Università degli Studi di Padova
Facoltà di Ingegneria
Tesi di Laurea Magistrale

MULTILEVEL SIGNAL PROCESSING USING PHASE SENSITIVE AMPLIFICATION

RELATORE: Ch.mo Prof. Marco Santagiustina

CORRELATORE: Prof. Christophe Peucheret

LAUREANDO: *Francesco Da Ros*

Padova, 10^{th} July 2011

Abstract

In this thesis we present a study on optical signal regeneration techniques, in particular for quadrature phase shift keying (QPSK) modulated signals. After an overview of the available strategies, we focus on phase sensitive (PS) parametric amplification in order to provide all-optical regeneration using fiber optical parametric amplifiers (FOPAs). Two regeneration schemes, one presented in literature and one developed here, are theoretically and numerically investigated. MATLAB® models have been implemented in order to benchmark the performances of the two methods both in terms of phase noise reduction, analyzing the phase standard deviation (std), and of bit error ratio (BER) improvement. At last an investigation on stimulated Brillouin scattering (SBS), one of the main limitations to parametric amplification, is reported. A dynamic model of SBS is employed to examine two promising techniques proposed to reduce the impairments caused by Brillouin effects: Aluminum-doped fibers and multi-segment links. Length optimization of a dual-fiber optical link combining these methods is finally discussed.

Ai miei genitori,
a Elisa

Contents

List of Figures

List of Tables

Acronyms

ASE amplified spontaneous emission

AWG array waveguide grating

AWGN additive white Gaussian noise

BER bit error ratio

BPF bandpass filter

BPSK binary phase shift keying

BtB back-to-back

CSRZ carrier-suppressed return to zero

CW continuous wave

DI delay interferometer

DP dual pump

DPSK differential phase shift keying

EDFA Er-doped fiber amplifier

FEC forward error correction

FOPA fiber optical parametric amplifier

FWHM full width half maximum

FWM four wave mixing

GVD group velocity dispersion

HNLF highly nonlinear fiber

LD laser diode

LPF low-pass filter

MF modulation format

MZ Mach-Zehnder

MZDI Mach-Zehnder delay interferometer

MZI Mach-Zehnder interferometer

MZM Mach-Zehnder modulator

NALM nonlinear amplifying loop mirror

NF noise figure

NLSE nonlinear Schrödinger equation

NOLM nonlinear optical loop mirror

NRZ non return to zero

OEO optic-electric-optic

OOK On-Off keying

OSNR optical signal-to-noise ratio

PD photo diode

PI phase insensitive

PIA phase insensitive amplification

PM phase modulator

PMD polarization mode dispersion

PP power penalty

PRBS binary pseudo random sequence

PRQS quaternary pseudo random sequence

PS phase sensitive

PSA phase sensitive amplification

PSK phase shift keying

QPSK quadrature phase shift keying

R-OSNR required OSNR

RPP relative power penalty

RZ return to zero

SA saturable absorber

SBS stimulated Brillouin scattering

SBST SBS threshold power

SI Sagnac interferometer

SOA semiconductor optical amplifier

SOP state of polarization

SP single pump

SPM self phase modulation

SPR signal-to-pump ratio

SSMF standard single mode fiber

std standard deviation

WDM wavelength division multiplexing

XPM cross phase modulation

ZDW zero-dispersion wavelength

Chapter 1

Introduction

The demand for capacity in communication systems is constantly increasing driven by a yearly internet growth of more than 50%. Microwave communication cannot withstand the massive speed requirement of the aggregated internet traffic, the task to provide such high bitrate then falls upon the optical communication systems building the core network.

Two are the main directions towards increasing both system reach and bitrate, which we look into in this study.
From one hand the use of high order modulation formats (MFs) like quadrature phase shift keying (QPSK) enables to extend the reach and achieve a higher spectral efficiency [1]. Phase modulations in conjunction with interferometric detection are indeed more tolerant to fiber impairments such as group velocity dispersion (GVD) and polarization mode dispersion (PMD) than On-Off keying (OOK) signals [2]. Multilevel MFs then are characterized by a higher spectral efficiency carrying more than one bit per symbol. A higher spectral efficiency allows to transmit a larger amount of information within the same bandwidth and thus increases the link capacity [3].

On the other hand signal processing features such as signal regeneration or switching, now mostly implemented through optic-electric-optic (OEO) conversion, show the potential to be provided all-optically [4, 5], thus removing the electrical domain bottlenecks. Moreover, avoiding electrical signal processing would also lower the power consumption in systems where the power budget is critical [6, 7].

Several schemes have been proposed for phase and amplitude regeneration of differential phase shift keying (DPSK) signals [4, 8–10]. The decreased distance of the constellation states for QPSK signals, however, increases the challenges in designing regeneration schemes. These challenges are the main focus of our thesis. Our goal is to study all-optical signal regeneration for QPSK signals using fiber optical parametric amplifiers (FOPAs).

First of all in Chapter 2 an overview on FOPAs, both in phase sensitive (PS) and phase insensitive (PI) configuration, is presented. Then Chapter 3 provides a summary of the state of the art in signal regeneration and in particular on the proposed solutions exploiting FOPAs. Chapters 4 and 5 discuss two approaches for QPSK phase regeneration. The first has been successfully demonstrated in [11] while the second scheme is here proposed as a method developed elaborating the gain saturation analysis reported in [12]. Next, Chapter 6 shows the performances of the two systems discussing the phase noise standard deviation (std) reduction and the bit error ratio (BER) improvement for 28 and 40 Gbaud QPSK signals with different pulse shaping. Finally in Chapter 7 the main impairment to parametric amplification, stimulated Brillouin scattering (SBS), is investigated and two promising trends towards mitigating its effects are presented. Numerical comparisons of parametric gain with and without SBS are also reported.

Chapter 2

Theoretical Background

Parametric amplification has been widely investigated in the last years as a mean to provide very high gain, up to 70 dB, or a flat gain over a large bandwidth, 20 dB over 100 nm [9]. Furthermore, the possibility of using parametric amplification in a phase sensitive scheme shows a high potential to provide phase regeneration and sub-quantum noise amplification. Finally, FOPA are attractive because the main building blocks are essentially a highly nonlinear fiber (HNLF) with low dispersion and a high power laser diode (LD) with low intensity noise, i.e. equipment already common in optical communication systems.
In this chapter we begin providing a brief description of Kerr nonlinearities with a particular focus on four wave mixing (FWM), the phenomenon parametric amplification relies on in optical fibers. In Section 2.2 we present a theoretical analysis of parametric amplification through a four-wave model. In Section 2.3 phase insensitive amplification (PIA) and phase sensitive amplification (PSA) are discussed taking also a brief look at sub-quantum noise amplification. Finally, in Section 2.4, two classes of FOPAs are introduced and analyzed.

2.1 Kerr Nonlinearities

Dielectric materials are characterized by a nonlinear response when an electric field is applied. The polarization is related to the electric field through the susceptibility:

$$\mathbf{P} = \epsilon_0 \left(\chi^{(1)} \cdot \mathbf{E} + \chi^{(2)} : \mathbf{EE} + \chi^{(3)} \vdots \mathbf{EEE} + \dots \right), \tag{2.1}$$

where ϵ_0 is the vacuum permittivity and $\chi^{(j)}$ is the jth order susceptibility.

As optical fibers are mainly made of silica (SiO_2), a symmetric molecule, the second order susceptibility vanishes. The main nonlinear effects to be taken into account are thus the results of the third-order susceptibility and they are known as Kerr nonlinearities. Kerr nonlinearities can be described through the use of the nonlinear refractive index n_2 in order to describe the intensity dependence of the optical fiber refractive index $n = n_0 + n_2 I$, with n_0 weak-field refractive index and I field intensity.

Three are the main Kerr nonlinearities, all characterized by the interaction between three electrical fields: self phase modulation (SPM), cross phase modulation (XPM) and four wave mixing (FWM).

When a single wave ω_1 propagates through the fiber, the field intensity modulates the refractive index of the silica and thus the phase of the wave itself. From this characteristic the effect is known as self phase modulation.

A second wave ω_2 injected into the fiber, other than undergoing phase modulation due to its own intensity, is also affected by the refractive index variations generated by the first field. This phenomenon is thus called cross phase modulation.

Finally a third co-propagating wave ω_3 experiences SPM and XPM effects due to the other waves, but it is also affected by the modulation caused by the beating component at $\omega_2 - \omega_1$. This effect results in the creation of sidebands at $\omega_3 \pm (\omega_2 - \omega_1)$. Due to the involvement of three waves in generating a forth one, this process is called four wave mixing.

The same effects experienced by ω_3 are also exerted on ω_2 by the beating between ω_1 and ω_3 and on ω_1 by $\omega_2 - \omega_3$.

An example of frequency spectrum at the output of a fiber when ω_1, ω_2, ω_3 are injected is shown in Figure 2.1. High order FWM products between waves not at the input are neglected and ω_{lmn} should be read as $\omega_l + \omega_m - \omega_n$.

The quantum mechanical picture corresponding to FWM consists in the annihilation of photons from one or more waves and the creation of new photons at frequencies such that energy and momentum conservation are fulfilled. The conservation laws can be rewritten in terms of frequency and propagation constant $\beta^{(i)} = \omega_i n(\omega_i)/c$ giving rise to (2.2a) and (2.2b).

$$\omega_{lmn} = \omega_l + \omega_m - \omega_n \,, \tag{2.2a}$$

$$\Delta\beta_{lmn} = \beta^{(lmn)} - \beta^{(l)} - \beta^{(m)} + \beta^{(n)} = 0 \,. \tag{2.2b}$$

The energy conservation law defines the grid where the new frequency components are

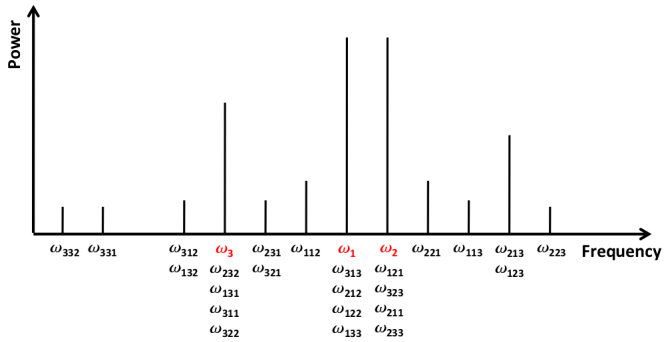

Figure 2.1: Frequency comb generated through FWM for two strong waves at ω_1 and ω_2 and a weak one at ω_3 in input to the fiber [13].

generated while the linear phase matching condition determines the efficiency of the FWM process.

Considering a particular case where we suppress the wave ω_3 and thus only the waves ω_1 and ω_2 are co-propagating, an expression for the FWM efficiency η can be easily derived. According to (2.2a), two waves are generated at $\omega_3 = 2\omega_1 - \omega 2$ and $\omega_4 = 2\omega_2 - \omega_1$. Assuming all the waves with the same state of polarization (SOP), Maxwell's equations in scalar form can be used to derive the power of these new frequency components. Furthermore, to simplify the derivation the pumps are assumed undepleted and the effects of SPM and XPM are neglected.
Defining the nonlinear coefficient γ, the losses α and the effective length L_{eff} as in Appendix A and calling $P_i(0)$ the power at the fiber input for the wave ω_i, it can be derived [14]:

$$P_3 = \eta_3 \gamma^2 L_{eff}^2 P_1^2(0) P_2(0) e^{-\alpha L}\,, \tag{2.3a}$$

$$P_4 = \eta_4 \gamma^2 L_{eff}^2 P_2^2(0) P_1(0) e^{-\alpha L}\,, \tag{2.3b}$$

where the FWM efficiency η_i for the ith wave is expressed by:

$$\eta_i = \frac{\alpha^2}{\alpha^2 + \Delta\beta_i^2} \left(1 + \frac{4 e^{-\alpha L} \sin^2\left(\frac{\Delta\beta_i}{2}\right)}{\left(1 - e^{-\alpha L}\right)^2} \right). \tag{2.4}$$

From (2.4) we can see that the efficiency is maximized only when $\Delta\beta_i = 0$. The phase matching is however highly dependent on the dispersion characteristic of the fiber. As discussed in Appendix A, since waves at different frequencies propagate with different

speeds, their interaction is strongly affected. Introducing this phenomenon we can rewrite $\Delta\beta$ as [14]:

$$\Delta\beta_{lmn} = \frac{\lambda^2\Delta\omega^2}{2\pi c}\left[D(\lambda_{lmn}) - \frac{\lambda^2}{2\pi c}\Delta\omega S(\lambda_{lmn})\right], \tag{2.5}$$

where $\Delta\omega$, D and S are respectively frequency spacing $|\omega_1 - \omega_2|$, dispersion (A.5a) and dispersion slope (A.5b).

This derivation is strongly limited by the amount of assumption made. Parametric processes are not fully described since SPM and XPM are neglected. Nevertheless it provides a meaningful insight into the relation between initial and newly generated waves and underlines the importance of dispersion.

2.2 Theory on Parametric Amplification

For our theoretical analysis of parametric amplification we use a four-wave model of [15]: two pumps at ω_1 and ω_2, a signal at ω_3 and an idler at ω_4. The other FWM products can be neglected either due to phase mismatch or low power.
From Maxwell's equations, assuming the same SOP for all waves, the following set of equations can be derived to describe the propagation of the four waves through the optical fiber [15].

$$\frac{dA_1}{dz} = i\gamma\left[|A_1|^2A_1 + 2\sum_{l=2}^{4}|A_l|^2A_l + 2A_3A_4A_2^*e^{i\Delta\beta z}\right], \tag{2.6a}$$

$$\frac{dA_2}{dz} = i\gamma\left[|A_2|^2A_2 + 2\sum_{l=2}^{4}|A_l|^2A_2 + 2A_3A_4A_1^*e^{i\Delta\beta z}\right], \tag{2.6b}$$

$$\frac{dA_3}{dz} = i\gamma\left[|A_3|^2A_3 + 2\sum_{l=2}^{4}|A_l|^2A_3 + 2A_1A_2A_4^*e^{-i\Delta\beta z}\right], \tag{2.6c}$$

$$\frac{dA_4}{dz} = i\gamma\left[\underbrace{|A_4|^2A_4}_{SPM} + \underbrace{2\sum_{l=2}^{4}|A_l|^2A_4}_{XPM} + \underbrace{2A_1A_2A_3^*e^{-i\Delta\beta z}}_{FWM}\right], \tag{2.6d}$$

where $\Delta\beta = \beta^{(3)} + \beta^{(4)} - \beta^{(1)} - \beta^{(2)}$. Since our focus is on parametric processes, losses are neglected throughout this Section. If required, an extra term $-\alpha/2A_i$ can be added to the right hand side of each equation.

Writing $A_i = \sqrt{P_i}e^{i\Phi_i}$ we can split (2.6) into a set of equations for the phases an one for the powers. Defining $\theta = \Delta\beta z + \Phi_4 + \Phi_3 - \Phi_2 - \Phi_1$, we derive [15]:

$$\frac{\partial}{\partial z}\theta = \Delta\beta + \gamma(P_1 + P_2 - P_3 - P_4) + 2\gamma\sqrt{P_1P_2P_3P_4}\left(\frac{1}{P_1} + \frac{1}{P_2} - \frac{1}{P_3} - \frac{1}{P_4}\right)\cos(\theta)$$

$$= \Delta\beta + \Delta\beta_{NL} = \kappa\,. \tag{2.7}$$

The total phase mismatch κ is thus defined by two components: the linear part defined in above and a nonlinear term due to contributions of XPM and SPM.

Furthermore from (2.6) we can derive also a relation between the powers of the four waves:

$$\frac{dP_3}{dz} = \frac{dP_4}{dz} = -\frac{dP_1}{dz} = -\frac{dP_2}{dz} = 4\gamma\sqrt{P_1P_2P_3P_4}\sin\theta\,. \tag{2.8}$$

The relation of equation (2.8) can be expressed in terms of the power evolution of each wave, resulting in:

$$P_1(z) = P_1(0) - x(z)\,, \qquad P_3(z) = P_3(0) + x(z)\,, \tag{2.9}$$

$$P_2(z) = P_2(0) - x(z)\,, \qquad P_4(z) = P_4(0) + x(z)\,.$$

It is worth remarking that this result is in line with the quantum mechanical description of the process. All the waves undergo an increase or decrease in power of the same amount.

The quantity of most interest is then the power transferred x. If positive it represents the power transferred from the pumps to signal and idler. Negative values instead indicate flow of power in the opposite direction. x is a function of the length of the fiber and it is strongly dependent on input power and phase of the four waves.

A solution in x can be analytically derived in terms of Jacobian elliptic functions. The solution however is quite complex and does not give a clear picture, so in this study we present instead some considerations on the power trends of the four waves through the simulation of a degenerate signal-idler case $\omega_3 = \omega_4 = (\omega_1 + \omega_2)/2$. The parameters used are $\gamma = 10\ \mathrm{W^{-1}{\cdot}km^{-1}}$, the GVD $\beta_2 = 16.8\ \mathrm{ps^2/km}$ and the fourth order dispersion $\beta_4 = 2.48 \cdot 10^{-4}\ \mathrm{ps^4/km}$ (Appendix A).

The signal initial power is 30 dB below the pump power. In Figure 2.2 both the total pump power and the signal power are plotted as they evolve throughout the fiber. The

curve shows clearly the periodic exchange of power between pumps and signal, in line with the trends reported in [16] for the non-degenerate case[1].

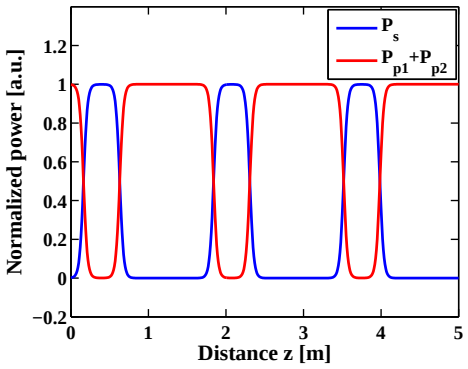

Figure 2.2: Normalized pumps and signal power for a DP-FOPA with degenerate signal-idler. The pump power is set to 1 W and the signal power 30 dB below.

As a final remark note that the equations in (2.6) neglect the influence of Raman and SBS. While the former effect is usually negligible in optical fiber, the latter represent a serious impairment for parametric amplification. For a more detailed discussion on Brillouin effects refer to Chapter 7.

2.3 Phase Sensitive and Phase Insensitive Parametric Amplification

The complex theory presented in the previous Section can be greatly simplified introducing the assumption of undepleted pumps. If the power of the pumps is orders of magnitude above the power of signal and idler, then it is reasonable to approximate the output pump power with the value at the input.
Furthermore, we have already underlined the importance of phase matching in determining the FWM performance. In this Section we set ourselves in the special scenario of perfect linear phase matching, i.e. $\Delta\beta = 0$, i.e. taking into account only $\Delta\beta_{NL}$.
Under these assumptions, (2.6) can be simplified into (2.10):

$$\begin{pmatrix} A_3 \\ A_4^* \end{pmatrix} = \begin{pmatrix} \cosh(\gamma L_{eff} P_T) & i\sinh(\gamma L_{eff} P_T) \\ -i\sinh(\gamma L_{eff} P_T) & \cosh(\gamma L_{eff} P_T) \end{pmatrix} \begin{pmatrix} A_3(0) \\ A_4^*(0) \end{pmatrix}, \tag{2.10}$$

[1] As in [16], losses are neglected.

where P_T represent the total pump power.

We now consider two different situations:

1. all the four waves are injected into the HNLF so both signal and idler are present,
2. the idler is suppressed, only two pumps and the signal are injected into the HNLF.

Note that the degenerate signal-idler scenario is part of the first case.

We can now derive the signal gain in these two cases.

When four waves are injected into the fiber, assuming for simplicity $P_3 = P_4$, then the gain results [9]:

$$G_3 = 1 + 2\sinh^2(\gamma L_{eff} P_T) - 2\sinh(\gamma L_{eff} P_T)\cosh(\gamma L_{eff} P_T)\sin(\theta)\,. \tag{2.11}$$

Due to the gain dependence on θ, the signal gain given by (2.11) is clearly phase sensitive.
This could have already been noticed in (2.8), where the sign of $\sin(\theta)$ determines the direction of the power flow. When $\sin(\theta)$ is positive the pumps photons are annihilated and signal and idler photons are created. When $\sin(\theta)$ is negative it is the signal that is attenuated.

Analyzing the second case, the idler is generated inside the HNLF according to $\Phi_4 = \Phi_2 + \Phi_1 - \Phi_3$. Using this expression we have $\theta = 0$ and thus the signal gain with no input idler results:

$$G_3 = 1 + 2\sinh^2(\gamma L_{eff} P_T)\,. \tag{2.12}$$

The phase dependence of (2.11) is lost in (2.12).
Furthermore, for values of γ, L_{eff} and P allowing high gain, the PI gain is 6 dB smaller than the PS. Figure 2.3 shows the comparison between the PI gain and both maximum and minimum PS gains through experimental results
PSA allows to achieve a higher gain, but with the drawback of requiring to inject also an idler phase-locked with the signal. Nevertheless PS-FOPAs are attracting quite some interest due to their potential in the fields of both phase regeneration and sub-quantum noise amplification.

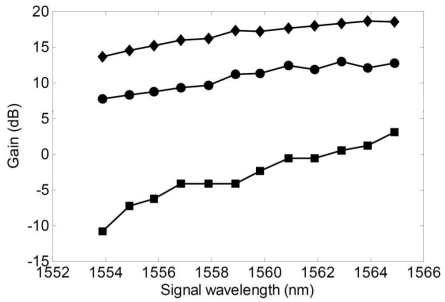

Figure 2.3: Comparison from PSA and PIA gain: PIA (•), maximum (⧫) and minimum PSA (■) gain [17].

Figure 2.3 shows an almost 15 dB difference between maximum and minimum PS gain. This feature has been employed in many proposed schemes for phase modulated signal regeneration as we discuss in the following Chapters.
Furthermore, if we consider the noise figure (NF) of the amplifier for both signal and idler, the noise fluctuation of the two waves are amplified of the same amount as the waves themselves. The complete correlation between signal and idler thus allows ideally to achieve a NF of 0 dB. The usual NF of 3 dB is in fact the result of noise generated both from the signal noise amplification and the wavelength conversion of the idler fluctuations [15, 18].
A dual pump (DP) degenerate configuration is therefore of particular interest. When signal and idler are at the same frequency the two waves are indistinguishable so only the noise in the input signal can give rise to noise in the output signal. The same gain is experienced by both the signal and the noise, the amplifier is characterized by NF=0 dB.

The ideal NF of 0 dB can however only be approached in practice. Other noise sources need to be taken into account: pump transfer noise, Raman noise and residual pump amplified spontaneous emission (ASE) noise [9]. To our best knowledge the lowest NF experimentally demonstrated is reported in [9] to be around 1 dB.

2.4 FOPA Schemes

In this Section we particularize the analysis for the two FOPA configurations: single pump (SP) and DP. The frequency assignments for the two configurations are shown in Figure 2.4.

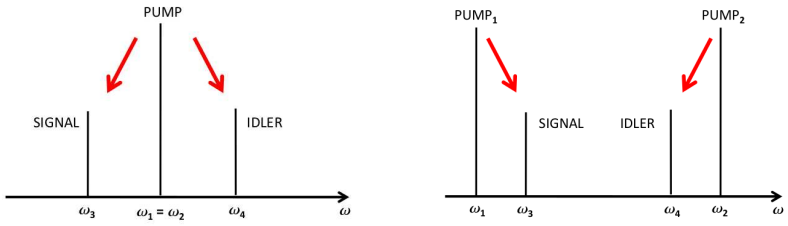

(a) (b)

Figure 2.4: Frequency assignment for single (a) and dual (b) pump FOPA.

2.4.1 Single Pump Scheme

This scenario (Figure 2.4(a)) is a special case of the four-wave model with $\omega_1 = \omega_2$ and (2.9) thus becomes:

$$P_1(z) = P_1(0) - 2x(z) \quad P_3(z) = P_3(0) + x(z) \quad P_4(z) = P_4(0) + x(z)\,. \tag{2.13}$$

Furthermore, assuming no losses and undepleted pump, an analytical expression for the signal gain can be derived solving (2.8) as in [13].

$$G_s = 1 + \left[\frac{\gamma P_p}{g}\sinh(gL)\right]^2\,, \tag{2.14}$$

where the parametric gain coefficient g is given by

$$g^2 = -\Delta\beta\left[\frac{\Delta\beta}{4} + \gamma P_p\right]\,. \tag{2.15}$$

First of all we can notice that in the limit $\Delta\beta \to 0$ we can obtain (2.12).

Then, to briefly investigate PIA for this waves configuration, a numerical model of the SP-FOPA structure of [13] has been implemented. A pump at $\lambda_p = 1560.7$ nm has been amplified to $P_p = 1.4$ W and injected together with a 10 nW signal inside a 500 m fiber with the signal wavelength λ_s swept from 1515.7 nm to 1605.7 nm. Zero-dispersion wavelength, dispersion slope and γ of the fiber, are respectively 1559 nm, 0.03 ps/nm$^2\cdot$ km and 11 W$^{-1}\cdot$ km^{-1}. Losses are neglected to allow comparison with (2.14).

The propagation in the optical fiber is calculated solving the nonlinear Schrödinger equation (NLSE) with the Split-step Fourier Method of Appendix B.

Figure 2.5 shows an excellent agreement between the numerical results obtained and the theoretical curve obtained from (2.14). Agreement which provides a first validation of our numerical model.

Furthermore, Figure 2.5 gives an example of the bandwidth range achievable with parametric amplification. As already mentioned one of the most interesting features of

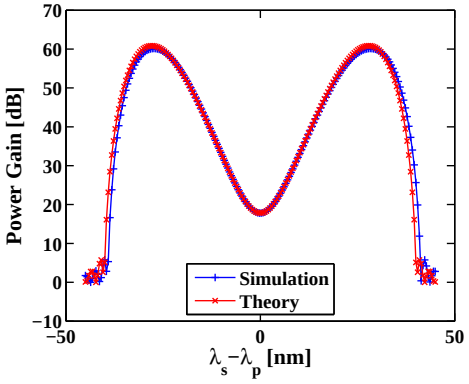

Figure 2.5: Parametric gain in SP-FOPA - comparison between our simulation and (2.14).

FOPAs is providing a flat gain over a wavelength range wider than Raman and Er-doped fiber amplifier (EDFA) [13].
Assessing the benefits of this configuration we have both the possibility to obtain PSA coupling the idler inside the HNLF and the potential to provide amplification for wavelength division multiplexing (WDM) systems due to its wide gain bandwidth.

2.4.2 Dual Pump Scheme

The frequency assignment for the DP-FOPA scheme is shown in Figure 2.4(b). Two pumps (ω_1) and (ω_2) are co-propagating together with a signal (ω_3) and idler (ω_4). In this thesis all DP configurations assume equal power for the two pumps ($P_1 = P_2$), asymmetry effects are therefore neglected.

Compared to a SP FOPA this scheme requires a lower single pump power. One photon per pump is transferred to signal and idler compared to the two in the SP configuration. Furthermore, in a signal-idler degenerate scheme, PSA can be achieved injecting only one wave carrying the data, saving the complexity of the idler generation block.

A degenerate configuration is, however, inherently single channel. Only one channel can be amplified since it requires $\omega_3 = (\omega_1 + \omega_2)/2$.

DP FOPAs in a non-degenerate and degenerate configuration are analyzed in Chapter 4 and 5 respectively.

Chapter 3

Signal Regeneration in FOPA: State of the Art

In this chapter we provide an overview of the state-of-the-art in signal regeneration with particular focus on FOPAs. We begin with an introduction to amplitude and phase regeneration, underlining limits and possibilities for each of the three main approaches proposed. Then we proceed into analyzing amplitude regeneration through an interesting feature offered by FOPAs: gain saturation. Finally we report various results on phase regeneration describing different proposed schemes for both DPSK and QPSK modulated signals.

3.1 Introduction to Amplitude and Phase Regeneration

In an optical communication system several noise sources give rise to impairments for the transmission. Other than at the transmitter and receivers the noise sources in the link itself grow more and more detrimental when increasing the bitrate and transmitting with multilevel MFs.

An optical signal is impaired by two types of noise: amplitude and phase noise. These noise components are shown in the phasors diagrams of Figure 3.1.

The main source of amplitude noise in an optical link is represented by the amplified spontaneous emission (ASE) introduced by optical amplifiers. As we have already mentioned in Chapter 2, the NF of the amplifiers currently (Raman and EDFAs) in use is above 3 dB. Amplitude noise thus accumulates throughout the link providing a serious impairment especially for amplitude modulated signals.

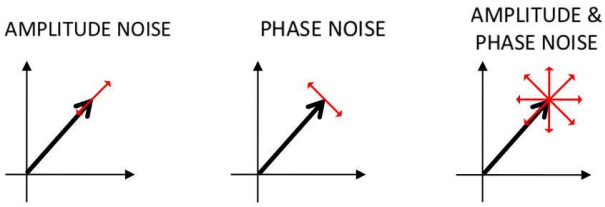

Figure 3.1: Phasors diagrams showing amplitude and phase noise.

Considering phase modulations instead, amplitude noise could be expected to cause a less severe degradation. Phase modulated signals, however, are strongly affected by phase noise, both in its linear and nonlinear component. Linear phase noise is mainly due to the optical fiber dispersion (Appendix A), and thus its variance is linearly proportional to the total length of the fiber span [19]. Nonlinear phase noise instead is caused by the conversion of the ASE noise into phase noise through Kerr nonlinearities. The variance of this component has been estimated in [1, Formula (6.29)] to be inversely proportional to the optical signal-to-noise ratio (OSNR) other than growing quadratically with the fiber length. Amplitude noise cannot therefore be neglected for phase modulated signals. In fact it represents a serious impairment to the transmission and as such needs to be limited to avoid its conversion into nonlinear phase noise.
To decrease the accumulated noise, the use of regenerators is being investigated. Concerning systems relying on phase modulated signals, three are the main areas where the research has been focused:

- Modulation format conversion
- Phase preserving amplitude regeneration
- Phase sensitive amplifiers.

3.1.1 Modulation Format Conversion

In general the amplitude is easier to control compared to the phase of a signal. Various methods for intensity modulated signal regeneration have been proposed in the past years [20–22]. Until very recently intensity modulations were indeed the preferred choice for optical communications due to their easy implementation.
Intensity regeneration methods can thus be employed using MF conversion. All-optical

signal regeneration is performed in three steps: phase-to-amplitude conversion, amplitude regeneration, amplitude-to-phase conversion.
Various schemes have been proposed, mainly for DPSK modulated signal.
Phase-to-amplitude conversion is realized either with the use of a delay interferometer (DI) or with a more complex coherent demodulation.
Then, amplitude regeneration can be performed through:

- SPM or XPM in optical fibers [23, 24],
- semiconductor optical amplifier (SOA)-based Mach-Zehnder interferometer (MZI) [6, 25, 26] ,
- phase modulator (PM)-based MZI [27].

Finally the information is converted back into the phase domain through the use of all-optical phase modulators.
To better show the concept, Figure 3.2 shows the constellation diagrams at the key points of the scheme proposed in [24].

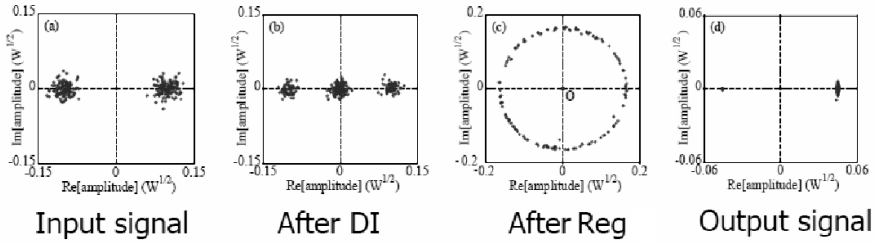

Figure 3.2: Constellation diagrams at the key points of the regeneration scheme [7].

The output signal constellation diagrams indeed shows the suppression of both phase and amplitude noise compared to the regenerator input.
The main drawback of this strategy is the inherently single channel operation. Furthermore pre-coding is required and the amplitude-to-phase conversion may propagate errors to subsequent bits.

3.1.2 Phase Preserving Amplitude Regeneration

The approach presented in the previous section has the strong limitation of not being MF transparent, and it is characterized by an increasing complexity when adapted to high order MFs (multilevel).

As an alternative approach, phase preserving amplitude regeneration has been strongly investigated. This strategy allows to perform amplitude regeneration reducing the intensity noise and thus lowering the generation of nonlinear phase noise. Furthermore no MF conversion is required.
On the other hand, no phase regeneration can be obtained so this method does not treat any existing phase noise and no WDM capabilities have been demonstrated.
The principle of phase preserving amplitude regeneration is shown in Figure 3.3. Ideally the constellation is squeezed in amplitude without increasing the phase noise.

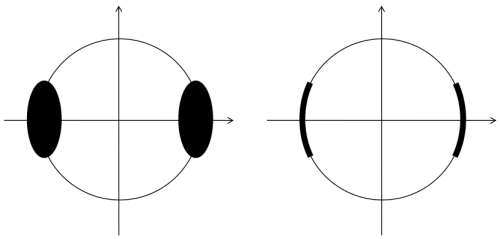

Figure 3.3: Operating principle of phase preserving amplitude regeneration: input (left) and output (right) of the regenerator.

Several systems have been suggested in literature implementing this method:

- Saturated FOPA [28–30],
- XPM in optical fibers [31],
- nonlinear optical loop mirror (NOLM) [32],
- nonlinear amplifying loop mirror (NALM) [33],
- saturable absorber (SA) [34].

Phase preserving amplification through saturated FOPAs is further elaborated in Section 3.2.

3.1.3 Phase Sensitive Amplifiers

Both amplitude and phase regeneration, without the need to perform MF conversion, would be desirable for phase modulations.
Phase sensitive amplification can be used to regenerate the phase of a signal suppressing the phase noise. Some schemes have also shown WDM capabilities [35]. Furthermore

using saturated PS-FOPA the signal amplitude can also be partially cleaned. In general however a second stage of phase preserving amplitude regeneration may be required to remove the residual intensity noise.

Figure 3.4 shows the idea behind this latter strategy. This particular scheme is analyzed in details in Chapter 5

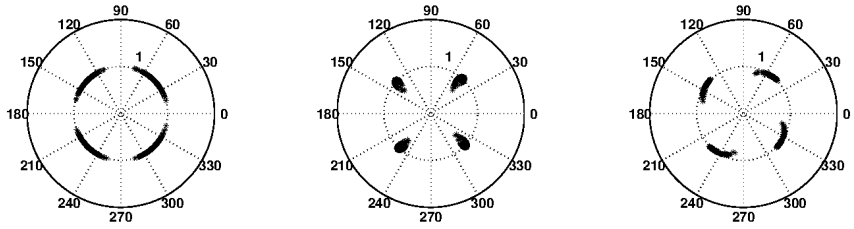

Figure 3.4: Simulated constellation diagrams at input (left), after the PS-FOPA (center) and after the amplitude regenerator (right).

As can be seen, the main drawback of this approach is the re-introduction of some phase noise in the second stage. Overall however, the amount of both phase and intensity noise is indeed decreased. Finally, a stringent phase and frequency locking between the waves involved is required. Some practical solutions to this issue are presented in Sections 3.3 and 3.4.

3.2 Amplitude Regeneration

In the previous Section we have given a general introduction to the concept of phase preserving amplitude regeneration. Here we provide a more detailed analysis on how FOPAs can be used to regenerate the amplitude of DPSK and QPSK modulated signals.

Figure 3.5 shows the signal power at the output of the FOPA proposed in [28] as a function of the input signal power. The FOPA consists in a HNLF characterized by zero-dispersion wavelength (ZDW), dispersion slope, nonlinearity, losses, and length of λ_0 = 1556 nm, S=0.026 ps/nm^2·km, γ=12 W^{-1}·km^{-1}, α=0.78 dB/km, and L=150 m, respectively. A single pump scheme is used with a 20 mW pump at λ_p =1561 nm. The signal-pump frequency separation is 600 GHz.
The numerical results of our simulations, in good agreement with the experiments of

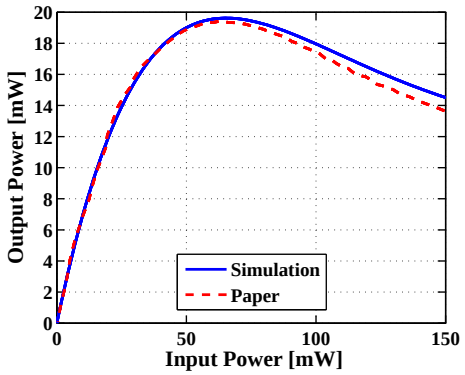

Figure 3.5: Output signal power as function of the input signal power: comparison between numerical simulations (continuous) and experimental results [28] (dashed).

[28] , illustrate the power saturation for a signal power of ~ 50 mW. The almost flat curve for higher signal power enables to reduce the intensity fluctuations and thus clean the signal amplitude.

Figure 3.6 shows the effects of saturation for DPSK modulated signals respectively through the eye [36] and constellation diagrams [30].

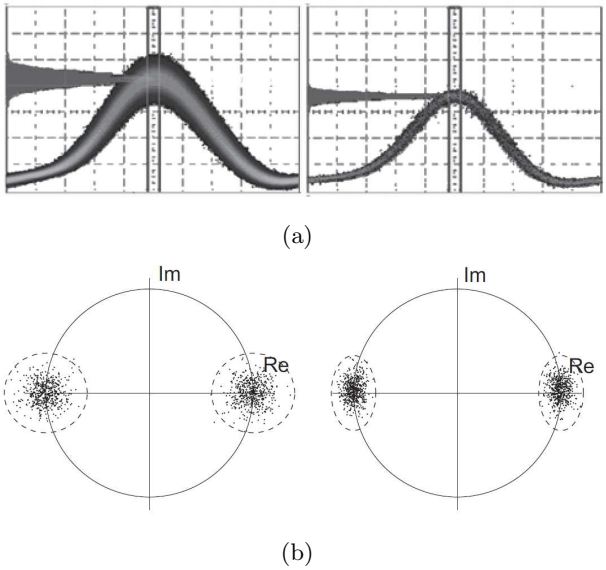

(a)

(b)

Figure 3.6: Eye (a) and constellation (b) diagrams at input (left) and output (right) of the regenerator of [36] and [30] respectively.

The constellation diagrams underline the challenge of designing the FOPA to be phase-transparent. An increase in the phase noise at the regenerator output can be noticed.

3.3 Phase Regeneration for DPSK signals

In this Section we focus on phase regeneration for DPSK signals through PS-FOPA. We report various schemes giving first a brief description focused on the most interesting aspects of each method and then showing some numerical or experimental results reported and in one case also reproduced.

3.3.1 Single Pump Degenerate FOPA

One of the first methods for DPSK regeneration has been proposed in [8]. The regenerator analyzed and simulated relies on a degenerate signal-pump configuration inside an interferometric structure as in Figure 3.7.

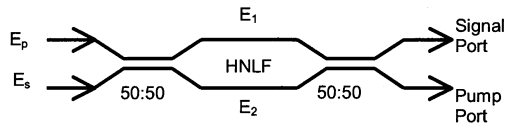

Figure 3.7: SP scheme for DPSK regeneration from [8].

A strong pump and a DPSK modulated signal are coupled together in a MZI with the same HNLF in both the arms. The total fields inside the two arms are different and so are the nonlinear phase shifts experienced by the waves.

$$E_1 = (E_{s0} + iE_{p0})/\sqrt{2} \qquad E_2 = (iE_{s0} + E_{p0})/\sqrt{2}\,,$$

where the subscripts $s0$, $p0$ refers to signal and pump at the MZI input.
The output power P_s at the upper (signal) port results [8]:

$$P_s = P_{s0}\cos^2(\Phi_{nl}) + P_{p0}\sin^2(\Phi_{nl}) - \sqrt{P_{s0}P_{p0}}\sin(2\Phi_{nl})sin(\Phi_{p0} - \Phi_{s0})\,, \tag{3.1}$$

where Φ_{s0} and Φ_{p0} are the two waves phases and $\Phi_{nl} = \gamma L|E_{s0}E_{p0}|\cos(\Phi_{p0} - \Phi_{s0})$ is the nonlinear phase shift.

The phase sensitivity of the scheme follows immediately from (3.1). The nonlinear phase shift is strongly dependent on the relative phase between pump and signal and

in turn it can vary the output power from P_{s0} ($\Phi_{nl} = 0, \pi$) to P_{p0} ($\Phi_{nl} = \pi/2, 3\pi/2$).

Figure 3.8 shows the gain and output signal phase as a function of $\Phi_{p0} - \Phi_{s0}$ for P_{p0} = 20 mW, $P_{s0} = 175$ mW $\gamma = 27$ W^{-1}·km^{-1}, $L = 6$ km.

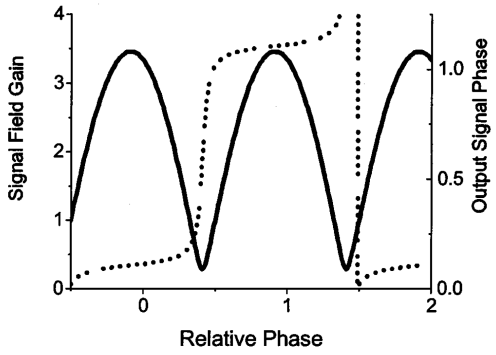

Figure 3.8: Gain and output signal phase as function of the input signal phase [8].

Analyzing the response of the FOPA, the output phase shows clearly π-spaced levels. These curve present indeed the trends required for DPSK signal regeneration. Furthermore the gain is characterized by π-spaced peaks aligned with the flat zones in the phase response.

3.3.2 Single Pump Non-Degenerate FOPA

In Chapter 2 we have mentioned that a SP FOPA can be used in a PS configuration if both signal and idler are coupled into the HNLF.

Phase regeneration for DPSK signals has been demonstrated through such a scheme in [9, 37]. In the setup proposed two stages of HNLF are employed. First in a PI-FOPA the four-wave mixing between two continuous waves (signal and pump) generates a third phase-locked wave (idler). Then, after modulating both signal and idler, the three waves are injected into the second stage acting as PS-FOPA and providing the phase regeneration.

Figure 3.9(a) shows the calculated static curves for different values of the maximum gain [9]. As the gain is increased, the phase approaches the target step-like profile.
Figure 3.9(b) illustrates the phase-squeezing effect obtained when the FOPA is operating in PS mode, i.e. with both signal and idler at the input, compared to the PI mode.

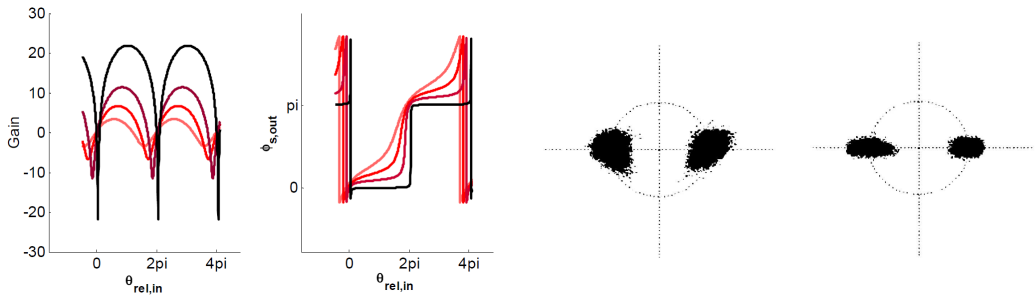

(a) (b)

Figure 3.9: Gain and output signal phase (a) as function of the input signal phase for different maximum gain values. Constellation diagrams (b) at the output of a PI-FOPA (left) and a PS-FOPA (right). Figures from [9].

3.3.3 Dual Pump Degenerate FOPA

A DP degenerate signal-idler scheme providing phase regeneration has been first analyzed numerically in [10] and then demonstrated experimentally in [4].
Assuming the pump undepleted, the interaction between the three waves can be studied theoretically. Following [38] it can be derived that the evolution of the signal inside the FOPA follows:

$$B_S(z) = \mu(z)B_S(0) + v(z)B_S^*(0)\,. \tag{3.2}$$

with $B_S(z) = A_S(z)e^{i\beta z/2}$, transformed signal amplitude.
Formula 3.2 can be related to the quantum mechanical concept of mode squeezing since the μ and v functions are expressed as:

$$\mu(z) = \cosh(gz) + i\frac{\kappa}{2g}\sinh(gz)\,, \tag{3.3a}$$

$$v(z) = \frac{2\gamma A_{P1}(0)A_{P2}(0)}{g}\sinh(gz)\,, \tag{3.3b}$$

where κ is the total phase matching coefficient of (2.7) and $g = \sqrt{4\gamma^2 P_{P1}P_{P2} - (\kappa/2)^2}$ the parametric gain. Such expressions indeed recall Baker-Hausdorff lemma [39].

To investigate the gain and phase response of the FOPA, a model of the system has been implemented solving the propagation through the fiber as in Appendix B.
The simulated FOPA consist of a HNLF characterized by length, nonlinear coefficient, ZDW, dispersion slope and β_4 respectively 200 m, 12 $W^{-1}{\cdot}km^{-1}$, 1560 nm,

0.03 ps/nm^2·km and -2.48·10^{-4} ps^4/km. The continuous wave (CW) pumps with 27 dBm of power are tuned at 1540 and 1580 nm and the signal at 1559.7 nm.
Figure 3.10 shows signal gain and output phase as function of the input signal phase. The results of our simulations have been superimposed to the data presented in [10] and good agreement is shown.

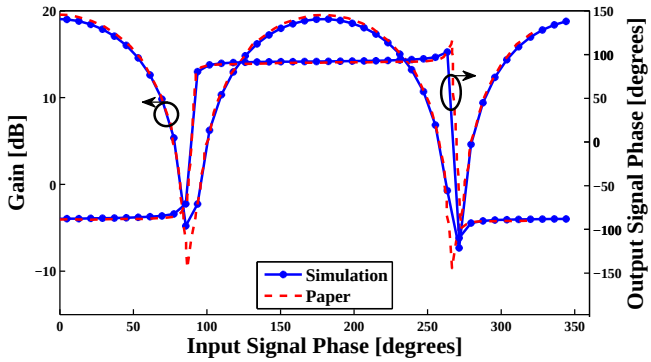

Figure 3.10: Gain and output signal phase as function of the input signal phase. Comparison between our own simulations (continuous) and the data in [10] (dashed).

As in Figure 3.8, the output phase shows a π-spaced step-like trend and the gain a π-spaced peaks profile and thus the characteristics required for DPSK signal regeneration. To further prove the effectiveness of this scheme, a noisy DPSK signal at 10 Gb/s has been injected into the regenerator. The phase noise has been simply modeled through a laser linewidth of 10 GHz. The phase of the signal at input and output of the regenerator is shown in Figure 3.11.

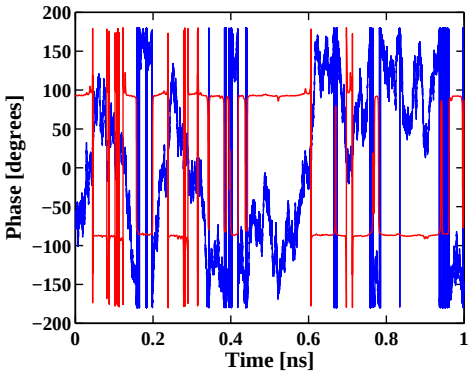

Figure 3.11: Simulated phase at the input (blue) and output (red) of the regenerator. Phase noise added through a 10 GHz laser linewidth.

The output phase is indeed characterized by a regenerated two-level trend.

The efficacy of this method has also been investigated experimentally in [4]. The main challenge of the practical implementation of this scheme is the need for two pumps phase-locked with the signal. In [4] this has been achieved with a strategy similar to [9]. In a first PI-FOPA stage the signal and a pump are four-wave mixed to generate a second phase-locked pump. Then the generated pump is cleaned from the noise using an injection-locked laser (see Chapter 4).
It is important to remark that only the phase noise needs to be removed, the modulation is not transferred to the second pump due to the squaring relation of the FWM process: $\Phi_i = 2\Phi_s - \Phi_p$.
Figure 3.12(a) shows constellation diagrams at input and output of the regenerator. The phase noise is indeed decreased

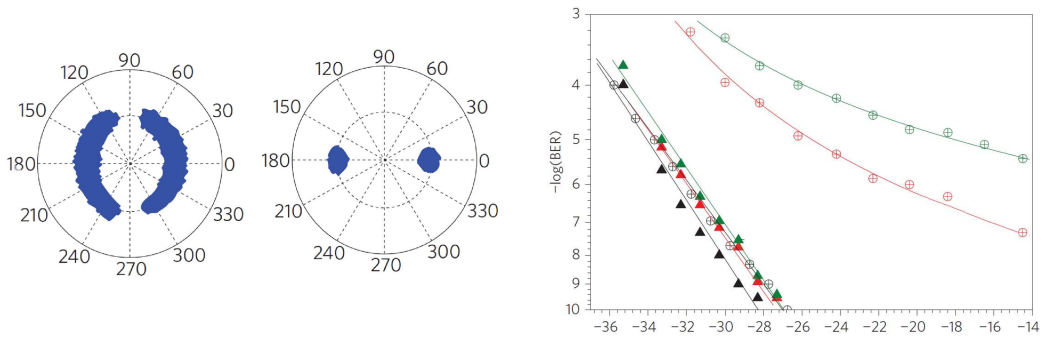

(a) (b)

Figure 3.12: Constellation diagram (a) at input (left) and output (right). BER (b) as a function of the received average power for no perturbation (black), ±30° (red) and ±50° (green) at input (⊕) and output (▲) [4].

Finally the BER as a function of the received average power is reported in [4] for three different levels of phase perturbations: no perturbation, ±30° and ±50°. The comparison between input (⊕) and output (▲) are shown in Figure 3.12(b).

3.3.4 Dual Pump Non-Degenerate FOPA

As previously mentioned the use of a DP non-degenerate scheme has the potential for WDM regeneration but requires three waves phase-locked with the signal. Not only the pumps but also the idler needs to be injected into the FOPA. In the scheme proposed in

[40], pumps and idler are generated through a Mach-Zehnder modulator (MZM)-based comb generator. Then the two pumps are amplified and cleaned from noise with the use of two injection-locked lasers as in the previously analyzed system [4].

Figure 3.13(a) shows the constellation diagrams at the input and output of the proposed regenerator for two different choices for the noise. In both cases the phase noise is introduced through a PM but while in the first case the electrical signal driving the modulator is a '1100' periodic sequence, in the second experiment a quasi-random sequence with a 2^{15}-periodicity is used.

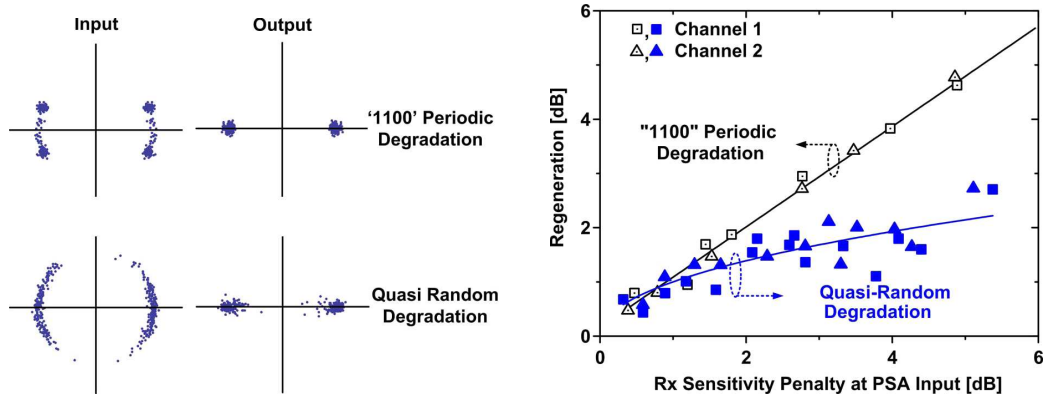

(a) (b)

Figure 3.13: Constellation diagrams (a) at input (left) and output (right) of the regenerator for periodic (up) and quasi random (down) degradation. Improvement (Regeneration) (b) between the receiver sensitivity at output and input of the regenerator as a function of the sensitivity at the input for the two different noise types [40].

The constellation diagrams indeed show a significant decrease in the phase noise. Furthermore they highlight a different response of the regenerator to the two noise types. This aspect is further investigated analyzing the improvement in receiver sensitivity before and after the regenerator. It can be seen in Figure 3.13(b) that the periodic degradation allows to improve the performances linearly (on a logarithmic scale) while for quasi random noise the improvement saturates.

The worsening of the performances when quasi-random degradation is added can be identified into the phase-to-amplitude noise conversion, as shown in Figure 3.13(a) [40].

3.4 Phase Regeneration for QPSK signals

The signal regeneration for QPSK modulated signal results more challenging than for DPSK since the constellation points are characterized by a smaller phase-separation.
Nevertheless three methods have been presented making use of either two SP degenerate FOPAs in an interferometer [41] or a DP FOPA in a degenerate [42] and non-degenerate [11, 43] configuration.
Only two of these methods are presented here. The last one is analyzed in more details in Chapter 4.

3.4.1 Single Pump Degenerate FOPA

In Section 6.1 a rigorous description of a Mach-Zehnder (MZ)-based QPSK modulator is provided. The main idea is to use a "super-MZI" with a DPSK modulator in each arm. The same idea has been applied in [41] to convert the DPSK regenerator of Subsection 3.3.1 into a QPSK regenerator.
The system is shown in Figure 3.14. In PSA1 the regeneration is carried on along the $\pi/2 \rightarrow 3\pi/2$ direction, while PSA2 squeezes the noise along the orthogonal $0 \rightarrow \pi$ direction. Both PSA1 and PSA2 are the Sagnac interferometer (SI) equivalents of Figure 3.7.

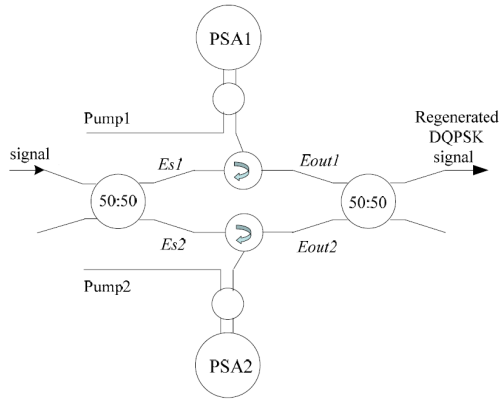

Figure 3.14: QPSK regeneration scheme from [41]. PSA1 and PSA2 are the SI equivalents of Figure 3.7.

This approach can be seen as demultiplexing the QPSK signal into two DPSK signals which are singularly regenerated and re-multiplexed back together. The occurred regeneration is shown in Figure 3.15

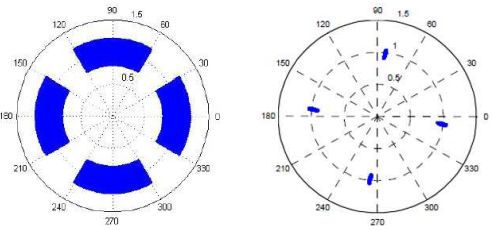

Figure 3.15: Constellation diagrams at input (left) and output (right) of the regenerator from [41].

A more detailed analysis of another interferometer-based scheme we propose is presented in Chapter 5.

3.4.2 Dual Pump Degenerate FOPA

The phase regeneration for DPSK signals is based on the fact that $\theta = \Phi_{P1} + \Phi_{P2} - 2\Phi_s - \beta(z)$ as in Section 2.2. The DP degenerate scheme of [42] relies on creating a phase relation as:

$$\theta = \Phi_{P1} + \Phi_{P2} - 4\Phi_s - \beta(z)\,. \tag{3.4}$$

The setup used to achieve this condition is shown in Figure 3.16.

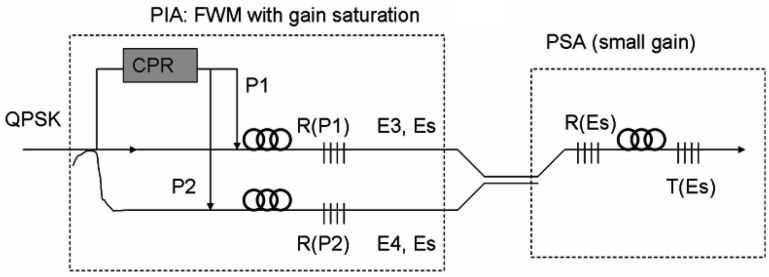

Figure 3.16: Two stages setup providing QPSK regeneration [42]: CPR carrier phase and polarization recovery, R reflected and T transmitted.

The system consists of two stages. First SP-FOPA-based MZI generates pumps 3 and 4 such that $\Phi_{3,4} = \pi/2 + 2\Phi_{1,2} - \Phi_s$, with $\Phi_{1,2}$ phases of pump 1 and 2 respectively. Then, injecting the newly generated pumps and the signal in a DP degenerate FOPA, (3.4) is obtained.

Static curves and constellation diagrams demonstrating the regeneration effect are shown in Figure 3.17.

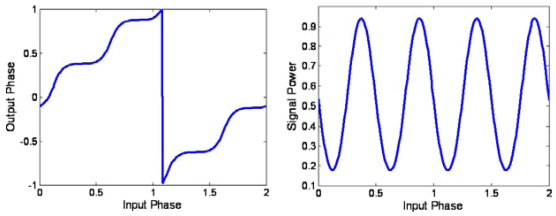

(a)

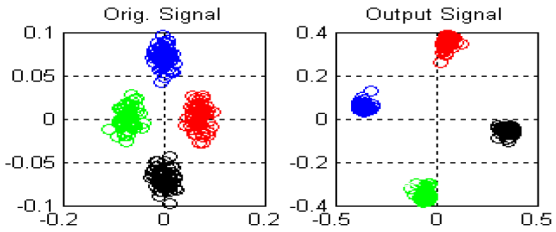

(b)

Figure 3.17: Static curves (a) and constellation diagrams (b) demonstrating the regeneration [42].

The regeneration is clearly visible from Figure 3.17(b). Note that the shape of the QPSK states is distorted by the different scale on x and y axis.

Chapter 4

Dual Pump Non-Degenerate FOPA for QPSK Regeneration

In this chapter we introduce and analyze the first of the two schemes for QPSK regeneration that are studied in this thesis. This method has been proven effective in achieving phase noise suppression in [11]. In Section 4.1 the regenerator is described underlining the main idea together with challenges and proposed solutions. Then Section 4.2 provides a theoretical analysis to show the principle providing phase regeneration. Section 4.3 reports the static gain and phase response calculated through numerical simulations. Finally Section 4.4 comments upon the potential application of the method and on a variant of the scheme proposed in [43].

Note that unlike in Chapters 2 and 3, here we denote the signal with $\omega_s = \omega_2$, the idler with $\omega_i = \omega_3$ and the pumps with $\omega_{p1} = \omega_1$ and $\omega_{p2} = \omega_4$. This choice is made to follow the order from lower to higher frequency.

4.1 Regenerator Setup

Figure 4.1 shows the setup proposed in [11].

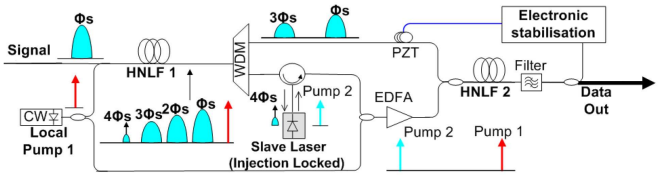

Figure 4.1: Setup for the QPSK regenerator of [11].

The regenerator is made of two stages: a PI-FOPA and a PS-FOPA and it is based on a DP non-degenerate scheme. As already described in the previous chapters the main challenge of this system is the need for three waves phase-locked with the signal in input to the PS-FOPA. The task of the first stage is thus to act as a frequency comb generator up to the fourth harmonic.

The input signal at 1555.7 nm is modulated in a QPSK format at 28 or 40 Gbaud, amplified to 22 dBm and injected into the first HNLF together with a 14 dBm CW pump at 1557.2 nm.

The parameters characterizing the first HNLF are shown in Table 4.1. In [11], no information about the fiber losses is given. The value used in our simulation has been chosen higher than the typical value for HNLFs assuming an Al-doped HNLF in order to neglect SBS effects (see Chapter 7). Al-doped HNLFs actually show losses up to 15 dB/km, losses are however not critical for our analysis. The regeneration would be provided also for 15 dB/km of losses, only the power levels may need to be adapted.

	HNLF 1	HNLF 2	Unit
Length	500	300	m
Losses	3.5	3.5	dB/km
Nonlinear coefficient	10.7	11.6	$W^{-1}{\cdot}km^{-1}$
Zero-dispersion Wavelength	1544	1553	nm
Dispersion slope (at ZDW)	0.029	0.018	$ps/nm^2{\cdot}km$

Table 4.1: Main parameters for the two HNLFs modeled as in [11].

The spectra at input and output of the first HNLF are shown in Figure 4.2.
The generation of a frequency comb is clearly visible. The frequency components needed as idler and second pump at the input of the PS-FOPA are the third and fourth harmonic, $\omega_i = \omega_s + 2(\omega_s - \omega_{p1})$ and $\omega_{p2} = \omega_s + 3(\omega_s - \omega_{p1})$ respectively (Figure 4.2(b)).

In the original setup of [11] a WDM de-multiplexer is used to separate the components. Then the wave at ω_{p2} is coupled into an injection-locked laser in order to remove the high frequency phase noise.

In our simulations, the WDM de-multiplexer is simulated through a set of third order

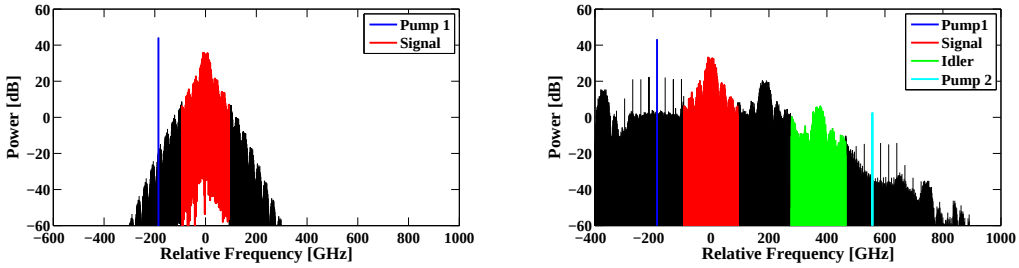

(a) Input (b) Output

Figure 4.2: Simulated spectra at the input (a) and output (b) of HNLF 1. The frequencies are relative to the signal frequency.

Gaussian bandpass filters (BPFs) with 0.75 nm full width half maximum (FWHM) bandwidth. Concerning the injection-locked laser then, due to the lack of a simple model, we simply generate a CW pump at ω_{p2} with a constant phase to simulate the phase locking.

Nevertheless the injection-locking solution is worth some remarks. First, as mentioned for the case of Section 3.3, also in this case the injection-locked laser (slave laser) does not need to remove the phase modulation. The phase of the fourth harmonic is given by $\Phi_{p2} = 4\Phi_s - 3\Phi_{p1}$ due to the relation $A_{p2} \propto A_s^4$. The signal phase modulation is then suppressed by the fourth power dependence. Furthermore, both frequency and phase of the wave at the output of the slave laser have a constant relation with frequency and phase of the injected wave. Assuming ω_{p2} in the injection-locking range of the slave laser, the emission frequency is shifted to ω_{p2} and the phase Φ_{out} is proportional to a time average of the injected wave phase Φ_{in} [44, 45]. As a rough approximation this process can be interpreted as:

$$\Phi_{out}(t) \propto \frac{1}{\tau} \int_{t-\tau/2}^{t+\tau/2} \Phi_{in}(t')dt' , \tag{4.1}$$

where τ is the characteristic response time of the laser which is longer than the fast time-variations of Φ_{in}.

After cleaning ω_{p2} the two pumps are combined together, amplified through an EDFA up to 24 dBm of total power and injected with signal and idler into HNLF 2 (Table 4.1). This second stage, with both signal and idler at the input performs then the PSA. Finally another Gaussian BPF is used to select the regenerated signal and remove the

other frequency components.

4.2 Theory

After describing the whole system, in this Section we focus into understanding the physical effects taking place in the PS-FOPAs and showing the principle behind the phase regeneration.

Let us review phases and frequencies of the waves at the input of HNLF 2.

Pump 1:	Φ_{p1}	ω_{p1}
Signal:	Φ_s	ω_s
Idler:	$\Phi_i = 3\Phi_s - 2\Phi_{p1}$	$\omega_i = \omega_s + 2(\omega_s - \omega_{p1})$
Pump 2:	$\Phi_{p2} = 4\overline{\Phi}_s - 3\Phi_{p1}$	$\omega_{p2} = \omega_s + 3(\omega_s - \omega_{p1})$

Table 4.2: Review of frequency and phase of the waves in input to HNLF 2.

where $\overline{\Phi}_s$ represents the phase of the noise-free signal.

Following the same approach of Figure 2.1 we can analyze the frequency comb at the output neglecting the higher-order FWM processes between the waves not present at the input.

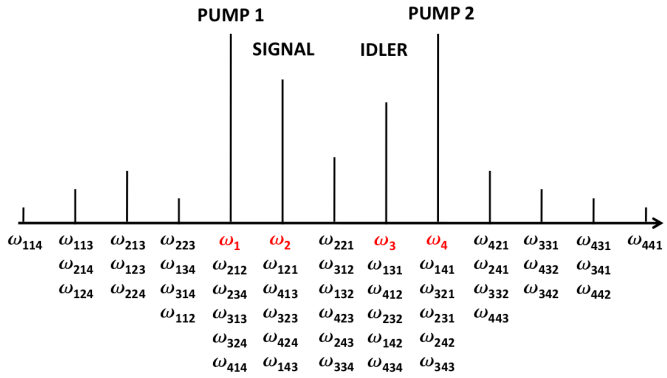

Figure 4.3: Frequency components at the output of HNLF 2.

A depiction of the frequency components distribution is shown in Figure 4.3. For clarity the products ω_{ijj} are not shown as they do not cause interesting changes in the waves phase.

We can thus see that five FWM products are frequency matched with the signal, respectively ω_{121}, ω_{413}, ω_{323}, ω_{424} and ω_{143}. Limiting our analysis to the phase of such

waves we can write:

$$\begin{aligned}
\omega_{121} &\rightarrow e^{-i(\Phi_{p1}+\Phi_s-\Phi_{p1})} = e^{-i(\Phi_s)}, \\
\omega_{413} &\rightarrow e^{-i(\Phi_{p2}+\Phi_{p1}-\Phi_i)} = e^{-i(\Phi_0-\Phi_i)}, \\
\omega_{323} &\rightarrow e^{-i(\Phi_{p1}+\Phi_s-\Phi_{p1})} = e^{-i(\Phi_s)}, \\
\omega_{424} &\rightarrow e^{-i(\Phi_{p2}+\Phi_s-\Phi_{p2})} = e^{-i(\Phi_s)}, \\
\omega_{143} &\rightarrow e^{-i(\Phi_{p1}+\Phi_{p2}-\Phi_i)} = e^{-i(\Phi_0-\Phi_i)},
\end{aligned}$$

where Φ_0 takes into account the two pumps constant phases.
Summing up and using $\Phi_i = 3\Phi_s - \Phi_{p1}$, we can write the signal at the output A_s as:

$$A_s \approx \left[B(t)e^{-i(\Phi_s)} + C_1(t)e^{i(\Phi_i)}\right]e^{-i\omega_2 t} = \left[B(t)e^{-i(\Phi_s)} + C_2(t)e^{-i(-3\Phi_s)}\right]e^{-i\omega_2 t}, \quad (4.2)$$

where $B(t)$, $C_1(t)$ and $C_2(t)$ are opportune complex functions with a constant phase. Formula (4.2) is consistent with what described in [11].

For suitable choices of the waves powers, the signal and its conjugate third harmonic interfere constructively for $\Phi_s = k \cdot \pi/2$ and destructively for $\Phi_s = (2k+1) \cdot \pi/4$. For values of Φ_s in between a re-alignment takes place as shown in Figure 4.4. The role of Φ_0 has been neglected since it only shifts the interference pattern in phase.

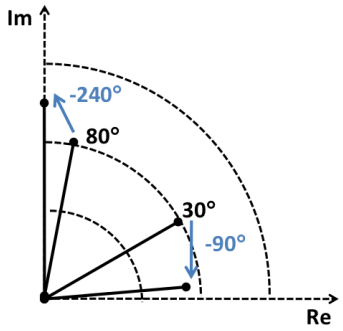

Figure 4.4: Realignment due to interference in the PS-FOPA as in [11].

Note that the ω_{ijj} contributions that have been neglected, i.e. $\omega_{211}, \omega_{233}, \omega_{244},$, are characterized by a phase equal to Φ_s so do not affect the results of our analysis.

4.3 Static Curves

The scheme has been described and its potential for QPSK signal regeneration has been semi-analytically proven. In this Section then we numerically investigate the static gain and phase response. The simulations are carried on sweeping the phase of a CW signal injected into the regenerator. The propagation is solved using the Split-step Fourier method of Appendix B and the results are shown in Figure 4.5 together with the trends reported in [11].

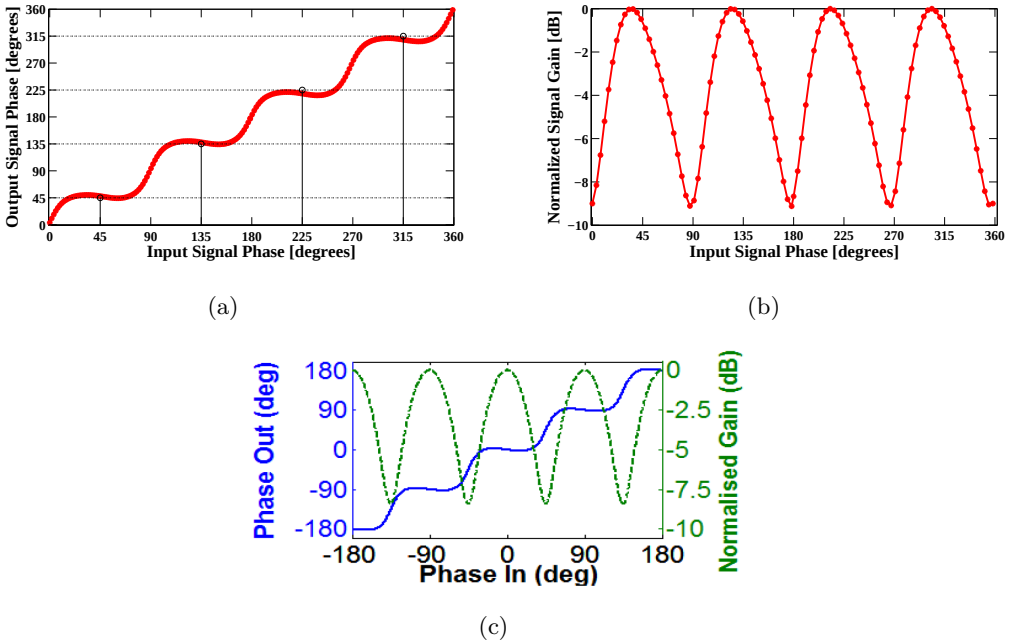

(a) (b)

(c)

Figure 4.5: Simulated output signal phase (a) and gain (b) as a function of the input signal phase. Semi-analytical curves (c) calculated in [11].

As can be seen in Figure 4.5(a), the phase shows four well-defined steps $\pi/2$-spaced both in values and input signal phase. Comparing the results with 4.5(c), a $\pi/4$ shift of the static curve is visible. This has been achieved for an opportune choice of the phase of pump 1. Having the steps centered at $(2k+1)\pi/4$ allows direct regeneration of a standard QPSK signal[1].

The gain of Figure 4.5(b) follows the phase profile. The gain curve is characterized by

[1]Here the expression "standard QPSK" refers to a QPSK signal with constellation states at $\pm\pi/4$ and $\pm 3\pi/4$.

peaks aligned to the phase flat zone and valleys to the phase transitions. The extinction ratio value of our simulated gain is not comparable with the semi-analytical derivation of [11] but the trends are indeed the same.

To conclude, both the simulated gain and phase response are promising for QPSK regeneration. In order to get a better insight of the regeneration process however, we can evaluate the constellation diagrams at input and output of the regenerator simply propagating a QPSK signal with added phase noise. The results of this first test are shown in Figure 4.6.

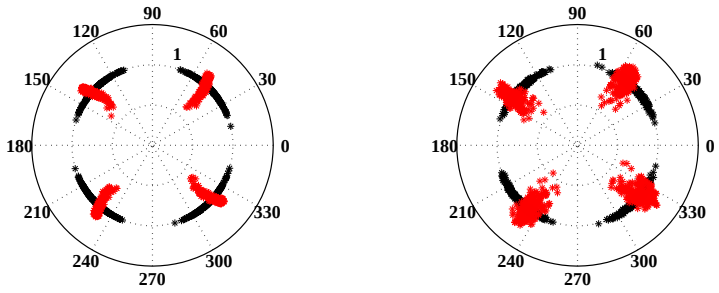

(a) (b)

Figure 4.6: Normalized constellation diagrams at the input (black) and output (red) of the regenerator for an input phase std σ_1 = 10° and a baudrate of 28 (a) and 40 (b) Gbaud.

The phase noise has been added to the QPSK signal injecting it into a phase modulator driven by white Gaussian noise spanning up to 20 GHz and with a std of 10°.

For both baudrates, the signal at the output of the regenerator indeed shows a lower phase variation. The drawback is however an increased amplitude noise resulting from the gain shape. To avoid amplitude variations in fact, the gain should be constant throughout (at least) the phase flat-zone.

A significant baudrate impact can finally be noticed. The performances of the scheme, including the baudrate dependence, are assessed in Chapter 6 together with the analysis of the other regenerator presented in Chapter 5.

4.4 Further Improvements

Two main directions have been proposed to improve this scheme: the extension to other MFs and the possibility to provide PSA without the need to inject an idler. These possible features are analyzed in the following Subsections.

4.4.1 Higher Order Modulation Formats

The potential to extend this configuration to a generic M-phase shift keying (PSK) signal has been suggested in [11]. To verify this possibility we have simulated the regenerator changing the position of the filters in the WDM de-multiplexer and adjusting the signal power.

Figure 4.7 shows the static curves for two different cases.

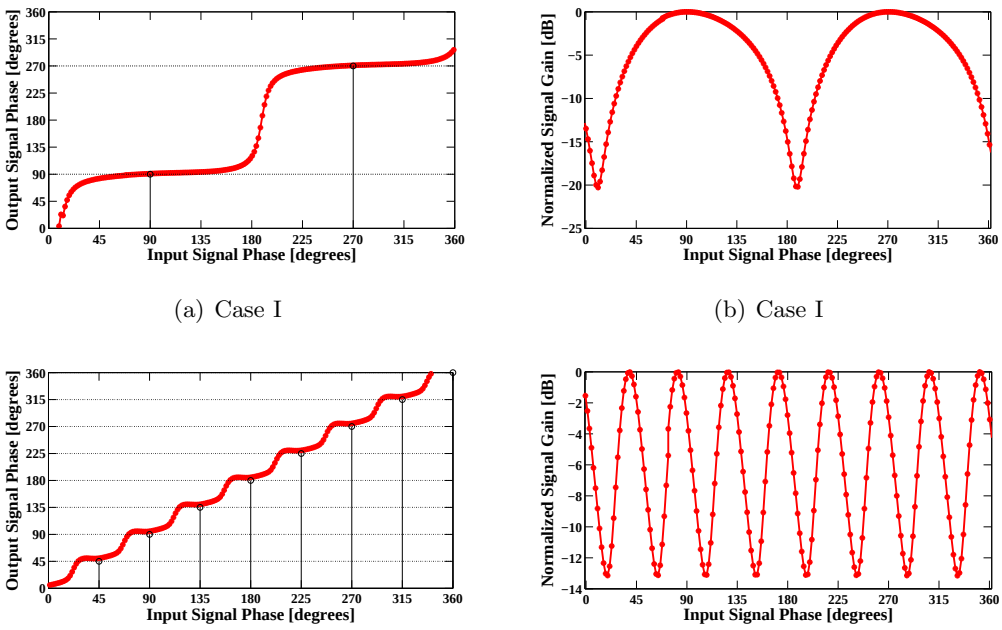

(a) Case I

(b) Case I

(c) Case II

(d) Case II

Figure 4.7: Output signal phase (a)-(c) and gain (b)-(d) as a function of the input signal phase.

Figures 4.7(a) and 4.7(b) show phase and gain profile when the DP FOPA is degenerate, i.e. signal and idler are at the same frequency. The signal power in input to the first

HNLF is set to 14 dBm. Higher power values cause saturation effects distorting the phase flatness. A DP degenerate FOPA has already been discussed in Section 3.3 and its performances for DPSK regeneration have been reported.

Figures 4.7(c) and 4.7(d) show phase and gain profile when the harmonics considered as idler and pump are the 7th and 8th harmonics: $\omega_i = \omega_s + 6(\omega_s - \omega_{p1})$ and $\omega_{p2} = \omega_s + 7(\omega_s - \omega_{p1})$.

The phase shows $\pi/4$-spaced levels and the gain follows the same trend with $\pi/4$-periodically spaced peaks and dips. Such profiles thus seem promising for 8-PSK regeneration. A slightly higher (24 dBm) signal power in input to the first HNLF is needed to generate up to the 8th harmonic in the first stage, but still within the reach of a standard EDFA.

To sum up, the scheme has been adapted to potentially operate for three different MFs only adjusting the signal power and the filters central position showing a high degree tunability.

4.4.2 Idler-free Scheme

In a recent paper by the same authors proposing the original method, QPSK regeneration has been experimentally demonstrated through a variant of the QPSK regenerator with no idler at the input of the second HNLF [43].

To investigate the proposed modification, the same system described above has been simulated removing the first HNLF and injecting signal and the two pumps directly into HNLF 2. Figure 4.8 shows the static curves for this idler-free scheme.
Figures 4.5 and 4.8 indeed show the same trends for both phase and gain responses.

This behavior seems to disagree with the theory of PI and PS-FOPA. In Section 2.3 we have stated the need to inject both idler and signal in order to obtain PSA. To understand this incongruity, the waves propagation inside HNLF 2 is investigated. The simulations are carried on with the usual fixed-step version of the Split-step Fourier method (Appendix B).

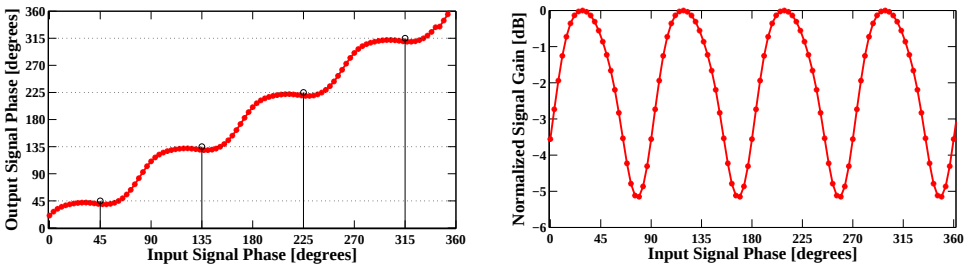

(a) (b)

Figure 4.8: Simulations of the idler-free scheme: output signal phase (a) and gain (b) as a function of the input signal phase.

First of all the absence of numerical artifact increasing the FWM efficiency and thus invalidating the results is verified using different step sizes for the Split-step [46]. Signal and idler powers as function of the position in the fiber are shown in Figure 4.9.

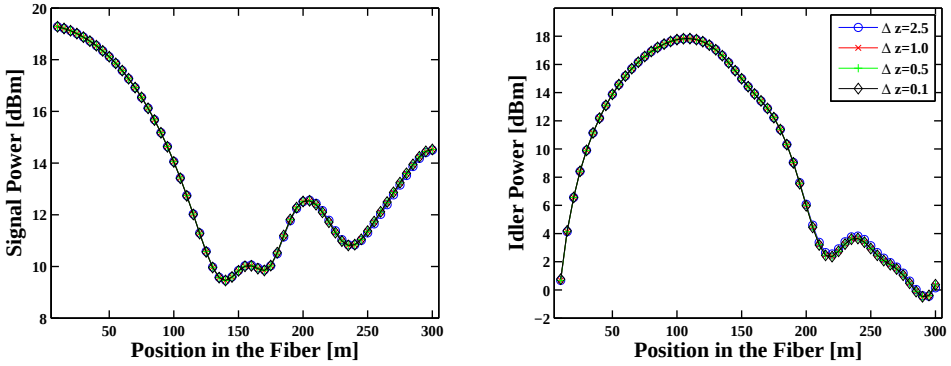

(a) (b)

Figure 4.9: Signal (a) and idler (b) power as function of the position in the fiber for various values of the step size Δz.

Both signal and idler show indeed the same trend regardless of the step size. The absence of numerical artifact is then proven. Rather than the power, however, we can analyze the power spectral density evolution through the fiber as in Figure 4.10. For clarity only a small (10 m) section at the beginning of the fiber is plotted.

The graph shows clearly that the generation of the idler takes place almost instantaneously. The fast growth is visible also in Figure 4.9(b) and may be caused by the

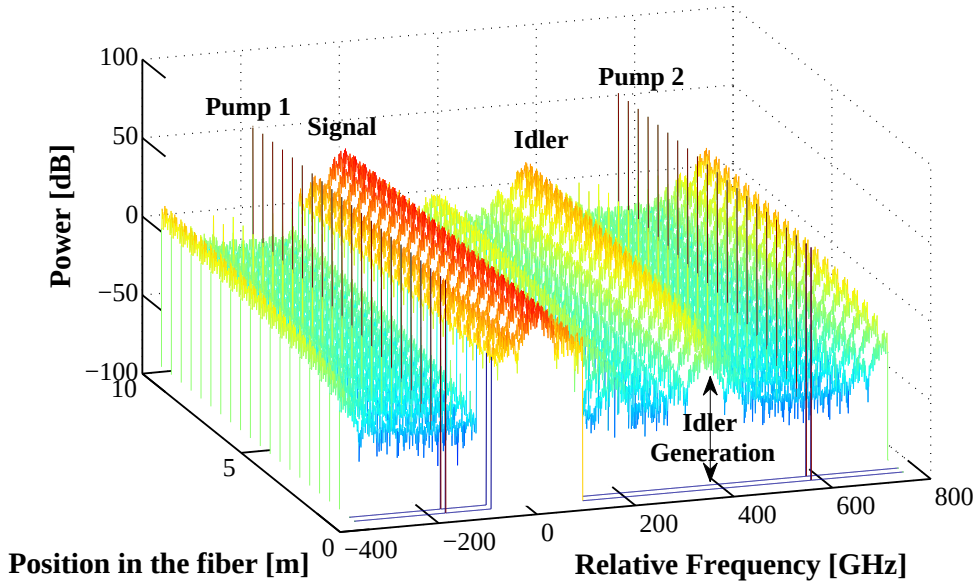

Figure 4.10: Simulated power spectral density as a function of the position inside the fiber. The step size for the Split-step Fourier method is set to 0.5 m and the frequencies are relative to the signal frequency.

contribution of more effects than only the standard two pumps PIA. Due to a signal stronger than the pumps, additional contributions as FWM between the signal and pump 1 alone, as previously in HNLF 1, are likely to take place.

The discrepancy with the simplified analysis of Section 2.3 is therefore related to the assumptions in the theoretical model. The expressions for the gain derived there rely both on perfect phase matching $\Delta\beta = 0$ and most importantly on undepleted pumps.

Further studies are however required to increase the understanding of the different processes involved. An analysis using the six-wave model of [15] may provide a more comprehensive description of the interaction.

The possibility of using a idler-free configuration allows to greatly simplify the first stage. Only the two phase-locked pumps are needed and they can be generated in an easier way through a comb generator [43].

As a last remark, our simulations showed one main drawback. In 4.5(b) and 4.8(b) only the normalized gain is shown to allow an easier comparison. When the idler-free configuration is used however the peak gain is decreased from around -3 to around -7 dB. An amplifying stage might thus be needed at the output of the idler-free regenerator with consequent ASE noise added to the signal. This situation requires a careful trade-off between the lower complexity of the setup and the need for noisy amplification.

Chapter 5

Dual Pump Degenerate FOPAs for QPSK Regeneration

In this chapter we propose and analyze a novel scheme for QPSK regeneration using saturation effects in two DP degenerate signal-idler FOPAs used in an interferometric configuration. In Section 5.1 we begin our investigation with some consideration on gain saturation in DP degenerate FOPAs, elaborating the ideas reported in [12] and evaluating the gain profile as function of the main fiber and system parameters. Then, Section 5.2 presents our proposed regeneration scheme and Section 5.3 shows gain and phase response to demonstrate the potential for QPSK regeneration. Finally the use of an amplitude limiter as a second stage is discussed in Section 5.4.

5.1 Gain Saturation in DP Degenerate FOPA

Saturations effects in a DP degenerate FOPA have been studied in [12], so as a starting point in our investigation, the model of [12] has been reproduced.

Similarly to the DP non-degenerate scheme of Chapter 4, also this system is made of two stages. A first HNLF with injected the signal and a CW pump is used to generate a second pump fulfilling the phase-locking requirements. Then an array waveguide grating (AWG) is used to multiplex signal and pumps together and inject them inside the second HNLF where the saturation effects take place.

The first stage is comparable with the one analyzed in Chapter 4. Our main interest

is studying the effects of saturation on the gain response of the DP FOPA so we focus only on the second stage. In our simulations only the second HNLF has been modeled and a second pump has been simply generated as a CW signal at $\omega_{p2} = \omega_s + \Delta\omega$ with $\Delta\omega = \omega_s - \omega_{p1} = 200$ GHz. The fiber parameters are reported in Table 5.1.

Length	177	m
Losses	15	dB/km
Nonlinear coefficient	7.1	$W^{-1}{\cdot}km^{-1}$
Dispersion at 1562 nm	-0.13	ps/nm·km

Table 5.1: Fiber parameters for saturation analysis in DP degenerate FOPA [12].

The high losses are caused by the Al-doping used to increase the SBS threshold power (SBST) (see Chapter 7).

In order to analyze the saturated PS gain, a CW signal wave at $\lambda_s = 1558.75$ nm with a linearly modulated phase Φ_s is injected into the HNLF together with the two pumps. At the output the signal is selected with an BPF of 200 GHz of FWHM bandwidth. The dispersion slope at 1562 nm is set to 0.011 $ps/nm^2{\cdot}km$ as in the similar fiber of [47]. The total power at the input of the fiber is set to $P_T = 33$ dBm and various values of the signal-to-pump ratio (SPR) are simulated. The SPR is defined as the signal power normalized to the power of a single pump and the two pumps are carrying the same power.
The results are illustrated in Figure 5.1(a). The gain is normalized to allow the comparison both between the different SPR values and with Figure 5.1(b) from [12].
The curves numerically simulated through our model (Figure 5.1(a)) and the ones presented in [12] (Figure 5.1(b)) indeed show comparable trends. Some discrepancies are expected due to the lack of knowledge on the ZDW and dispersion slope of the fiber used in the experiment. For both sets of data however, as the signal power increases the gain profile starts to display a valley on one side of the peak. The valley grows deeper for high SPR giving rise to a secondary peak next to the main one, other than shifting the maximum to higher input phase values.

Adjusting opportunely total power and SPR, a gain profile with $\pi/2$-spaced peaks having the same amplitude can be designed. Such profile is suggested in [12] to have the potential to provide QPSK signal regeneration.

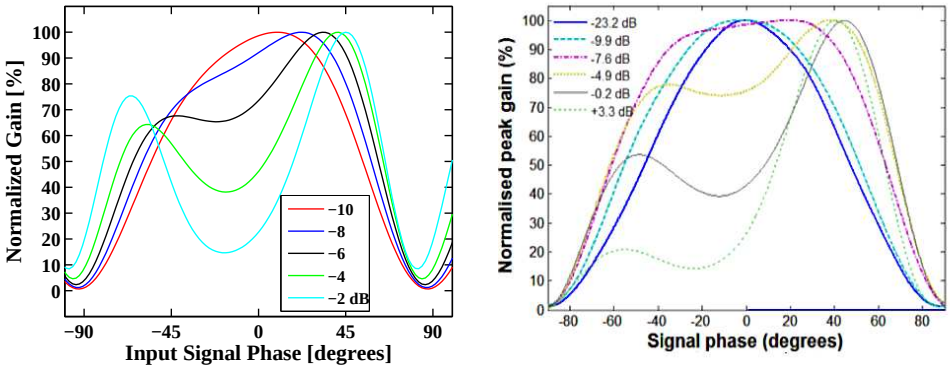

(a) (b)

Figure 5.1: Saturated gain in a DP degenerate FOPA for various SPRs: simulations (a) for a total power of 33 dBm and experimental results (b) from [12] for a total power of 32 dBm.

Such interesting opportunity is here investigated. We start our study with assessing through numerical simulation the influence some fiber and system parameters have on the gain shape in the saturated regime. The spanning range of the fiber parameters is chosen to be consistent with HNLFs, and the system parameters with usual values in optical communication systems.

In each Subsection only one explicitly stated parameter is varied, the other follow Table 5.1. This decision eases the analysis but, as drawback, removes the possibility to highlight combined effects. This study however does not have the pretension of being a rigorous analysis but aims only at giving a better insight on how the gain profile can be tailored with the different parameters. Even neglecting combined effects a good understanding can be gained.

Furthermore, unless stated otherwise, P_T = 35 dB and SPR=-5 dB, the specific choice of values is clarified later on in Section 5.3.

5.1.1 Gain Vs Nonlinear Coefficient

The nonlinear coefficient is the main parameter used to define FWM and thus parametric processes in FOPA. To analyze how strongly the gain shape is affected by variations in

the nonlinear coefficients, γ is varied from 5 to 20 $W^{-1}{\cdot}km^{-1}$. The results are illustrated in Figure 5.2

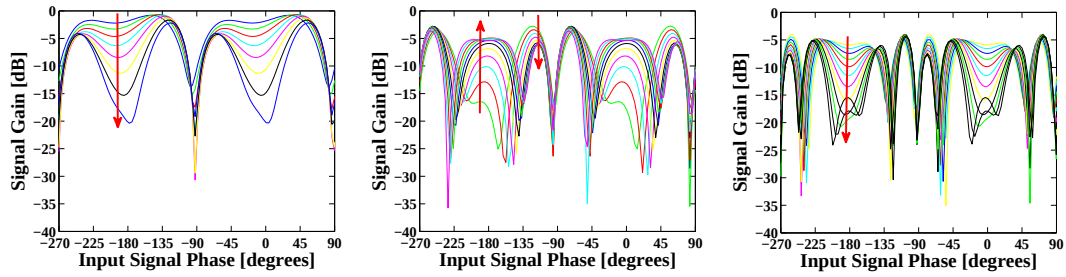

(a) (b) (c)

Figure 5.2: Saturated gain as a function of the input signal phase for various values of the nonlinear coefficient: $5 \leq \gamma \leq 8.5$ $W^{-1}{\cdot}km^{-1}$(a), $9 \leq \gamma \leq 14$ $W^{-1}{\cdot}km^{-1}$ (b), $14.5 \leq \gamma \leq 20$ $W^{-1}{\cdot}km^{-1}$ (c). The red arrows point towards the direction of increase of γ.

Starting from low values of γ (Figure 5.2(a)), the gain profile shows flat π-spaced peaks. As the nonlinear coefficient increases a valley appears in the middle of the peak and grows deeper. As γ keeps growing, a gain shape with $\sim \pi/2$-spaced peaks shape is shown. The peaks present a difference in the maximum values lower than 2 dB.
Proceeding further with Figure 5.2(b), higher values of the nonlinearities give rise to a secondary peak at the bottom of the valley. At the same time the highest peak is also reduced. Tuning accurately the value of γ the peaks can approach the same value[1].
Finally, as shown in Figure 5.2(c), for values of γ above 15 $W^{-1}{\cdot}km^{-1}$, the behavior is repeated. The middle peak is split into two by the growth of a deep valley. The total number of peaks is now four within a π signal phase shift. We stopped our analysis for $\gamma = 20$ $W^{-1}{\cdot}km^{-1}$ since it becomes challenging to achieve higher values of nonlinearities for standard HNLFs.

Nevertheless it is important to notice that the last two curves for $\gamma = 19.5$ and 20 $W^{-1}{\cdot}km^{-1}$ show a new peak making its appearance at the bottom of the valley. This whole process is thus likely to be repeated with a periodical increase in the number of peaks. The main drawback is however the of lack of symmetry of the obtained gain profile. The

[1]In this analysis we are assuming perfect tunability of the parameters, other than the parameters being independent from each other. This is usually not the case in designing optical fibers. Nevertheless our study could give some hints on how to design a desired gain profile.

spacing between the peaks is not constant, the maxima values are not equal and one side of the peaks drops more steeply than the other. Perhaps optimizing both γ and other parameters such drawback may be solved.

5.1.2 Gain Vs Fiber Length

The length of the fiber span together with γ determines the amount of nonlinear effect the signal undergoes to propagating through the FOPA. Different fiber lengths have been analyzed spacing from 10 m to 2 km. Three main situation have been distinguished: short fiber span, medium length and long fiber. The results are illustrated in Figure 5.3.

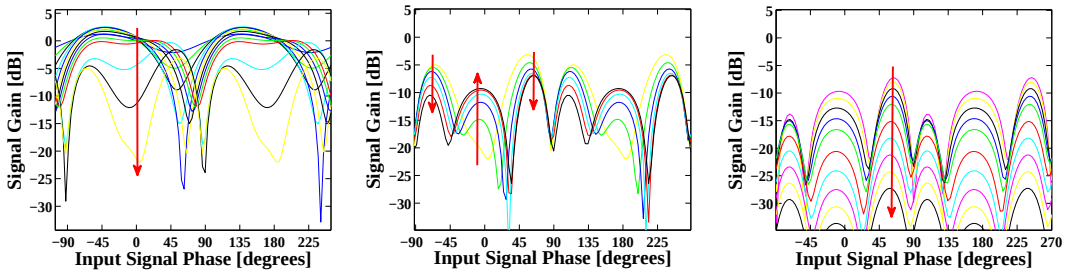

(a) (b) (c)

Figure 5.3: Saturated gain as a function of the input signal phase for various values of the fiber length: $10 \leq L \leq 250$ m (a), $300 \leq L \leq 550$ m (b), $0.6 \leq L \leq 2$ km (c). The red arrows point towards the direction of increase of L.

For a short fiber span, a small increase in length does not influences the gain in a significant way. Only when L reaches 100 m (red curve in Figure5.3(a)) a valley starts to grow in the π-spaced broad peaks. As for γ thus, the gain evolves towards a $\sim \pi/2$-spaced peak profile.

When the fiber length is increased further (Figure 5.3(b)), additional peaks start to grown within the valleys. The spacing between such peaks is around $\pi/3$. Furthermore, while the "new" peak grows the others are attenuated. For specific values for the length thus the relative maxima values can be equalized (e.g. black curve).

Finally for long fiber spans (Figure 5.3(c)) the main effect is only a down-shift of the gain curve. Losses become dominant over parametric processes.

Note that, even if for medium and short HNLFs the dependence of the gain on L is similar to the dependence on γ, the width of the peaks is more uniform varying L.

5.1.3 Gain Vs GVD

When it comes to parametric amplification, GVD has a strong influence. The dispersion coefficient D (A.5a) defines the phase-matching condition and thus the parametric processes efficiency. The dispersion coefficient at λ_s has then been swept from -3 to 3 ps/nm·km. As for the length and γ, also concerning the dispersion we can distinguish three ranges of values: normal dispersion $-3 \leq D \leq 0$ ps/nm·km, anomalous low dispersion $0 \leq D \leq 0.5$ ps/nm·km and finally anomalous dispersion $0.5 \leq D \leq 3$ ps/nm·km. The results are shown in Figure 5.4.

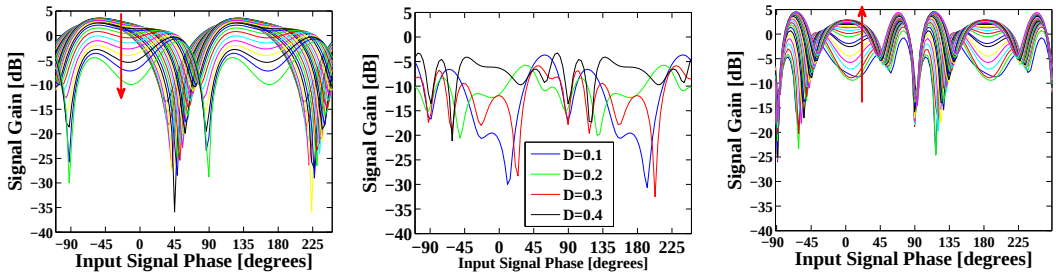

(a) (b) (c)

Figure 5.4: Saturated gain as a function of the input signal phase for various values of the dispersion at λ_s: $-3 \leq D \leq 0$ ps/nm·km (a), $0 \leq D \leq 0.5$ ps/nm·km (b), $0.5 \leq D \leq 3$ ps/nm·km (c). When no legend is shown, the red arrows point towards the direction of increase of D.

The results show a low impact on the gain when the signal is propagating in the normal regime $D < 0$ (Figure 5.4(a)). Only for values of the dispersion approaching zero a valley starts to perturb the π-spaced peaks. The gain profiles is then characterized by a $\sim \pi/2$-spaced peak profile.

For positive but small values of the dispersion the gain shows an irregular shape (Figure 5.4(b)).

Finally when the dispersion increases the evolution returns more regular and a peak grows from the bottom of the valley.

It is interesting to notice how the evolution of the gain profile for increasing values of the dispersion follows a similar trend as for γ and L. In particular the changes in shape are closer to the ones shown for the nonlinear coefficient, excluding the few cases of Figure 5.4(b). The gain curve shows a broad peak with two narrower and stronger side ones: Figure 5.4(c) is comparable with Figure 5.2(b).

5.1.4 Gain Vs Dispersion Slope

Similarly to the considerations made for GVD, also the dispersion slope (A.5b) is expected to have a strong influence on the gain profile. This is indeed demonstrated by the results in Figure 5.5 where the slope spans from -0.3 to 0.3 ps/nm^2·km while D at 1562 nm is kept at -0.13 ps/nm·km. As the slope of the dispersion profile changes though, also the ZDW is shifted.

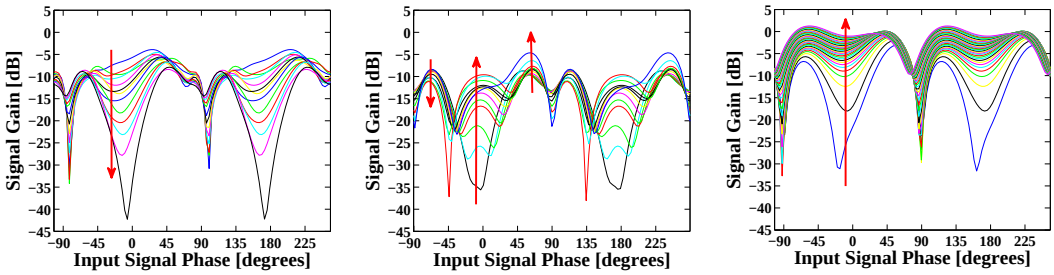

(a) (b) (c)

Figure 5.5: Saturated gain as a function of the input signal phase for various values of the dispersion slope at λ_s: $-0.3 \leq S \leq -0.18$ ps/nm^2·km(a), $-0.18 \leq S \leq -0.05$ ps/nm^2·km (b), $-0.04 \leq S \leq 0.3$ ps/nm^2·km (c). The red arrows point towards the direction of increase of S.

For a strongly negative dispersion slope (Figure 5.5(a)) the usual valley starts to grow deeper in the middle of what this time is a more irregular peak. The π-spaced peaks are not flat and show a strong asymmetry.

When the slope increases, i.e. the dispersion at the signal wavelength tends towards zero, a broad peak grows from the valley similarly to the gain evolution for dispersion and γ. At the same time however, one of the two already existing peaks is attenuated while other keeps growing slowly.

Finally for S=-0.04 ps/nm^2·km the is shifted ZDW at the signal wavelength. This value represents a discontinuity in the evolution. Comparing the curves for S=-0.05 ps/nm^2·km (blue curve of Figure 5.5(b)) and for S=-0.04 ps/nm^2·km (blue curve of Figure 5.5(c)), a strong difference in the gain shape can be seen. As the slope keeps increasing then the valley flattens out and the gain reverts slowly to a broad π-spaced peaks profile.

Unlike for the other fiber parameters analyzed, the evolution does not continue periodically but reverts back to the initial state.

5.1.5 Gain Vs Frequency Spacing

Figure 5.6 presents the gain calculated through the simulations carried on varying the spacing between signal and pumps. The frequency spacing range considered goes from 200 GHz up to 4 THz. A narrower spacing would indeed be challenging due to the strict requirements on the BPF bandwidth rather than the modulated signal spectral width, and a detuning above 4 THz, i.e. a total bandwidth of 8 THz, is likely to provide poor performances due to GVD: $\theta \approx \Delta\beta$.

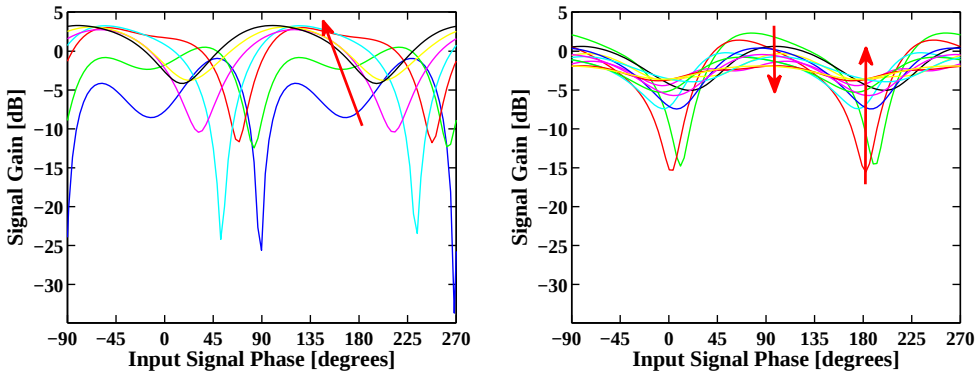

(a) (b)

Figure 5.6: Saturated gain as a function of the input signal phase for various values of the signal-pump frequency spacing: from 200 GHz to 1.4 THz (a), from 1.6 to 4 THz (b). The red arrows show the direction of increase of the spacing.

For frequency spacings between signal and pumps of the order of hundreds of GHz, the shape of the gain is strongly affected by the value of the detuning. The gain broadens out from $\pi/2$-spaced peaks to broader π-spaced peaks (Figure 5.6(a)).
For a larger spacing instead the phase periodicity of the oscillation is not affected by increasing the waves distance. Only the contrast is decreased eventually resulting in an almost flat gain profile (Figure 5.6(b)).

This behavior is consistent with the strong dependence of phase matching on GVD. When the waves are quite close in frequency, the detuning influences significantly the phase matching condition as the GVD varies. As $\Delta\beta$ becomes the dominant term in $\theta = \Delta\beta + \Phi_s - \Phi_{p1} - \Phi_{p2}$, however, the contrast is strongly reduced and the gain becomes almost phase insensitive.

5.1.6 Gain Vs Power

In this section P_T and SPR are not kept constant anymore. The gain is analyzed for different values of the total power P_T and the SPR: P_T spans from 31 to 35 dBm and SPR from -8 to 8 dB.

When the total power is quite low, both 31 and 32 dBm, the evolution of the signal gain shows the two main effects marked with arrows in Figure 5.7(a).

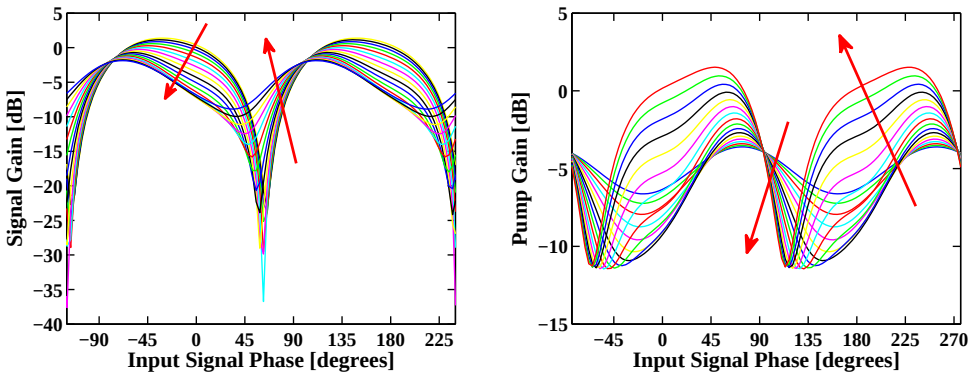

(a) Signal (b) Pump 1

Figure 5.7: Saturated signal (a) and pump (b) gain as a function of the input signal phase for values of the SPR from -8 to 8 dB and a total power of 31 dBm. The red arrows show the direction of increase of the SPR.

First of all for increasing values of the SPR the maximum gain becomes negative. The decrease on the maximum gain can be explained recalling the power saturation characteristic described in Figure 3.5. As the signal power is increased the output power saturates at a constant value and thus the gain eventually becomes negative. Intuitively, when the signal carries more power than the pumps, the photons flow from the signal to the pumps rather than vice versa. This scenario is confirmed by the pump gain becoming positive as shown in Figure 5.7(b).
Furthermore the contrast between gain peaks and valleys is reduced.

As the total power is increased to 33 and 34 dBm the additional effects already seen when analyzing the fiber parameters start to take place. As already illustrated for most of the parameters analyzed, a valley appears in the middle of the gain peak for high SPRs. For higher ratios and P_T = 34 dBm a secondary peak starts rising (Figure 5.8(b)).

With the growth of the secondary peak, the gain profile is characterized by $\pi/2$ spaced peaks.

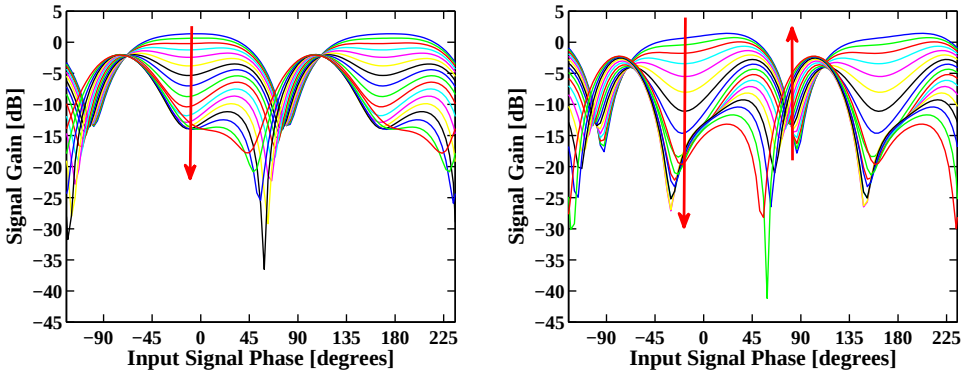

(a) (b)

Figure 5.8: Saturated signal gain as a function of the input signal phase for values of the SPR spanning from -8 to 8 dB and a total power of 33 dBm (a) and 34 dBm (b). The red arrows show the direction of increase of the SPR.

Finally, going up to P_T = 35 dBm and for values of the SPR, spanning from -8 to -3 dB, the generation of secondary peaks is accentuated and $\pi/2$-spaced peaks can be tailored as in Figure 5.9(a). Accurate tuning of the power allows to equalize the maximum of the peaks to the same values but is limited by a trade-off between equalization and contrast.

Increasing further the SPR, $\sim \pi/3$-spaced peaks with similar width rise (Figure 5.9(b)). As for the long fiber spans of Figure 5.3(c), equalization of the peak values results more challenging as the number of maxima increases.

Values of SPR above 4 dB have been neglected since the only effect shown is the flattening out of the gain as discussed for P_T =31 dBm.

5.1.7 Gain Vs Relative Pump Phase

In all the investigation presented so far the pump phases have been neglected as constant terms as long as they were locked with the signal phase. In this Subsection however we present a brief analysis to relate the relative pump phase $\Delta\Phi = \Phi_{p1} - \Phi_{p2}$ to the phase shift of the gain profile.

Figure 5.10 shows the gain profile for three cases: $\Phi_{p1} = \Phi_{p2} = \Phi_0$, $\Phi_{p1} = -\Phi_{p2} = \Phi_0$ and

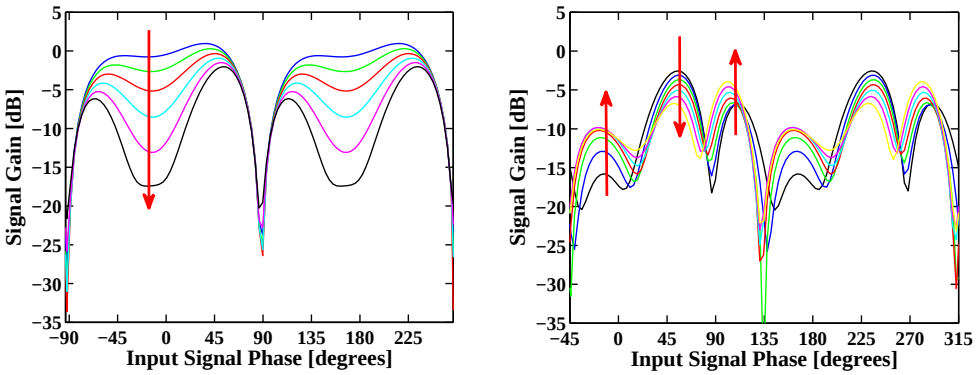

(a) (b)

Figure 5.9: Saturated signal gain as a function of the input signal phase for values of the SPR spanning from -8 to -3 dB (a) and from -3 to 4 dB (a) and a total power of 35 dBm. The red arrows show the direction of increase of the SPR.

$\Phi_{p1} = \Phi_0$, $\Phi_{p2} = 0$. For each case $\Phi_0 = 0, \pi/2, \pi$.

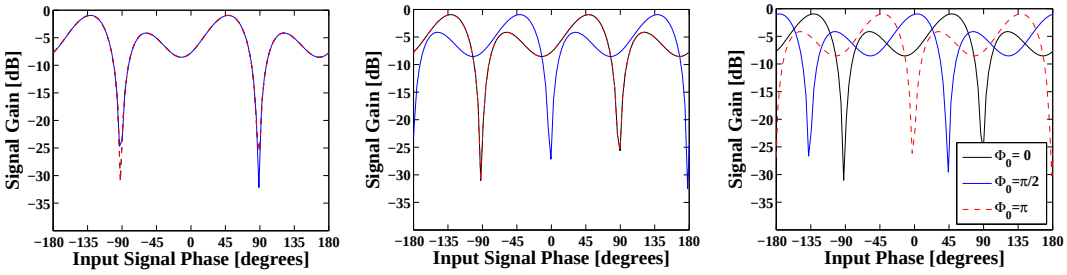

(a) $\Phi_{p1} = \Phi_{p2} = \Phi_0$ (b) $\Phi_{p1} = -\Phi_{p2} = \Phi_0$ (c) $\Phi_{p1} = \Phi_0$, $\Phi_{p2} = 0$

Figure 5.10: Saturated signal gain as a function of the input signal phase for $\Phi_0 = 0, \pi/2, \pi$.

Analyzing the reported trends we can see that:

- In Figure 5.10(a) the three curves are superimposed. When $\Delta\Phi = 0$ no phase shift of the gain is shown, regardless of the absolute phase of the waves.
- In Figure 5.10(b) the curves for $\Phi_0 = 0$ and $\Phi_0 = \pi$ are superimposed and the curve for $\Phi_0 = \pi/2$ is $\pi/2$ phase shifted. When $\Delta\Phi = 2 \cdot \Phi_0$, the gain profile is Φ_0-phase shifted.
- In Figure 5.10(c) the phase shift between the curves is $\pi/4$: the gain phase shift

thus correspond to $\Delta\Phi/2 = \Phi_0/2$.

Summarizing a relative phase between the pumps of $\Delta\Phi$ results in a phase shift of the gain profile of $\Delta\Phi/2$.

5.2 Regenerator Setup

In the previous Section we have shown that the gain can be tailored to show $\pi/2$-spaced peaks. This characteristic is indeed promising for QPSK signal regeneration as suggested in [12]. Nevertheless it is not sufficient, we need to investigate the main property required for QPSK regeneration: a step-like phase response with levels $\pi/2$ spaced in both input signal phase and value. Figure 5.11 reports normalized gain and output signal phase as function of the input signal phase for $P_T = 35$ dBm and various SPR.

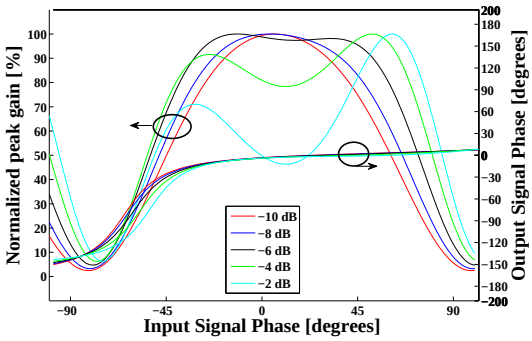

Figure 5.11: Saturated gain and output signal phase as a function of the input signal phase for various SPRs and a total power of 35 dBm.

As can be seen, the phase trend is not significantly affected by saturation. This result was actually already hinted in [10] where it is stated that pump depletion has no impact in the phase response.

Such results indeed demonstrate that saturation in a DP degenerate FOPA does not provide all the characteristics required to perform QPSK regeneration.

Nevertheless, within the effects of saturation described in the previous Section, two are indeed promising for our goal:

- A gain profile with $\pi/2$ spaced peaks can be achieved, as in Figure 5.11.
- A relative phase between the two pumps of $\Delta\Phi = \pi$ results in both a phase-shift of the gain curve (Figure 5.10) and a down-shift of the phase characteristic of exactly $\pi/2$.

Our proposal is thus to use two DP degenerate FOPAs inside a MZI. The amplifier in the upper arm should take care of squeezing the constellation along the in phase component of the QPSK signal while the one on the lower arm should act upon the orthogonal in quadrature component. In our scheme this effect is achieved using the same fiber in both arms but with the relative pump phases fulfilling $\Delta\Phi_{upper} = \pi + \Delta\Phi_{lower}$. Gain and phase response in the two arms are thus $\pi/2$ phase shifted.

The use of a FOPA-based MZI follows an approach similar to [41] reported in Section 3.4. The main difference however is the type of FOPA used. In [41] degenerated signal-pump FOPAs are used, with a length of 6 km each and a nonlinear coefficient as high as 27 $W^{-1}{\cdot}km^{-1}$. Following our approach instead we require only two HNLFs of 177 m and with $\gamma = 7.1$ $W^{-1}{\cdot}km^{-1}$.
Furthermore also in [42] a scheme similar to our proposal is presented. There however, no saturation effects are mentioned.

The process is conceptually described through the constellation diagrams in Figure 5.12.

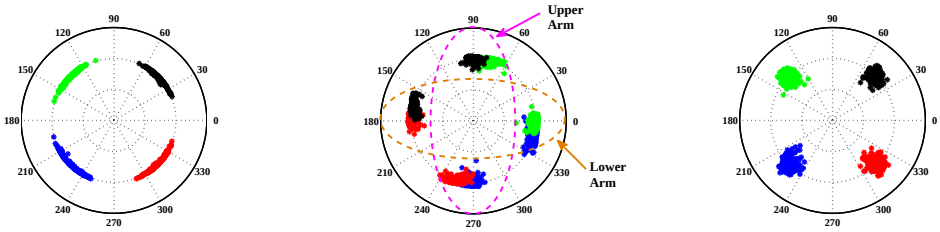

(a) (b) (c)

Figure 5.12: Depiction of target constellation diagrams at the input of the MZI (a), in the two arms (b) and at the output of the MZI (c). The samples are grouped by color according to their initial noise-free state.

Figure 5.12(b) shows the squeezing process taking place in the two arms: in one arm the constellation points are squeezed along $0 \rightarrow \pi$, in the other along $\pi/2 \rightarrow 3\pi/2$.

The target gain and phase response to achieve such effect are shown in Figure 5.13.

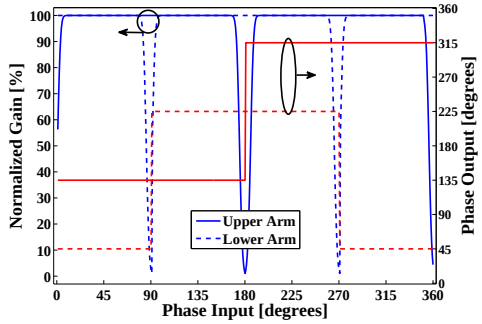

Figure 5.13: Target gain and phase responses as function of the input signal phase in the two arms.

In each arm the output phase should show a staircase profile with π-spaced level, while the gain should be characterized by a flat profile. Only narrow gain transitions aligned with the phase transitions are tolerated since they are expected to be impossible to suppress. The gain in the two arms needs to be equalized for all the four states of the QPSK signal. Different amplification levels result in amplitude noise when the fields of the two arms interfere at the MZI output.

The configuration we propose to implement this scheme is shown in Figure 5.14.

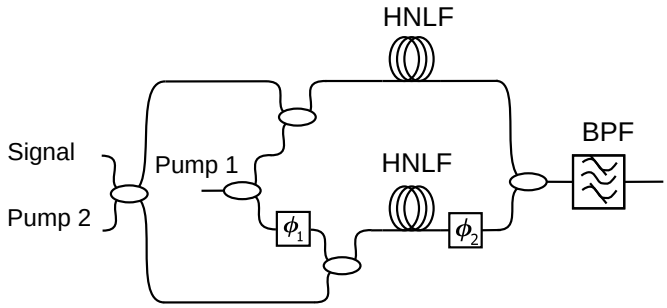

Figure 5.14: Proposed setup for a QPSK regenerator using saturation in a DP degenerate FOPA inside an interferometer. The two phase shifters are marked as Φ_1 and Φ_2.

Two phase-locked pumps are coupled in the interferometer together with the signal such that the signal and pump 2 co-propagate with pump 1 in the upper arm and its

π-phase shifted version in the lower arm ($\Phi_1 = \pi$). The frequency spacing has been optimized at 350 GHz. The HNLFs in the two arms are identical and for consistency characterized by the same parameters of [12] already reported in Table 5.1, Only the reference wavelength for D and S, not mentioned in [12], has been changed to 1550 nm [47]. Then, the outputs of the two FOPAs are coupled together and the signal is selected with a third order Gaussian filter of 175 GHz FWHM bandwidth.
Note that the second phase shifter in the lower arm (Φ_2) is used to compensate the $\pi/2$ phase rotation caused by the last 3-dB coupler.

In Figure 5.14 we have neglected the pre-stage for the generation of the two phase locked pumps. This can be easily implemented through the technique proposed in [43], i.e. a frequency comb generator followed by injection-locked lasers to remove the phase noise.
As a last remark, the use of a MZI with two identical arms sets strict and potentially unrealistic requirements on the scheme. Nevertheless mapping the MZ into a SI, it could be implemented with one single HNLF and thus relieving significantly the constrains.

5.3 Static Curve

From the gain profiles shown in Section 5.1, it can be expected that the scheme of Figure 5.14 only allows to approach the target responses of Figure 5.13 even optimizing the power levels at the input of the HNLFs.

Figure 5.11 hints that π-wide peaks cannot be achieved even through saturation. The proposed strategy is thus to use a gain profile with equalized $\pi/2$ spaced peaks.
It is worth remarking however that equalization is not the only goal, also a step-like phase profile is required. A compromise between the phase flatness and the gain equalization is required.
Furthermore, it should be remembered that symmetry in the two arms is crucial for the operation of the scheme. The proposed configuration thus provides only two degrees of freedom for the optimization: total power and SPR need to have the same value at the input of both HNLFs.

The optimized trends for P_T =35 dBm and SPR=-5 dB are shown in Figure 5.15.
The trade-off is clearly visible by the need to accept a gain profile showing a 50% gain

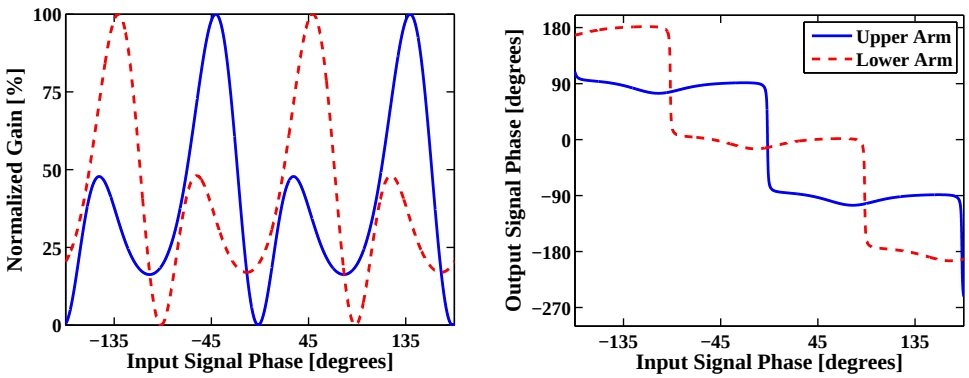

(a) (b)

Figure 5.15: Normalized gain (a) and output signal phase (b) as function of the input signal phase for the upper (continuous) and lower (dashed) arm.

.

difference between secondary and main peak in order to achieve a flat phase response. Furthermore, a higher secondary peak could be designed lowering the SPR but such peak would be also shifted close to the main one and thus not anymore $\pi/2$ spaced. The alignment between secondary peak of one arm and main peak of the other is critical in order to keep low the phase-to-amplitude noise conversion.

The overall static curves of the MZI are shown in Figure 5.16.

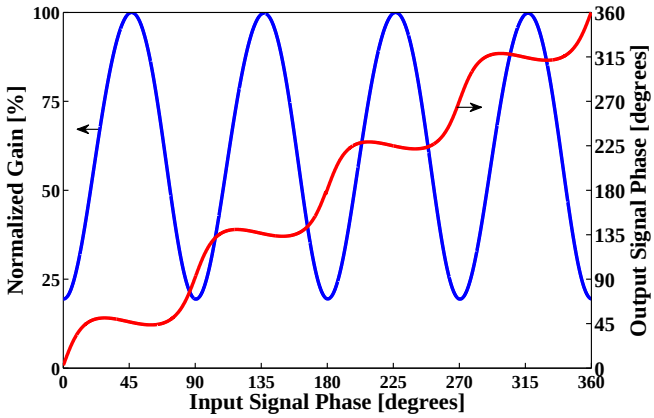

Figure 5.16: Static curves of the proposed regenerator scheme with the optimized parameters $P_T = 35$ dBm and $R = -5$ dB.

A flat step-like phase profile has been designed and the equalized gain shows an extinc-

tion ratio of around 6 dB.

Comparing the static curved obtained with the target trends of Figure 5.13, the main difference is related to the non-constant gain. Gain variations cause partial phase-to-amplitude noise conversion.

The analysis of the performances is reported in Chapter 6 together with the evaluation of the regenerator of Chapter 4. We can however test the system simply replacing the CW with a QPSK signal with added phase noise. The comparison of the constellation diagrams at input and output of the regenerator is shown in Figure 5.17.

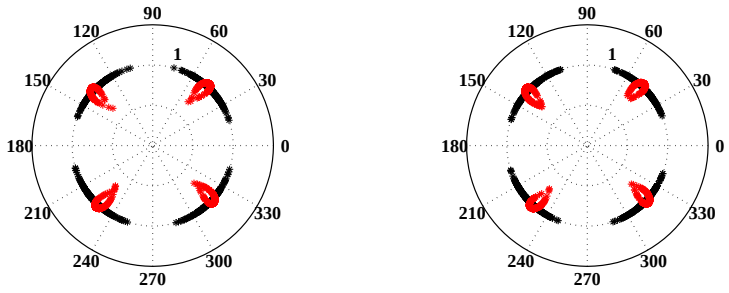

(a) (b)

Figure 5.17: Normalized constellation diagrams at the input (black) and output (red) of the regenerator for input signal phase std $\sigma_i = 10°$: 28 (a) and 40 (b) Gbaud.

The phase noise is obtained phase modulating the signal with white noise spanning up to 20 GHz and a noise std of 10°. The constellation diagrams have then been generated sampling the optical signal in the center of the symbol slot for both input and output of the regenerator. To provide a meaningful comparison the amplitude has been normalized.

Figure 5.17 indeed shows a decrease in the phase noise and at the same time highlights the increased variance in amplitude. Regardless to the baudrate, both simulations show clearly the phase squeezing and amplitude un-squeezing effects.

In general to limit this undesired increase of amplitude noise, a power limiter can be used at the output of the phase regenerator. This is discussed in the next Section.

5.4 Two-stage Regeneration

The use of amplitude limiters to remove intensity noise from an optical signal has been introduced in Section 3.2.

Here we re-propose the scheme of [28] adapted to be used for intensity noise suppression at the output of our phase regenerator. The parameters for the HNLF are the same as [28], only the dispersion profile has been up-shifted in wavelength to keep the same dispersion value at the signal wavelength. Fiber ZDW, dispersion slope, nonlinearity, losses, and length are respectively λ_0 = 1556 nm, S=0.026 ps/nm^2·km, γ=12 W^{-1}·km^{-1}, α=0.78 dB/km, and L=150 m. As far as the 20 mW pump is concerned the 600 GHz-detuning has been conserved setting λ_p = 1563.6 nm.

Figure 5.18 shows output signal power and phase as a function of the input signal power when a CW signal is propagating through the FOPA.

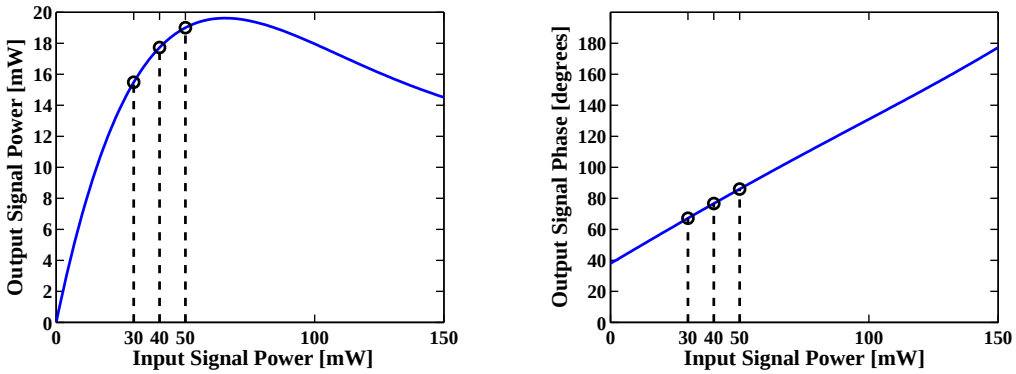

(a) (b)

Figure 5.18: Output signal power (a) and phase (b) as a function of the input signal power. Our chosen operating points are also marked in the plots.

Three different operating points for the input signal power P_s=30, 40 and 50 mW have been chosen from the saturation curve. These point have been selected close but not above the saturation power because we work with average powers. The peak power then falls in the saturation region.

To evaluate the potential of adding such additional stage after the phase regenerator we have calculated the static curves of the whole setup of Figure 5.19.

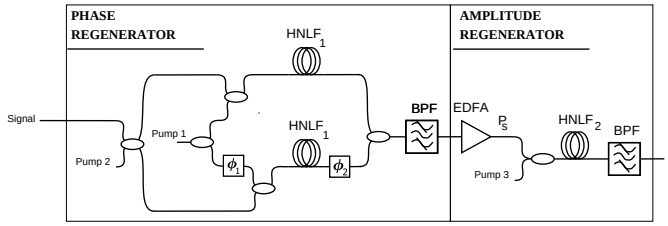

Figure 5.19: Proposed setup for the two-stage regenerator: phase and amplitude regeneration are performed sequentially.

The scheme responses for different P_s values are illustrated in Figure 5.20

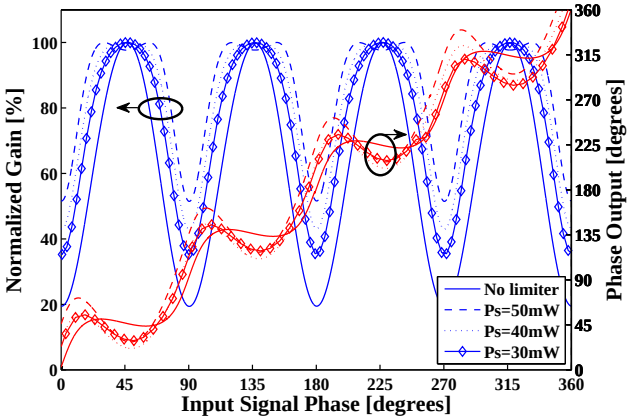

Figure 5.20: Static curves for the two stages system. Four scenarios are shown: no amplitude regenerator (continuous), average input signal power of 30 mW ($\diamond$), 40 mW (dotted), 50 mW (dashed).

As we can see, the gain profile is broadened when the amplitude regenerator is used. Furthermore, the higher P_s, the broader the gain. When the input power becomes too high though, the gain starts to be distorted acquiring a "horned" shape. This effect actually appears already for P_s =50 mW, but the output power variation is below 3%.

A broader gain indeed provides a lower intensity noise. As the gain is broadened however, the output phase deviates from the step-like profile with slow oscillations replacing the flat step. The amplitude of the oscillation increases together with the gain bandwidth for increasing P_s. The larger the oscillation, the lower the phase noise suppression, so once again balance between phase and amplitude regeneration is called for.

Constellation diagrams at input and output of phase and amplitude regenerators are shown in Figure 5.21.

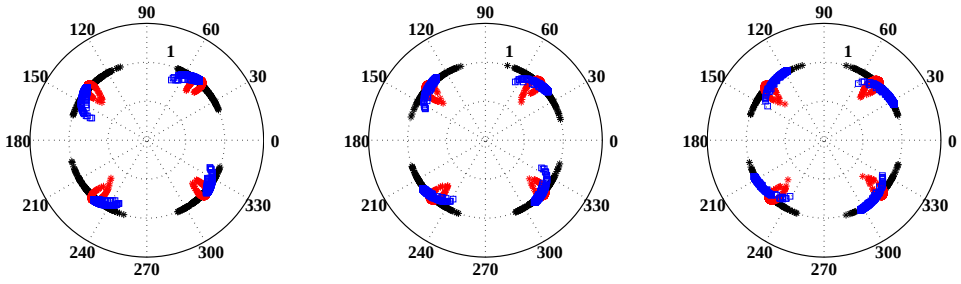

(a) (b) (c)

Figure 5.21: Constellation diagrams at input (black) output of first (red) and second (blue) stage for input signal phase std $\sigma_i = 10°$: average input signal power 30 mW (a) 40 mW (b) and 50 mW (c) at 28 Gbaud.

The comparison shows indeed a reduction of the amplitude noise at the output of the amplitude regenerator but it also remark the re-introduction of part of the phase noise. Nevertheless the phase variations at the output of the second stage are lower than at the input of the phase regenerator.

Furthermore, the compromise between amplitude and phase noise discussed above is shown by the three constellation diagrams. The amplitude noise reduction increases with the increased input power to the detriment of a decrease in the phase squeezing.

The performances analysis for the two-stage regenerator is shown in Chapter 6 as well.

Chapter 6

Simulation Results

In this chapter we analyze the performances of the QPSK signal regenerators presented in Chapters 4 and 5. First in Section 6.1 the setup of the system used for our evaluation is described. Next, in Section 6.2 the effectiveness of the DP non-degenerate FOPA regenerator of Chapter 4 is estimated through the analysis of both the improvement in the phase std and in the BER. The same investigation is then reported in Section 6.3 for the DP degenerate FOPA-based MZI regenerator of Chapter 5 and the comparison between the schemes is provided. Finally Section 6.4 summaries the main results.

6.1 System Setup

In this Section we present the system we modeled in MATLAB® .
The main blocks of the our setup are shown in Figure 6.1.

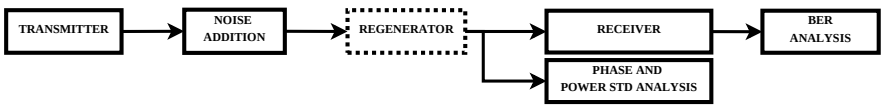

Figure 6.1: System setup.

First a QPSK signal is generated in a MZM-based transmitter. Then a second stage adds phase and, for some analysis, amplitude noise. Finally the noisy signal is propagated through a regenerator and the performances of the output are evaluated analyzing both the std of signal phase and power and the BER calculated injecting the signal into a balanced QPSK receiver. Comparison is carried on between the performances with and

without a regenerator. In the latter case, the noise-addition block is connected directly to receiver and signal phase and power analyzer.
These block, with the exception of the already deeply discussed regenerator, are analyzed in the following subsections.

6.1.1 Transmitter

The implementation of our QPSK transmitter is shown in Figure 6.2.

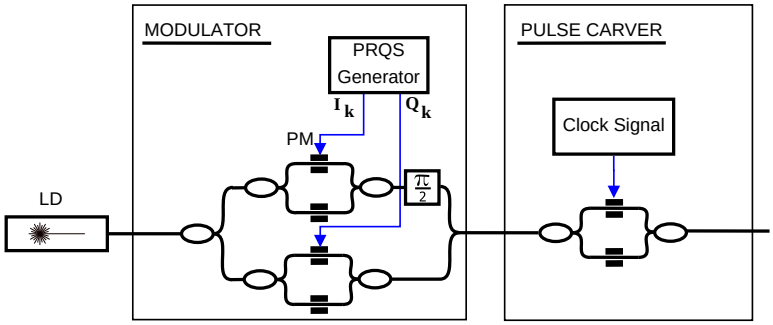

Figure 6.2: QPSK signal transmitter scheme.

The transmitter is composed by a ideal LD with zero-linewidth, an electrical signal generator ("PRQS generator") providing the data, a modulator block modulating the electrical data into the optical signal and a pulse carver shaping the optical pulses according to the desired MF.
The QPSK modulator is made of two parallel MZM-based binary phase shift keying (BPSK) modulators in a "super-MZM" structure. A $\pi/2$ phase shift is introduced between the arms in order to have the in-phase component of the signal modulated by one MZM and the orthogonal in-quadrature component by the other.
For clarity in Figure 6.2 only one arm of each MZM is connected to the driving voltage. All the MZMs used in the transmitter (two in the modulator and one as pulse carver) are however driven in push-pull operation[1] to avoid frequency-chirping of the signal.
The signal at the output of the modulator can be expressed as [48]:

$$E(t = t_k) = E_0 \cos\left(\frac{(I_k - Q_k)\pi + \frac{\pi}{2}}{2}\right) e^{i\left(\frac{(I_k - Q_k)\pi + \frac{\pi}{2}}{2}\right)} \tag{6.1}$$

[1] A MZM is driven in a push-pull operation when the driving signals of the PM in the upper arm ($V_{01} + V_1(t)$) and the signal driving the lower arm ($V_{02} + V_2(t)$) satisfy $V_1(t) = -V_2(t)$. One arm is driven by the data, the other with the complementary of the data.

This specific modulation is known as non return to zero (NRZ)-QPSK. Figure 6.3 shows the constellation and phase eye diagrams for such a signal.

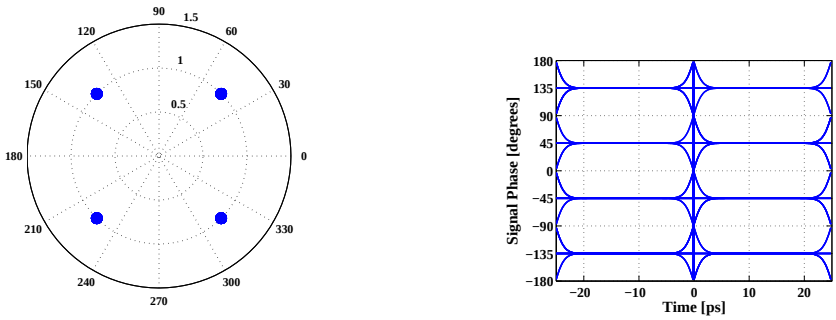

(a) (b)

Figure 6.3: Constellation (a) and phase eye (b) diagrams for a 40 Gbaud NRZ-QPSK signal. The four states of the constellation diagram have been plotted with big markers for the sake of clarity. They are in fact four single states with equal power (here normalized) and phase $(2k+1)\pi/4$.

After the modulator, a pulse carver sinusoidally driven at half of the baudrate, is used to shape the optical signal. This block allows to generate also return to zero (RZ) 33%-QPSK and carrier-suppressed return to zero (CSRZ)-QPSK signals.
Constellation and phase eye diagrams are the same shown in Figure 6.3 also for RZ 33% and CSRZ signals. The intensity eye diagrams instead are shown in Figure 6.4.

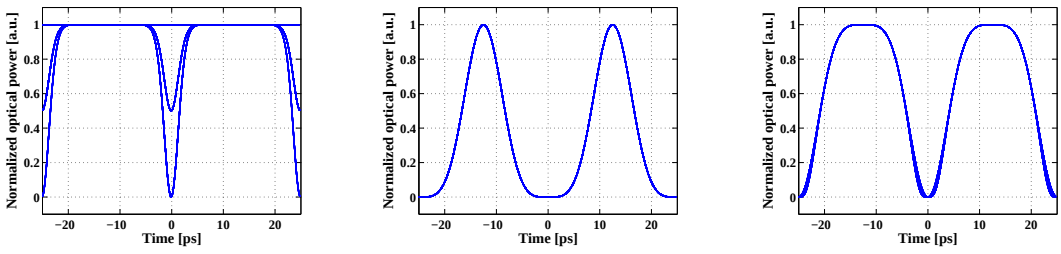

(a) (b) (c)

Figure 6.4: Intensity eye diagrams for 40 Gbaud NRZ (a), RZ 33% (b) and CSRZ (c) QPSK signals.

The transmission of all the three MFs is simulated to evaluate the impact of the MF

on the regeneration performances. RZ formats are indeed used in optical communication systems. NRZ pulses are carved into RZ formats in order to avoid the transition dependent power variations as in the intensity eye diagram of Figure 6.4(a) for $t = 0$.

One critical aspect still needs to be addressed, the choice of the electrical signal driving the modulators. This is discussed in the next Subsection.

6.1.2 Pseudo Random Sequences

In order to reliably evaluate the performances of a communication system, one of the most important aspects is the choice of the transmitted data. To avoid bias in the results, a pseudo-random sequence is required. These sequences are characterized by an autocorrelation given by :

$$\rho(0) = 1 \qquad \rho(i) = -1/n \qquad \text{for } 1 \leq i \leq n-1 \tag{6.2}$$

where n is the sequence length. For a high enough value of n, the sequences can be considered almost random and thus mimic the behavior of digital signals commonly transmitted.
For two-level MFs as OOK and BPSK, binary pseudo random sequence (PRBS) have been extensively studied. Due to their easy generation, the most used kind of PRBS is known as Shift-register sequences. The basis to construct a shift-register sequence of length $n = 2^m - 1$ is a binary primitive polynomial of degree m which specifies the feedback shift-register used as generator. An example is given in Figure 6.5 generating a PRBS characterized by a periodicity of 15 symbols. For a list of binary primitive polynomials refer to [49].

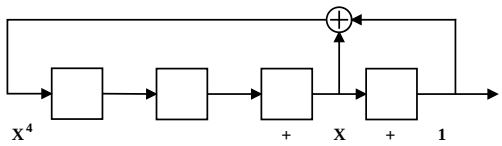

Figure 6.5: Example of feedback shift-register corresponding to $x^4 + x + 1$ [49].

In our simulations however we are propagating a four-level MFs. The easiest choice would indeed be to modulate the signal driving the MZMs with two PRBS sequences of the same length, uncorrelated by a time delay. Regardless of the time delay however,

the two sequences are not totally uncorrelated and (6.2) can only be approached [50].

For our simulations thus we move one step further introducing quaternary pseudo random sequence (PRQS), i.e. the direct extension of PRBS into a quaternary alphabet. Also for these sequences a feedback shift-register generation scheme can be used. The generating polynomial in this case needs to have coefficients defined on a quaternary alphabet and to be primitive over $GF(4)$, the Galois field of dimension four.
A list of primitive polynomials up to order m=10 ($4^{10} - 1$ symbols) is reported in Table 6.1.

m	Polynomial
2	$x^2 + x + 2$
3	$x^3 + x^2 + x + 2$
4	$x^4 + x^2 + 2x + 3$
5	$x^5 + x + 2$
6	$x^6 + x^2 + x + 2$
7	$x^7 + x^2 + 2x + 3$
8	$x^8 + x^3 + x + 2$
9	$x^9 + x^2 + x + 2$
10	$x^{10} + x^3 + 2x^2 + 2x + x$

Table 6.1: Primitive polynomials in $GF(4)$ [49].

The operations of addition (+) and multiplication (×) over $GF(4)$ are then defined in Table 6.2.
In our system a PRQS sequence of 1023 symbols (m = 5) is generated. Then each quaternary symbol is mapped into a pair of bits using a gray-encoding and the two resulting binary sequences (I_k, Q_k) are used to drive the two MZMs (Figure 6.2). Before feeding them to the modulators however, the sequences are up-sampled to 1024 samples per symbol and a Gaussian low-pass filter (LPF) is used to give a rise time of 25% of the bit slot to the square waves.
Finally, we want to stress that no differential encoding is used at the transmitter. As dis-

+	0	1	2	3
0	0	1	2	3
1	1	0	3	2
2	2	3	0	1
3	3	2	1	0

(a)

×	0	1	2	3
0	0	0	0	0
1	0	1	2	3
2	0	2	3	1
3	0	3	1	2

(b)

Table 6.2: Addition (a) and multiplication (b) in $GF(4)$ [51]

.

cussed in [50], the use of a differentially-encoded PRQS introduces correlation between the symbols and thus the autocorrelation property of (6.2) does not stand anymore. To properly evaluate the effects of dispersion and nonlinearities in the regenerators the use of PRQS sequences without any encoding is required.
The main drawback of this choice is the higher complexity at the receiver as discussed in the following Subsections.

6.1.3 Noise Addition

In a real optical communication system, phase noise is introduced by Kerr nonlinearities (Section 3.1). In our simulated system phase noise is instead added through a PM driven by white Gaussian noise with frequencies up to 20 GHz. This choice allows to have a better control over the statistical property of the added noise, in particular its std. The std of the input signal phase (σ_i) is the parameter used in this study to evaluate the overall performances of the regenerators. Both the std of the output signal phase (σ_o) and the BER are calculated as function of σ_i.
In short, the phase noise is inserted through:

$$s'(t) = s(t) \cdot e^{-iw(t)}\,, \tag{6.3}$$

where $s(t)$ is the noise-free signal and $w(t)$ is the white Gaussian noise with zero-mean and std σ_i.

The noise bandwidth (20 GHz) is chosen to be consistent with the results of [11] where noise with a 8 GHz bandwidth modulates 10 Gbaud signals. The influence on the noise statistics has been briefly analyzed in [40] and its scope goes beyond the purpose of

this study. Nevertheless it is indeed a topic worth future studies.

Other than phase noise, also amplitude noise is considered in some simulations. Complex white Gaussian noise is added to the phase noisy signal according to the desired OSNR defined over the reference bandwidth of 12.5 GHz (0.1 nm at 1550 nm) commonly used in literature.

The same method is also used to add noise before the receiver in order to calculate the BER as function of the OSNR.

6.1.4 Signal Phase and Power Analysis

At the output of the regenerator the output signal phase std (σ_o) is defined as [52]:

$$\sigma_o = \max_i \{ \sigma_{o,i} \}, \tag{6.4}$$

where $i = \{\pi/4, 3\pi/4, 5\pi/4, 7\pi/4\}$ refers to one of the four states of the QPSK signal (Figure 6.3(a)).
Our algorithm calculates the std first sampling the optical signal at the center of the symbol slot. Then the samples are split into four groups according to their original (noise-free) value and the phase std $\sigma_{o,i}$ is calculated for each group. Finally (6.4) is used.

Another way of calculating the std would be to sample the fourth power of the signal, thus collapsing the four states into one, calculate the std over all the samples and divide by four to derive σ_o.
This latter method provides a more accurate estimation since the std is calculated over four times the number of samples of the former method.
Unfortunately however this second method is less reliable due to the way in which MATLAB® treats the phase of a signal. A value of the phase in a left neighborhood of π is considered positive while values in the right neighborhood of π are treated as negative. Such discontinuity leads to wrong estimations of the std and unwrapping the phase does not solve the issue.
The same phase discontinuity issue rises also when the method of (6.4) is used. The phase variations of a single state are however lower than the ones for the signal fourth power, when the discontinuity presents itself in the former scenario a constant phase rotation allows to calculate the correct std.

The comparison of the two methods for cases where no discontinuities were highlighted showed negligible variations between the two stds, the method of (6.4) is therefore used throughout our study.

Finally, when comparing the phase and power stds of input and output of the regenerator, the input signal is first propagated through the same filters used in the regenerator. This approach permits a meaningful comparison removing the improvement due to the noise suppression induced by the filters.

6.1.5 Receiver and BER Analysis

In order to evaluate the BER performances with and without regenerator the optical signals with a balanced receiver. The scheme for the balanced receiver is shown in Figure 6.6.

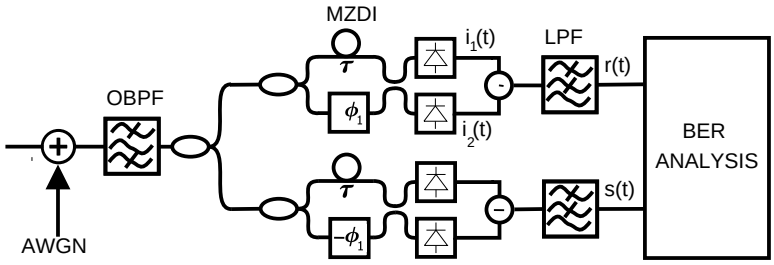

Figure 6.6: QPSK signal balanced receiver scheme as proposed in [3]. ϕ_1 equals to $\pi/4$ for NRZ and RZ 33% signals and $5\pi/4$ for CSRZ signals.

First of all, in order to calculate the BER as function of the OSNR, additive white Gaussian noise (AWGN) is added to the signal. Then the out-of-band noise is removed through a 1st-order Gaussian BPF with a FWHM bandwidth of $2.2 \cdot$ baudrate [53] and the signal is injected into the QPSK balanced receiver. The receiver consists of two Mach-Zehnder delay interferometer (MZDI) with a unitary delay of τ = 1/baudrate set to provide the phase to amplitude conversion according to the differential encoding. The two MZDIs are characterized by an opposite phase shift between their two arms in order to detect the two different components of the signal, in-phase and in-quadrature. Note that the phase shift is $\pi/4$ for NRZ and RZ 33% signals and $5\pi/4$ for CSRZ signals. The additional π shift for the CSRZ format takes into account the extra π-phase shift between neighboring symbols proper of this MF.
Each MZDI is then followed by a balanced photo diode (PD) where the fields at both

ports are detected and the photocurrents ($i_1(t)$, $i_2(t)$) subtracted to generate the output signal. The output signals of both the two detectors, $r(t)$ and $s(t)$, are then filtered with a 3rd-order Bessel LPF with a FWHM bandwidth of 0.7·baudrate [53], sampled at the center of the symbol slot and detected with a threshold of I_{th} =0 A. The PDs have been assumed ideal, so with a unitary responsivity and no noise added.

The pairs of samples (r_k , s_k) represent the de-coded symbols for a differentially encoded QPSK signal. The main drawback of not transmitting a differentially encoded PRQS is caused by this characteristic of the balanced QPSK receiver.
The BER measurements are performed through error counting with a direct Monte Carlo method. The errors are counted comparing the received signal with the signal at the transmitter. Due to the receiver choice, however, the received signal is decoded even though it was not previously encoded. The outputs of the receiver (r_k, s_k) need then to be differentially encoded as [48]:

$$I'_k = \overline{(r_k \oplus s_k)}(r_k \oplus I'_{k-1}) \oplus (r_k \oplus s_k)(s_k \oplus Q'_{k-1}) \,, \tag{6.5a}$$

$$Q'_k = \overline{(r_k \oplus s_k)}(s_k \oplus Q'_{k-1}) \oplus (r_k \oplus s_k)(r_k \oplus I'_{k-1}) \,, \tag{6.5b}$$

with $\oplus$ denoting the binary addition.
The encoded sequences I'_k and Q'_k can thus be compared with the inputs I_k and Q_k calculating the BER.

The receiver has been validated through comparison with trends reported in [53]. In Figure 6.7(a) the difference between our simulations and the results of [53] is below 1 dB for all the MFs showing a good agreement on the overall trends.
The gap between the curves is most likely due to the lack of a careful optimization of the receiver. We simply sample in the middle of the symbol slot and detect with a threshold of 0 A. The reason behind this sub-optimum choice is simply related to computational issues. The BER simulations are already quite demanding with a fixed threshold and sampling time, a sweep of such parameters to optimize the BER would have resulted in a too long computational time.
Nevertheless, we are interested in comparing the performances with and without the regenerator with respect to the back-to-back (BtB) trends illustrated in Figure 6.7(b). Reaching the lowest BER possible is therefore not critical for our analysis.

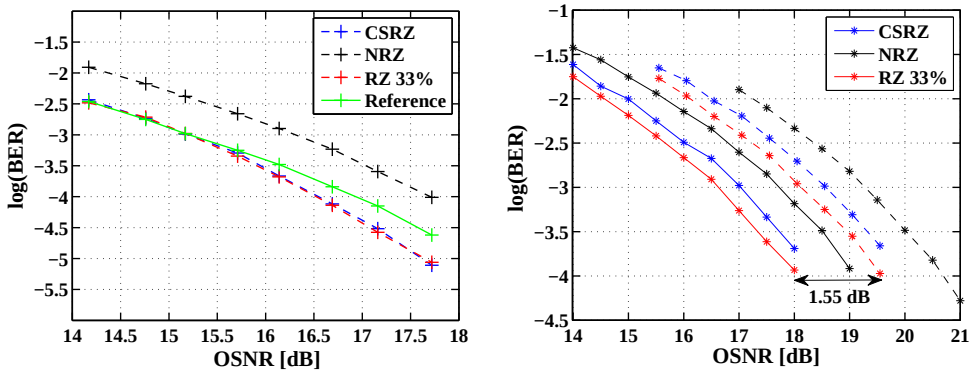

(a) (b)

Figure 6.7: BER as a function of the OSNR at the input of the receiver. Comparison (a)between our BtB simulations for 10 Gbaud NRZ-QPSK, RZ 33%-QPSK and CSRZ-QPSK, and the results of [53]. Performances (b) at 28 (continuous) and 40 (dashed) Gbaud used as reference to calculate power penalty.

Finally the baudrate separation of the BtB curves is 1.55 dB, consistent with the theoretical shift given by the ratio $10 \cdot \log(40/28) = 1.549$ [54].

6.2 DP Non-Degenerate FOPA Regenerator

In this section we analyze the performances of the DP FOPA regenerator proposed in [11] and analyzed in Chapter 4. The analysis is carried on as follows. In the first scenario only phase noise is added to the signal and the regenerator capabilities are defined through the reduction in phase std of the regenerator output. Next, a more general case is investigated adding both phase and amplitude noise to the input signal. The phase std reduction is then calculated for various OSNR levels. Finally the power penalty (PP) difference between the cases with and without regenerator is analyzed and the required OSNRs (R-OSNRs) for the two configurations are compared with the BtB noise-free transmission. In this latter set of simulations only phase noise is added to the modulated signal.

6.2.1 Regeneration for Signals with Phase Noise

The simulations are carried on using the model described in Section 6.1 with no amplitude noise added to the signal. Only the phase is modulated by Gaussian noise

and the input signal phase std (σ_i) is swept from 2 to 20°. According to [1, (6.28)], a phase std of 20° would correspond to the propagation of a 5 mW signal into 24 loops of 200 km of standard single mode fiber (SSMF) characterized by $\alpha = 0.2$ dB/km and γ= 1.3 $W^{-1}{\cdot}km^{-1}$ and with 18 dB of OSNR. This represents a quite extreme case since it involves the propagation through an almost transatlantic distance.

We define the phase std improvement $\Delta\sigma$ as:

$$\Delta\sigma = \frac{\sigma_i - \sigma_o}{\sigma_i}, \tag{6.6}$$

when $\sigma_0 < \sigma_1$ then the improvement is positive and the phase noise is reduced.
Figure 6.8 shows the regenerator improvement as function of σ_i.

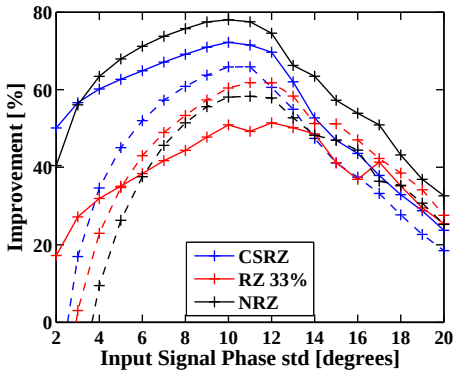

Figure 6.8: Improvement $\Delta\sigma$ as function of the input signal phase std σ_i for three MFs and two baudrates: 28 Gbaud (continuous) and 40 Gbaud (dashed).

Regardless of baudrate and MF, the improvement curves show an increasing trend, reach a maximum around $\sigma_i \approx 10°$ and decrease for higher values of σ_i.
The behavior shown is in line with what was expected. When σ_i is quite small, the regenerator is not expected to provide a large improvement. The squeezing indeed takes place but since the amount of phase noise is already low, the ratio σ_o/σ_i cannot be significantly small. As σ_i increases, so does the spreading of the phase values. As long as the variations are within the flat-zone of the phase response (Figure 4.5) the increase in σ_i is steeper than for σ_o with correspondingly increase of $\Delta\sigma$. When the range of variations grows closer to the step-transitions in the phase response however, for some points the phase noise is increased as is σ_o. The improvement thus starts decreasing.

Comparing the improvement for the two baudrates we notice a worsening of the performances going from 28 to 40 Gbaud when NRZ and CSRZ formats are used. For 40 Gbaud signals, the low values of σ_i are actually increased at the regenerator output corresponding to a negative improvement. The baudrate dependence, shown also in Figure 4.6, may be related to the signal distortion introduced by the set of filters used to select the different frequency components at the output of the first stage (see Chapter 4). Both the signal and the idler are selected through a filter and thus the total effect potentially increases. The distortion is indeed more detrimental increasing the baudrate as the spectral width of both signal and idler is increased.

In our study the bandwidth of the filters has been set to a constant value. A way to investigate the dependence of the improvement on the filter bandwidth would be to scale the filter bandwidth to the signal baudrate in order to make the filtering effects comparable. This has not been done in order to simulate more realistically an optical communication system where the filter bandwidth is fixed.

The above considerations however, do not apply for RZ 33% signals. This MF shows slightly better performances when the baudrate is actually increased.

Finally, we can compare trends for the three MFs at the same baudrate. For a low amount of phase noise the performances are quite dependent on the chosen format. As σ_i increases beyond 10°, the improvement decreases with different steepness and the gap between the curves is shrank.
When the input phase noise is strongly increased, the signal samples are spread beyond the flat steps of the phase characteristic regardless of the MF and thus the improvements tend to similar values.

6.2.2 Regeneration for Signals with Phase and Amplitude Noise

Signals propagating through optical links are not affected only by phase noise, amplitude noise plays an important role as well.
To analyze the regenerator potential in a more realistic scenario, the phase std improvement is here evaluated for different values of OSNR spanning from 35 to 60 dB. The OSNR is calculated only on the amplitude noise added after the noise-driven PM. Furthermore, as the noise added is complex Gaussian noise, it indeed increases the total

amount of phase noise. The input phase std is therefore calculated after the amplitude noise addition.

Figure 6.9 reports the improvement curves as function of σ_i for the three MFs and the different values of OSNR.

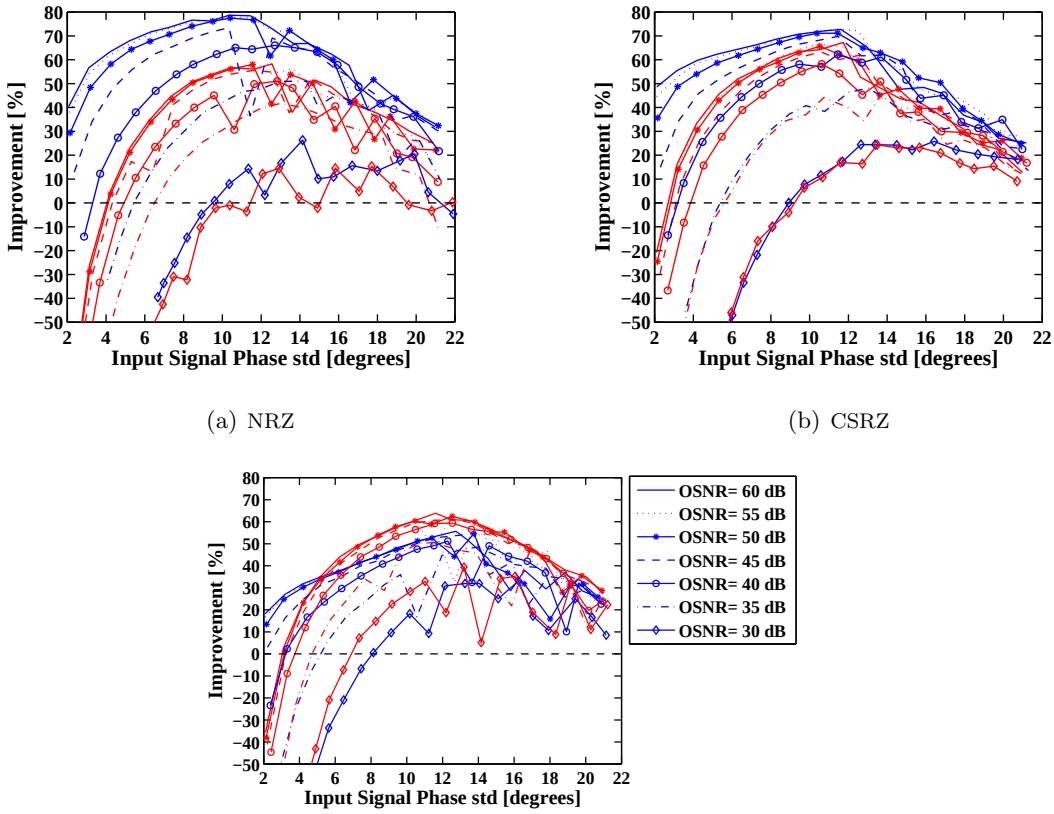

(a) NRZ

(b) CSRZ

(c) RZ 33%

Figure 6.9: Improvement $\Delta\sigma$ as function of σ_i for various values of the OSNR: (a) NRZ, (b) CSRZ and (c) RZ 33% for a baudrate of 28 Gbaud (blue) and 40 Gbaud (red).

The improvement curves show the same overall trend of Figure 6.8 but with a more irregular profile. Despite each plotted point being the results of an average over 30 simulations, the statistic is not precisely calculated. Nevertheless some general considerations can be drawn.

First of all, as the OSNR is decreased, the improvement curve is down-shifted reaching

negative values already for an OSNR of 40 dB when the baudrate is 28 Gbaud.[2] This effect is less obvious than it appears at first sight. The increased σ_i due to the amplitude noise added cannot be hold responsible as the definition of $\Delta\sigma$ already takes such effect into account. In general the increase in σ_i causes only the right-shift of the curves.
However, as underlined more than once throughout this study, the amplitude noise impairment comes from its conversion into phase noise through Kerr nonlinearities. The regenerator relies on such nonlinearities so the squeezing effect is contrasted by the amplitude-to-phase noise conversion resulting in a lower $\Delta\sigma$.

Furthermore, concerning the baudrate dependence, the performance gap between the two baudrates decreases with the OSNR. Such behavior can be again related to the filters used in the scheme. Increasing the baudrate the spectral width of the signal is increased and so are the distortion effects. At the same time however a narrower filter[3] provides a higher noise suppression and in turn a lower amount of noise amplitude-to-phase converted. In order to verify this explanation the performances of the regenerator could be checked suppressing the pump at the input. The regeneration property would thus be disabled and only the effects of the filters on the noise conversion would be highlighted.

In Figure 6.8 we have remarked that RZ 33% signals are impacted differently by the baudrate. When the OSNR is decreased however, also these signals start following the same trend as the other MFs.

Finally, to avoid the confusion resulting from the trends irregularity, we can focus on analyzing only the influence of the OSNR on the maximum improvement $\Delta\sigma_{max}$ and its position (in σ_i). The results are illustrated in Figure 6.10.
For low values of the OSNR, the trends are not parallel and actually RZ 33% signals show a better phase noise reduction compared with the other two MFs regardless of the baudrate. In general for RZ 33% signals the overall performance are less dependent on

[2] At 40 Gbaud the improvement for low σ_i is already negative even without amplitude noise so it keeps showing negative values when the OSNR is decreased.

[3] More precisely it is actually the signal that becomes broader increasing the baudrate, the filter bandwidth is unchanged. "Narrower" needs thus to be read in a relative sense, compared with the signal.

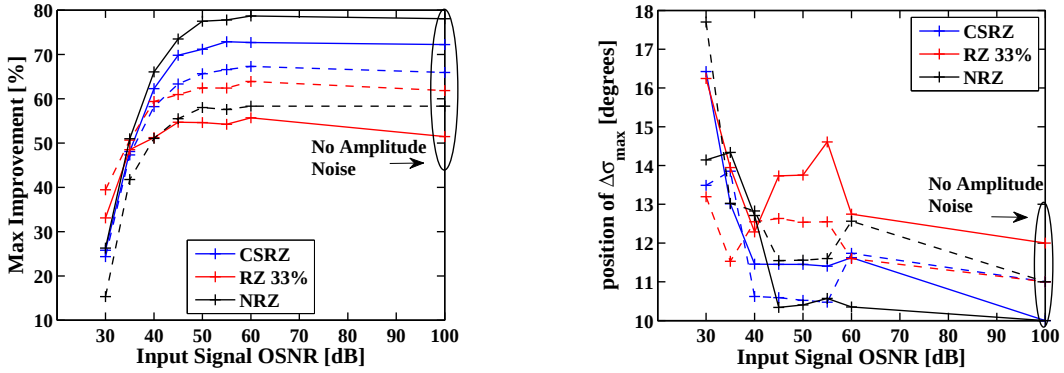

(a) (b)

Figure 6.10: $\Delta\sigma_{max}$ (a) and corresponding value of σ_i (b) as function of the OSNR for a baudrate of 28 Gbaud (continuous) and 40 Gbaud (dashed). The case with no amplitude noise added is treated as OSNR=100 dB.

the OSNR as the range of values assumed by $\Delta\sigma$ is smaller. As a drawback also the max improvement is lower.

Furthermore Figure 6.10(a) shows the saturation of $\Delta\sigma$ towards the amplitude-noise-free[4] values when the OSNR reaches a quite high level (~45 dB) and the distance between the curves becomes consistent with Figure 6.8.

Similar considerations can be drawn for the value of σ_i at which the maximum improvement is achieved. For low OSNRs the maximum is shifted towards higher σ_i values together with the whole curve but it quickly reverts to the amplitude-noise-free value when the OSNR is increased, similarly to $\Delta\sigma_{max}$.

6.2.3 BER Performances

The phase std improvement represents an important indicator in evaluating the potential of the phase regenerator. From a communication system perspective however, the quality of the regeneration needs to be assessed through the BER. In this subsection then we present the results of our BER measurements for various values of σ_i. The

[4]In Figure 6.10(a) this value is marked as OSNR=100 dB.

BER is measured as function of the OSNR at the receiver input for both noisy and regenerated signal.

In order to use a meaningful definition of OSNR only phase noise is added to the signal after the QPSK modulator. The complex AWGN providing the desired OSNR is then summed to the signal only before injecting it into the receiver.

The minimum number of error counted through the direct Monte Carlo simulations is set to 500. This choice guarantees a confidence level above 99% [55].

To characterize the regenerator the figure of merit used is the R-OSNR, defined as the OSNR required to achieve the target BER set to 3.3×10^{-3}. Assuming the use of forward error correction (FEC) with BCH(3860,3824) as outer code and BCH(2040,1930) as inner code, according to G.975.1 clause I.3 [56], the chosen error threshold is equivalent to a BER of 1×10^{-12}.

The drawback of using this coding scheme is the 6.69 % overhead required. The actual baudrates are therefore reduced to 26.25 and 37.5 Gbaud respectively. To avoid confusion however we keep referring to 28 and 40 Gbaud signals.

The BER curves are calculated for the three MFs and two baudrates in three scenarios:

- BtB transmission used as reference (Figure 6.7(b);
- signal with phase noise filtered[5] but not regenerated ("noisy signal");
- signal with phase noise regenerated ("regenerated signal").

First of all we can analyze the minimum input phase std $\bar{\sigma}_i$ giving rise to an error floor above the target BER. The results with and without regeneration are shown in Table 6.3.
Comparing the $\bar{\sigma}_i$ values, a improvement is clearly visible when the regenerator is used. On average $\bar{\sigma}_i$ is increased of more than 4°.

[5] As discussed above, to remove the bias in the analysis due to the presence of filters in the regenerator scheme, the noisy signal goes through the same set of filters as the regenerated one.

	28 Gbaud	40 Gbaud
CSRZ	10°	11°
NRZ	12°	10°
RZ 33%	10°	11°

(a)

	28 Gbaud	40 Gbaud
CSRZ	16°	15°
NRZ	16°	15°
RZ 33%	14°	14°

(b)

Table 6.3: $\bar{\sigma}_i$ values without (a) and with (b) regeneration.

More interesting is the full comparison of the relative power penalty (RPP) defined as the difference between the R-OSNRs without the regenerator and with the regenerator. Negative values of RPP refers to a lower R-OSNR for the regenerated configuration. The calculated RPP as function of σ_i is shown in Figure 6.11 for the usual three MFs and two baudrates.

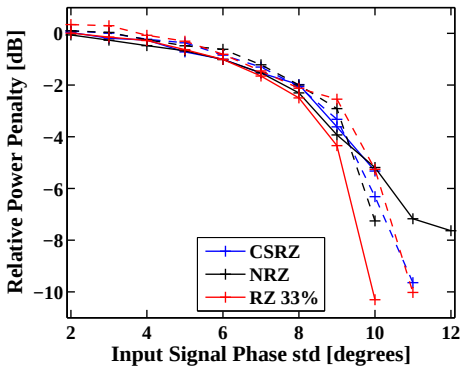

Figure 6.11: RPP as function of the input signal phase std σ_i for the three MF and a baudrate of 28 Gbaud (continuous) and 40 Gbaud (dashed).

For low values of σ_i the RPP is positive but always below 0.35 dB. As the phase noise increases though, the improvement derived by the use of the regenerator becomes evident. The RPP decreases with increasing σ_i reaching values as low as -10 dB.
In Figure 6.11 the RPP is shown only for the phase std values where the R-OSNR is well defined for both noisy and regenerated signal.

As discussed above, there is a range of values for σ_i where the target BER can be reached only with the use of the regenerator. Eventually however, as the constellation

spreads further, an error floor starts rising also for the regenerated signal and the BER of 3.3×10^{-3} cannot be reached anymore.

Finally a comparison with the BtB R-OSNR is presented in Figure 6.12. The PP between BtB transmission and both noisy and regenerated signals are illustrated as function of σ_i.

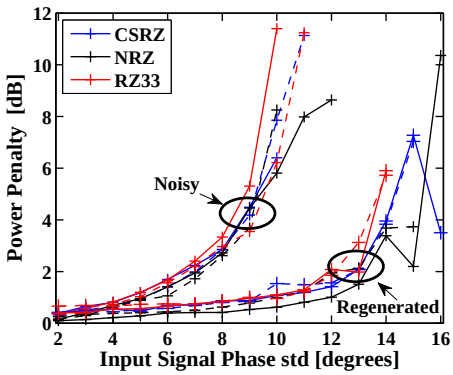

Figure 6.12: PP as function of the input signal phase std σ_i for three MFs and a baudrate of 28 Gbaud (continuous) and 40 Gbaud (dashed). Both the PP of noisy and regenerated signals are shown as marked in the plot.

The analysis of the PP reinforces our conclusions. In general the curves obtained with the regeneration are shifted to higher values of σ_i compared with the case without regenerator. Furthermore, while the PP for the noisy signal shows a monotonic increase, when the regenerator is used the trend is kept quite flat and starts increasing significantly only after the noisy signals have already hit the error floor. The increase is however quite steep so it is desirable to keep the input phase noise below a chosen threshold. Figure 6.12 hints that a suitable choice would be to allow a phase noise accumulation up to $\sigma_i \approx 12°$ to keep the PP below 2 dB, other than obtaining MF and baudrate transparent performances. No strong impact of the baudrate or the MF can indeed be seen in the $2° \div 12°$ range. The curves start to grow independently only after $\sigma_i \approx 13° - 14°$. For such high phase noise however, the performances become considerably dependent on the single phase noise realization. A thorough investigation, averaging the results of more than the five noise realizations here considered is needed to obtain a more precise statistic. Time and computational constraints did not allow such study to be done.

Finally the baudrate transparency shown by the BER curves seems in contrast with the analysis of the phase std. This latter parameter however, does not provide a complete description since it neglects the amplitude noise introduced by the phase squeezing. The results of Figure 6.8 indeed convey a good insight into the improvements provided by the regenerator. Nonetheless to precisely evaluate the performances a figure of merit like the BER (Figures 6.11 and 6.12) is required.

6.3 DP Degenerate FOPA Regenerator

In this section we analyze the performances of the FOPA-based MZI regenerator proposed in Chapter 5. The analysis follows the same structure of Section 6.2: first we evaluate the improvement in the phase std both for the scenario with only phase noise and when also amplitude noise is added; then the BER is discussed. Finally the two-stage regeneration introduced in Section 5.4 is investigated.

6.3.1 Regeneration for Signals with Phase Noise

The simulations are carried on as in the previous Section but replacing the regenerator of [11] with our proposed scheme described in Chapter 5.
Figure 6.8 shows the influence of σ_i on the phase std improvement $\Delta\sigma$ defined in (6.6). The values for the improvement have been obtained averaging the results of 100 tests for each points in the Figure.

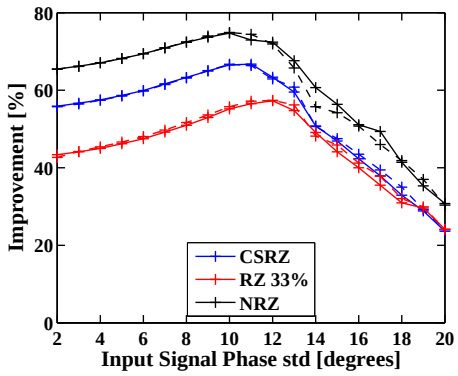

Figure 6.13: Improvement $\Delta\sigma$ as function of the phase std of the input signal σ_i for three MFs and a baudrate of 28 Gbaud (continuous) and 40 Gbaud (dashed).

From the trends shown we can derive some preliminary conclusions on the effectiveness of the regenerator.

As for the other scheme the performances improve with the increase of σ_i till they reach a maximum value around $10° \div 11°$ and start to decrease.

Comparing these trends with the DP non-degenerate FOPA however, in our regenerator the improvement is above 20% for all values of σ_i regardless of MF or baudrate.
A quite high improvement is shown even for low values of σ_i, improvement significantly higher than for the previously analyzed scheme. The performances of the former scheme rely on a total fiber length of 800 m, this second regenerator instead uses 177 m of HNLF so the phase noise added inside the regenerator through Kerr nonlinearities is definitely less. This aspect is mainly significant for low values of σ_i, when the amount of phase noise at the input increases it becomes negligible.

Furthermore, the simulations illustrate the baudrate transparent behavior of the proposed scheme. For each MF the results for the two baudrates are almost superimposed, unlike the non-degenerate scheme previously discussed. Kerr nonlinearities take place on a time scale of less than 10 fs for optical fibers [57] so much faster than the time variation of the propagated pulses where each symbol occupies a time windows of 37.5 and 25 ps respectively for 28 and 40 Gbaud. Furthermore the effects of the filter are less pronounced in this system thanks to the broader frequency spacing.

Finally a clear comparison of the three MFs can be made. For low amounts of phase noise we can notice a gap between the curves around 10%, going from the best performances of NRZ to the worst of RZ 33%. As for the previous regenerator then, as σ_i increases beyond 10° degrees the gap between the curves is shrank. The steepness of the decrease is higher for NRZ and CSRZ signals then for RZ 33% signals resulting at the end in the complete overlap of the curves for the last two.
The initial gap can be relate to the different resilience of the MFs towards nonlinearities which in turn decides the performances of the regenerator. For high values of σ_i however the constellation spreading collapses the performances regardless of the MF as discussed previously.

6.3.2 Regeneration for Signals with Phase and Amplitude Noise

Figure 6.14 reports the improvement curves as function of σ_i for the three MFs and different values of OSNR.

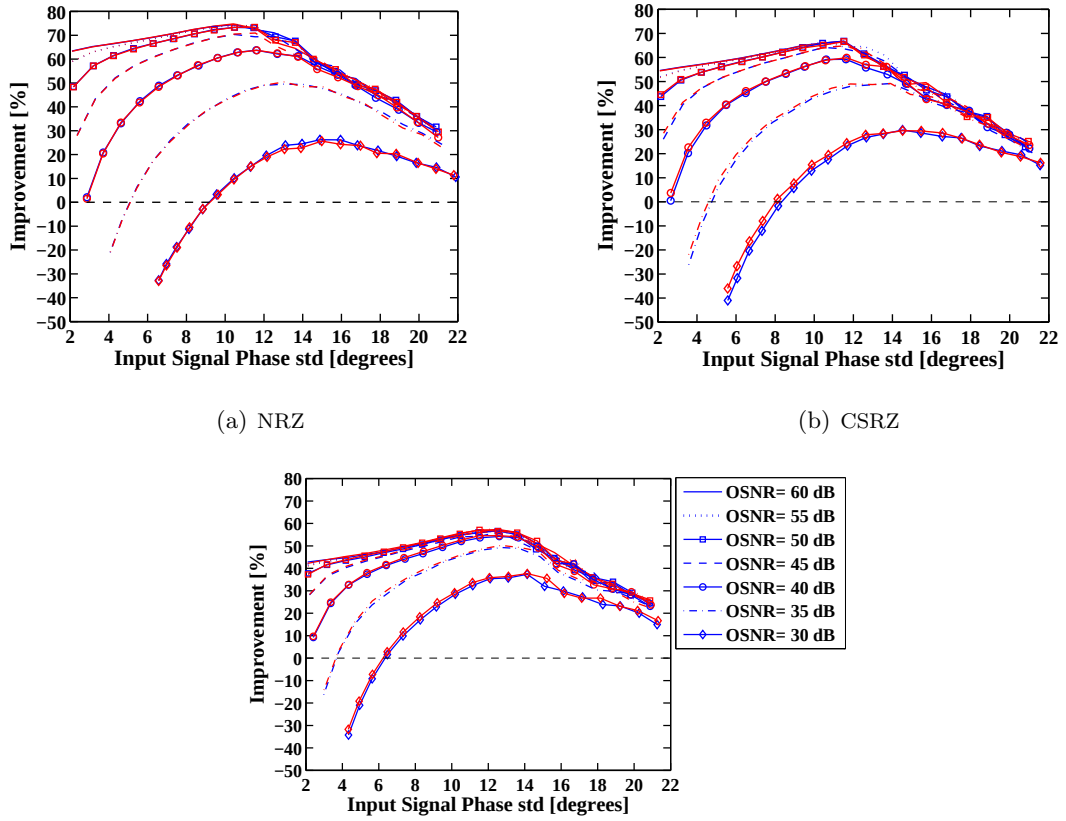

(a) NRZ

(b) CSRZ

(c) RZ 33%

Figure 6.14: Improvement $\Delta\sigma$ as function of σ_i for various values of the OSNR: (a) NRZ, (b) CSRZ and (c) RZ 33% for a baudrate of 28 Gbaud (blue) and 40 Gbaud (red).

As we can see the trends show the same characteristics of the amplitude-noise-free analysis. All the improvement curves are concave and there is no substantial difference between the two baudrates.

Furthermore, like in Figure 6.9, for increasing OSNR the curves are both down and right shifted due to the increased σ_i and the amplitude-to-phase noise conversion. This latter effect is particularly detrimental for low values of the input phase std. The curves undergo a stronger down-shift for low σ_i values. The amplitude-to-phase noise

conversion is independent on the initial amount of phase noise, so indeed the amplitude noise has a stronger influence for lower σ_i values. The overall down shift, however, is less significant than for the previously analyzed scheme as was expected due to the shorter fiber spans and thus the lower Kerr effects.

Finally, concerning the comparison between the performances of the three MFs, some more considerations are required.
The right shift of the improvement curve is highly MF-dependent. The displacement is stronger for NRZ and CSRZ signals while RZ 33% signals are less affected. At the same time, also the decrease in the improvement follows a similar trend.

In order to provide a more rigorous comparison, Figure 6.15 shows the impact of the OSNR on the maximum improvement $\Delta\sigma_{max}$ and the value of σ_i at which such improvement is achieved.

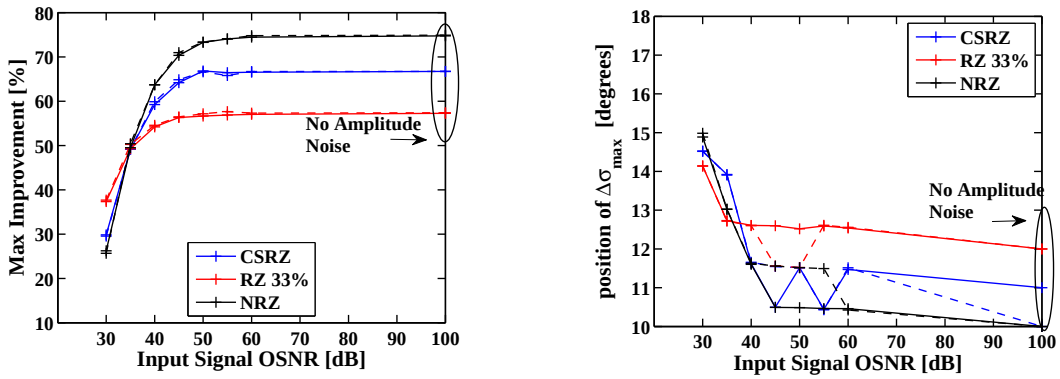

(a) NRZ

(b) CSRZ

Figure 6.15: $\Delta\sigma_{max}$ (a) and corresponding value of σ_i (b) as function of the OSNR and a baudrate of 28 Gbaud (continuous) and 40 Gbaud (dashed). The case with no amplitude noise added is treated as OSNR=100 dB.

Concerning the maximum $\Delta\sigma$, RZ 33% signals show better performances for low values of the OSNR (Figure 6.15(a)). The performances are then increased lowering the amplitude noise, with a common 50% improvement for all the MFs when OSNR=35 dB. Further reductions in the AWGN power revert $\Delta\sigma$ back to the amplitude-noise-free scenario[6].

[6] In Figure 6.15(a) this value is marked as OSNR=100 dB.

Finally, as the OSNR reaches a value around 50 dB, the influence of the amplitude noise both on the maximum improvement and on the overall trend becomes negligible. In general therefore the behavior reported follows the discussion for the DP non-degenerate FOPA. Unlike the previous scheme however, the trends are not determined by the filter bandwidth as it is hinted by the lack of baudrate impact. For this system the MF dependence may still be related to the tolerance of each single format towards non-linearities. As RZ is more resilient, the regeneration process is less effective. At the same time however also the amplitude-to-phase noise conversions is less efficient. This explains why when the noise conversion is significant, i.e. for low OSNR, the overall performances of RZ signals are higher than NRZ signals. Also this hypothesis can be evaluated analyzing the propagation in the regenerator with no input pumps.

As a last remark Figure 6.15(b) confirms the right-shifting of the curve described analyzing Figure 6.14.

6.3.3 BER Performances

The evaluation of the BER performances of the DP degenerate FOPA follows the same structure presented for the non-degenerate case in Section 6.2.
First of all we can analyze the minimum σ_i ($\bar{\sigma}_i$) giving rise to an error floor above the target BER. The values for the different MFs and baudrates are reported in Table 6.4.

	28 Gbaud	40 Gbaud
CSRZ	11°	11°
NRZ	11°	11°
RZ 33%	10°	10°

(a)

	28 Gbaud	40 Gbaud
CSRZ	15°	14°
NRZ	15°	13°
RZ 33%	16°	15°

(b)

Table 6.4: Minimum σ_i value giving rise to an error floor above a BER of 3.3×10^{-3} without (a) and with (b) regeneration.

First of all note that the slight differences between Table 6.3(a) and 6.4(a) are due to both the different filters in the two regenerator and the different noise realizations. Nonetheless the values are comparable.

Concerning the increase of $\bar{\sigma}_i$ due to the regenerator, on average almost 4° of improvement can be achieved, similarly to the previous scheme.

Figure 6.16 shows the RPP curves.

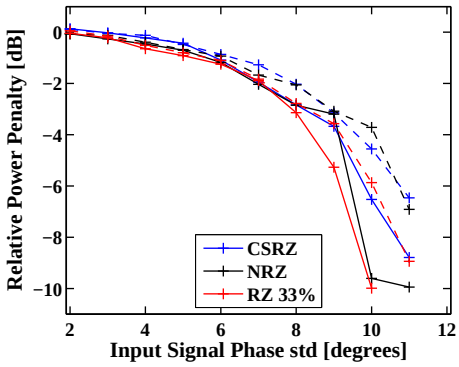

Figure 6.16: RPP as function of the input signal phase std σ_i for three MFs and a baudrate of 28 Gbaud (continuous) and 40 Gbaud (dashed).

The trends reported are generally comparable with the results of Figure 6.11. For low σ_i values however, the RPP is lower for this scheme, with a maximum below 0.13 dB. This result is in-line with the high $\Delta\sigma$ shown in Figure 6.13 even for low σ_i values.

Furthermore, no significant impact from MF and baudrate can be seen from the curves. Signals at a lower baudrate seem to provide a higher OSNR improvement for $\sigma_i > 10°$ but the gaps shown between the curves are mostly due to the more irregular trends. As already mentioned for the previous scheme, a more thorough average of the BER results is required to define precisely the behavior when $\sigma_i \approx \bar{\sigma}_i$.

Note that the slightly different values of $\bar{\sigma}_i$ for the two baudrates Table 6.4(b)) may be influenced by the power penalty due to the increased baudrate as shown also for BtB transmissions (Figure 6.7(b)). Such factor is removed discussing differences as RPP and PP.

Finally, the overall PP for both noisy and regenerated signal is illustrated in Figure 6.17.

Like RPP, also the PP shows trends similar to Figure 6.12. The only significant difference is a flatter PP curve using the degenerate regenerator scheme. Nevertheless, when σ_i increases to ~ 13°, an abrupt increase of the PP can be noticed, with the PP reaching the same levels as the DP non-degenerate configuration.

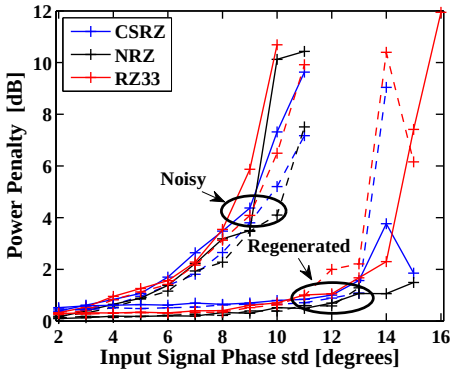

Figure 6.17: PP as function of the input signal phase std σ_i for the three MFs and a baudrate of 28 Gbaud (continuous) and 40 Gbaud (dashed). Both the PP of the noisy and regenerated case are shown as marked in the plot.

6.3.4 Two-stage Regeneration for Signals with Phase Noise

In Section 5.4 we have introduced the possibility to use an amplitude regenerator as a second stage after the phase regeneration. In this Subsection thus we briefly evaluate the performances of this system to confirm the trade-off between phase and amplitude noise reduction illustrated through the constellation diagrams of Figure 5.21.

A NRZ-QPSK signal characterized by its σ_i is propagated through the two stages regenerator of Figure 5.19 and both output power std and phase std improvement are analyzed.
The results as function of σ_i are shown in Figure 6.18 where the case without the second stage is compared to three different scenarios for the amplitude regenerator: P_s is set respectively to 30, 40 and 50 mW as discussed in Section 5.4.

Note however that in Figures 6.18(a) and 6.18(b) we are comparing two different quantities. We are not discussing power std improvements because the signal at the input of the phase regenerator has negligible power fluctuations, with a std as low as 10^{-12} W. It is therefore meaningless to define a ratio with such a low reference value.

Figure 6.18(a) shows indeed a decrease in the output power std with the use of the amplitude regenerator.
Furthermore, the closer P_s to the peak of the saturation curve ($\sim$ 50 mW as in Fig-

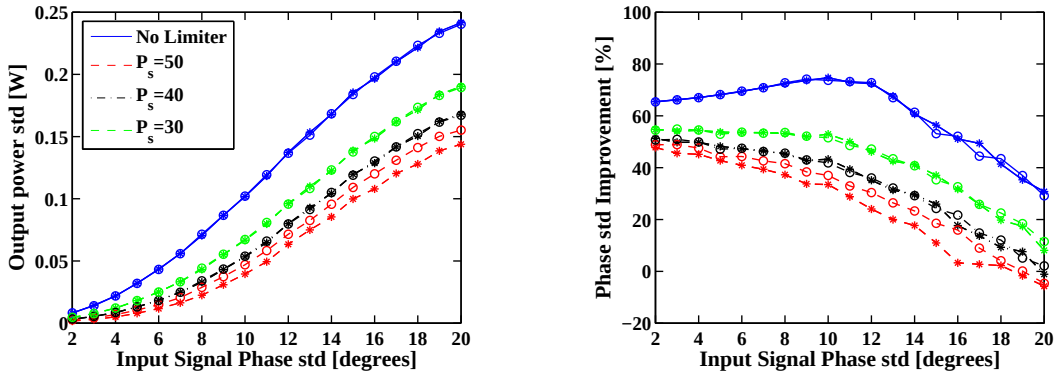

(a) (b)

Figure 6.18: Output power std (a) and phase std improvement (b) as function of the input phase std: without amplitude regenerator (blue) and with 30 (green) 40 (black) and 50 (red) mW of power in input to the amplitude regenerator for a baudrate of 28 ($\circ$) and 40 ($*$) Gbaud.

ure 3.5) the lower the output power std. Finally the two-stage regenerator results almost baudrate transparent. Only a small gap between the two curves is shown when P_s = 50 mW. Since the phase regenerator has been proven baudrate independent, this gap is indeed caused by the second stage. Further studies however are needed to evaluate the reasons behind this behavior, analyzing more in details the performances of the amplitude regenerator alone.

Figure 6.18(b) then illustrates the drawback introduced in Section 5.4 between amplitude squeezing and phase un-squeezing. When increasing the power P_s, the power std is lowered as is the phase std improvement. A trade-off is required. To assess the optimal configuration however, a more rigorous study using parameters as the BER should be carried on.

As a final remark note the same gap discussed for the power std is shown also for the phase std improvement.

6.4 Summary

To conclude our analysis we can summarize the results drawing some conclusions.

First of all through the evaluation of both phase std and BER we have demonstrated the increase in performances given by the use of a regenerator before the receiver.

Then, the comparison of the two presented schemes based on the phase std highlights a baudrate transparency of the degenerate FOPA which is not shared by the non-degenerate scheme.

This behavior is however not directly reflected by the BER analysis. According to the error rate both methods performs similarly for 28 and 40 Gbaud.
This discrepancy may be looked into investigating the impact of both phase squeezing and amplitude un-squeezing at the receiver.

Finally the both phase std and RPP results show slightly worse performances for RZ 33%.

Chapter 7

Parametric Amplification with Stimulated Brillouin Scattering

Throughout our study we have neglected the effects of stimulated Brillouin scattering (SBS) in optical fiber in order to lower considerably the computational requirements of our model. Nevertheless Brillouin effects are strongly affecting parametric processes and are thus discussed in this Chapter.

In Section 7.1 we begin giving a theoretical introduction to SBS underlining why it is detrimental for FOPAs and briefly discussing the main solutions proposed to limit its effects. Then, Section 7.2 presents and analyzes our dynamic model to solve the Nonlinear Shcrödinger equation with SBS and Section 7.3 provides a comparison with results presented in literature in order to validate the model. Finally Section 7.4 investigates the effects of Brillouin scattering on parametrical amplification.

7.1 Theory of Stimulated Brillouin Scattering

Electrostriction is the property of dielectric materials, as silica, to become compressed if an electric field is applied.

Qualitatively, when a strong pump travels in an optical fiber, variations in the electrical field generate, through electrostriction, changes in the material density and consequently an acoustic wave. Such acoustic wave modulates the refractive index of the fiber with the creation of a Bragg diffraction gratings that scatters the light beam.

To get a deeper understanding of the process however, the use of quantum mechanics is required. Brillouin scattering consists in the annihilation of a light photon at frequency ω_p with the creation of another light photon at frequency $\omega_{BS} < \omega_p$ and an acoustic phonon. Applying both the energy and the momentum conservation we get a constraint on the Stokes shift ω_B and the acoustic wave number $\mathbf{k_B}$:

$$\omega_B = \omega_p - \omega_{BS} \qquad\qquad \mathbf{k_B} = \mathbf{k_p} - \mathbf{k_{BS}}\,,$$

where the subscript "BS", as "Brillouin scattering", indicates the Stokes wave.[1] Combining those relation we get [57]:

$$\omega_B = 2v_A|\mathbf{k}_p|\sin(\psi/2),$$

where v_A is the velocity of the acoustic wave and ψ is the angle between the pump and the Stokes field as in Figure 7.1(b).

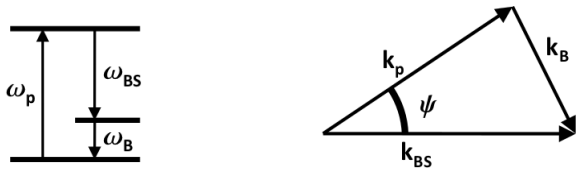

(a) (b)

Figure 7.1: Energy (a) and wave vector (b) diagrams between pump, Stokes field and acoustic wave (not to scale).

In a single-mode fiber only two direction of propagation are allowed: forward and backward. For the former, however, $\psi = 0$ implies $\omega_B = 0$ and consequently no Stokes shift. Our focus is thus on the backward scattered power.

Once the scattered wave at frequency ω_{BS} is generated, it beats with the pump creating a new component at a frequency equals to $\omega_p - \omega_{BS} = \omega_B$. Such component increases the amplitude of the acoustic wave, and therefore the amplitude of the scattered wave itself in a positive feedback loop.

[1] The perhaps more obvious subscript "S" as "Stokes" has not been chosen to avoid confusion with "signal".

The feedback process can be described by the following coupled power equations[2] in steady-state conditions [57]:

$$\frac{dP_p}{dz} = -\frac{g_B}{A_{eff}} P_p P_{BS} - \alpha_p P_p \,, \tag{7.1a}$$

$$\frac{dP_{BS}}{dz} = -\frac{g_B}{A_{eff}} P_p P_{BS} + \alpha_{BS} P_{BS} \,, \tag{7.1b}$$

where P_p and P_{BS} are the pump and Stokes field powers respectively, α_i the losses and $g_B(\omega)$ the Brillouin gain of the dominant acoustic mode [58]. Due to the finite lifetime of the acoustic phonons the ideally constant Brillouin gain becomes frequency dependent. Assuming an exponential decay for the acoustic wave and steady-state conditions, the Brillouin gain shows the Lorentzian profile [57]:

$$g_B(\omega) = \frac{g_B(\Delta\omega_B/2)^2}{(\omega-\omega_B)^2 - (\Delta\omega_B/2)^2} \,. \tag{7.2}$$

For silica fibers, the Brillouin frequency ω_B is around 10 GHz and the Brillouin gain bandwidth $\Delta\omega_B$ of the order of 10÷100 MHz [59]. The latter in particular is directly related to the lifetime of the acoustic phonons [57].

The steady-state approximation used to derive (7.2) stands only for a CW pump with a linewidth $\Delta\omega_P \ll \Delta\omega_B$. When such condition is not fulfilled, the Brillouin gain is considerably reduced and may become negligible when compared against Kerr nonlinearities or even Raman scattering.

For a pump with Lorentzian profile[3], the Brillouin gain peak is reduced by a factor $1 + \Delta\omega_p/\Delta\omega_B$.

When characterizing a fiber span for an optical communication system, the main parameter used to describe the Brillouin effects is the SBST defined as:

$$P_{th} \;=\; \{\, P_p(0) \,|\, P_{BS}(0) = \mu \cdot P_p(0) \,\} \,. \tag{7.3}$$

Concerning parameter μ, different values have been proposed in literature. The most common are $\mu = 1$ [57, 61], $\mu = 0.1$ [62] or $\mu = 0.01$ [58, 63, 64].

A well-known estimate of P_{th} for $\mu = 1$ derived under the undepleted pump approximation, i.e. neglecting the losses of power in the pump due to SBS, is given by [61]:

$$P_{th} \approx 21 \frac{A_{eff}}{g_B L_{eff}} \,, \tag{7.4}$$

[2] Polarization mismatch between pump and Stokes waves is neglected as throughout the whole thesis.

[3] A Lorentzian profile is a reasonable approximation for a signal at the output of a single mode laser [60].

where A_{eff} and L_{eff} are respectively effective area (A.7) and effective length (A.2) of the optical fiber.

In general the SBST defines the maximum amount of power that can be injected into the optical fiber without excessive losses. Standard Ge-doped HNLFs show values for the SBST of the order of 18 dBm [47, 64]. The SBST is thus significantly below the power levels we have discussed throughout this work. Parametric amplification relies on the power flow from a strong pump to a signal. When the pump power is strongly depleted by Brillouin effects, the power transferred to the signal is indeed reduced (see Section 7.4). The most promising solutions proposed to increase the SBST and so keep the backscattered power low are pump phase modulation, fiber doping and multi-segment links.

The first solution relies on phase modulating the pump with signals at radio frequencies in order to broad the pump spectrum and thus lower the Brillouin gain as in (7.2) [13, 65]. This study however focuses on PSA and thus strict requirements are set on the pump phase. In general modulating the pump is avoided when it comes to phase regeneration, so in the following Subsection we discuss only the other two methods.

7.1.1 Optical Fiber Doping

Many optical fibers manufacturers are currently spending quite some effort into designing HNLFs with a high SBST. The technique showing the highest potential consist in doping the fiber core with Aluminum (Al).

The core of optical fibers is usually doped with GeO_2 which has the property of increasing the refractive index of pure silica and thus generate a higher refractive index than in the cladding. From the SBS point of view however, GeO_2 doping is not a suitable choice. The field distribution of optical and acoustic modes in Ge-doped silica is very similar and thus the efficiency of the interaction between optical (ω_p) and acoustic (ω_B) modes is increased.

The proposed approach relies on using other dopants to reduce the overlapping between the two modes. Among the possible dopants for silica, the most interesting is Al_2O_3 which has the property of increasing the optical refractive index while decreasing the

acoustic refractive index [66]. In the Al-doped core, the sound speed is increased compared to the cladding creating an anti-guiding structure that refracts acoustic waves away from the core and into the cladding. The feedback process increasing the backscattered power is thus attenuated.
In [47] it has been shown that the comparison between two HNLFs, one Ge-doped and the other Al-doped, results in a ~10 dB higher SBST for the Al-doping. The main drawback is the high attenuation in Al-doped silica up to 15 dB/km.
Further improvements can be achieved designing a fiber structure with different dopants in different areas of the core [66] or applying a strain to the fiber span [64]. The latter technique provides improvements up to 6 dB (even for Ge-doped HNLF). The main drawback is however the shift of the ZDW. Being parametric amplification strongly dependent on the dispersion profile of the fiber, care should be taken when straining an optical fiber used as FOPA.

7.1.2 Multi-segment Fiber Links

The SBST can be increased with a careful system design of the fiber link. Formula (7.4), even providing only an approximation, shows the dependence of the SBST on the fiber length through L_{eff}. The idea proposed in [67] and experimentally demonstrated in [68] consists in transmitting through a fiber link made of more than one fiber span. The use of more, shorter fibers allows to increase the overall SBST.
As shown in Figure 7.2, the length of every segment of an N section link is tailored in order to have the output power of section $i-1$ equal to the SBST of section i. If such condition is fulfilled for all the N sections, the overall SBST coincides with the threshold of the first segment.
Furthermore, the SBST can be shifted even further using isolators between the fiber spans to avoid the Stokes wave generated in section i to back-propagate in section $i-1$, overlapping and thus amplifying the Stokes wave generated in that section.
The most obvious drawback of such solutions is the increase in losses. Even if splicing losses have been neglected in [68], they cannot be underestimated as the number of section grows. Concerning parametric processes then, using different fiber spans means different fiber parameters and more importantly a different dispersion profile. The results of such effects are far from being straightforward. In Section 7.4 a specific case is analyzed. Parametric gain is numerically calculated in a link composed by two HNLFs with respectively Al and Ge doping.

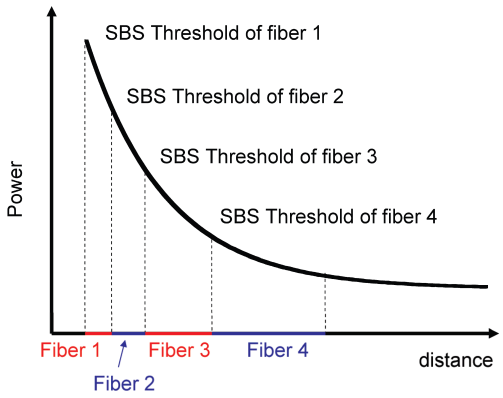

Figure 7.2: Optical power as a function of the distance for an optimized link with the output power of Fiber $i-1$ equals to the SBST of Fiber i [68].

7.2 Dynamic Model for Stimulated Brillouin Scattering

The set of coupled equations in (7.1) has the main limitation of not taking into account the dynamic behavior of the waves: none of the effects giving rise to parametric gain is included. In order to include Kerr nonlinearities and GVD, equations describing the propagation of the fields amplitude are required.

As for all the numerical models used in this study, the starting point is the NLSE. Extra terms to take into account the interaction between the pump and Stokes wave need to be added to (B.5) of Appendix B. Following the approach of [62] we can derive the propagation equation under the assumption of a pump with a dominating carrier component at ω_c and the Stokes wave being a CW signal with only one frequency component at $\omega_{BS} = \omega_c - \omega_B$.

This yields to:

$$\begin{aligned}\frac{d\tilde{A}_p(\omega,z)}{dz} = &-\left[\frac{\alpha}{2}+j\left(\frac{\beta_2}{2}(\omega-\omega_0)^2+\frac{\beta_3}{6}(\omega-\omega_0)^3+\gamma|A_p(\omega,z)|^2\right)\right]\tilde{A}_p(\omega,z)\\ &-\frac{g_B}{2A_eff}|\tilde{A}_{BS}(\omega_{BS},z)|^2\tilde{A}_p(\omega,z)\delta(\omega-\omega_c)\\ &-\frac{\beta_i}{2}\tilde{A}_p(\omega,z)\,, \end{aligned} \tag{7.5a}$$

$$\frac{d\tilde{A}_{BS}(\omega_{BS},z)}{dz} = \left[\frac{\alpha}{2} + j\left(\frac{\beta_2}{2}(\omega-\omega_0)^2 + \frac{\beta_3}{6}(\omega-\omega_0)^3 - \gamma|A_{BS}(\omega,z)|^2\right)\right]\tilde{A}_{BS}(\omega_{BS},z)$$
$$- \frac{g_B}{2A_{eff}}|\tilde{A}_p(\omega_c,z)|^2\tilde{A}_{BS}(\omega_{BS},z)$$
$$- \frac{\beta_i}{2\tilde{A}_{BS}(\omega_{BS},z)}|\tilde{A}_p(\omega_c,z)|^2 . \tag{7.5b}$$

In the right hand sides of (7.5a) and (7.5b), three terms are highlighted. The first accounts for the contribution of losses, GVD and Kerr nonlinearities (Appendix B). The second then represents the coupling term due to SBS and the third describes the spontaneous emissions initiating the Stokes wave generation.

Concerning the first part, only one remark is called for: in (7.5b) the signs are inverted compared to the pump wave. To avoid confusion, the position variable z increases in the same direction for both waves, but the Stokes wave is actually propagating backward and thus the opposite signs.

Moving on with analyzing the coupling term, the delta function in (7.5a) is due to our approximation of a single-frequency Stokes wave. The SBS gain is assumed constant, i.e. characterized by the Lorentzian profile of (7.2) with $\Delta\omega_B = 0$. This is a strong constraint on the results of our simulations but allows to reduce massively the complexity of the algorithm as we discuss later on.

Finally the last term was neglected in (7.1). This term models the thermal excitation of acoustic phonons initiating the generation of the Stokes wave. From (7.5b) it is clear that this contributions grows negligible as the Stokes wave builds up in power. Remark that β_i denotes the spontaneous emission factor which is not related to β_2 and β_3, i.e. GVD and third order dispersion.

Using the formulation of Appendix B, we can then rewrite (7.5) as:

$$\frac{d\tilde{A}_p(\omega,z)}{dz} = \left[\hat{N} + \hat{D} + \hat{S}_p\right]\tilde{A}_p(\omega,z) , \tag{7.6a}$$

$$\frac{d\tilde{A}_{BS}(\omega_{BS},z)}{dz} = \left[-\hat{N} - \hat{D} + \hat{S}_{BS}\right]\tilde{A}_{BS}(\omega_{BS},z) , \tag{7.6b}$$

where the linear $\hat{D}$ and nonlinear $\hat{N}$ operators are defined in (B.7) and (B.8) and the

Brillouin operators for pump and Stokes wave are given by:

$$\hat{S}_p = -\frac{g_B}{2A_e ff}|\tilde{A}_{BS}(\omega_{BS}, z)|^2 \delta(\omega - \omega_c) - \frac{\beta_i}{2}, \tag{7.7a}$$

$$\hat{S}_{BS} = -\frac{g_B}{2A_e ff}|\tilde{A}_p(\omega_c, z)|^2 - \frac{\beta_i}{2(\tilde{A}_{BS}(\omega_{BS}, z))^2}|\tilde{A}_p(\omega_c, z)|^2 . \tag{7.7b}$$

Note that, due to the spontaneous emission term the propagation of the Stokes wave cannot be easily solved with the Split-step Fourier method. In general, however, knowing the field propagation of the Stokes wave through the fiber is not one of our primary concerns. What we are interested in is the field propagation of the signal and to derive that only knowledge over the Stokes power is required.

7.3 Implementation and Validation of the Model

The main issue rising from the set of coupled equations presented in Section 7.2 is the counter-propagating characteristic of the two waves.
The problem described by (7.1) and (7.5) is a so called *boundary value problem* where the known boundary conditions are $A_p(0)$ and $A_{BS}(L) = 0$.

To simplify the problem we follow the approach presented in [62]. The algorithm to solve the propagation is split into two steps:

- A shooting algorithm is used to solve the boundary value problem described by the power equations of (7.1).[4]
- The gained knowledge over $P_{BS}(z)$ is used in $\hat{S}_p$ such that (7.6a) can be easily solved with Split-step Fourier method of Appendix B setting $\hat{D}' = \hat{D} + \hat{S}_p$.

A detailed analysis of the algorithm is presented in the next Subsections together with its validation.

[4] Actually, as specified later on, a normalized version of (7.1) with added the spontaneous emission term is used.

7.3.1 Shooting Algorithm Description

The first step consists in solving the power propagation through the fiber. To simplify the calculations the equations of (7.1) have been normalized both in space to the fiber length and in power to the input pump power. Furthermore the (normalized) spontaneous emission term has been added.

$$\frac{d\bar{P}_p}{d\zeta} = -G\bar{P}_p\bar{P}_{BS} - \alpha'\bar{P}_p - \beta_i'\bar{P}_p\,, \tag{7.8a}$$

$$\frac{d\bar{P}_{BS}}{d\zeta} = -G\bar{P}_p\bar{P}_{BS} + \alpha'\bar{P}_{BS} - \beta_i'\bar{P}_p\,, \tag{7.8b}$$

$$\tag{7.8c}$$

where $\zeta = -z/L$, $\bar{P}_i = P_i/P_p(0)$, $G = g_B L P_p(0)/A_{eff}$, $\alpha' = \alpha L$ ($\alpha_p = \alpha_{BS} = \alpha$) and $\beta_i' = \beta_i L$.

The algorithm implementing the shooting method is described by the flow chart of Figure 7.3. The procedure, designed modifying the proposal of [69] is based on an initial guess on $P_p(L)$. The power equations are then solved backward and the solution $P_p'(0)$ is compared with the known value. The guess is then refined accordingly and the process iterates until the error between known and calculated value is below a desired threshold (10^{-13} for our simulations[5]).

This procedure explains the reason behind our choice of a zero-linewidth Brillouin gain. Adding the frequency dependence to the model would require to have equations for the power spectral density rather than the total power. This in turn would imply the need to guess a whole spectrum instead of a single power value resulting in a massive increase of the complexity of the shooting algorithm.

The algorithm presented in [69] has then being refined in order to improve the convergence speed. The convergence parameter a is increased by a factor Y every X up and down shifts in a row to take care of the oscillations around the solution. Such parameters have been optimized and the value chosen are: $a = 30$, $Y = 20$, $X = 2$.

[5] A lower threshold would conflict with the numerical noise level of MATLAB® .

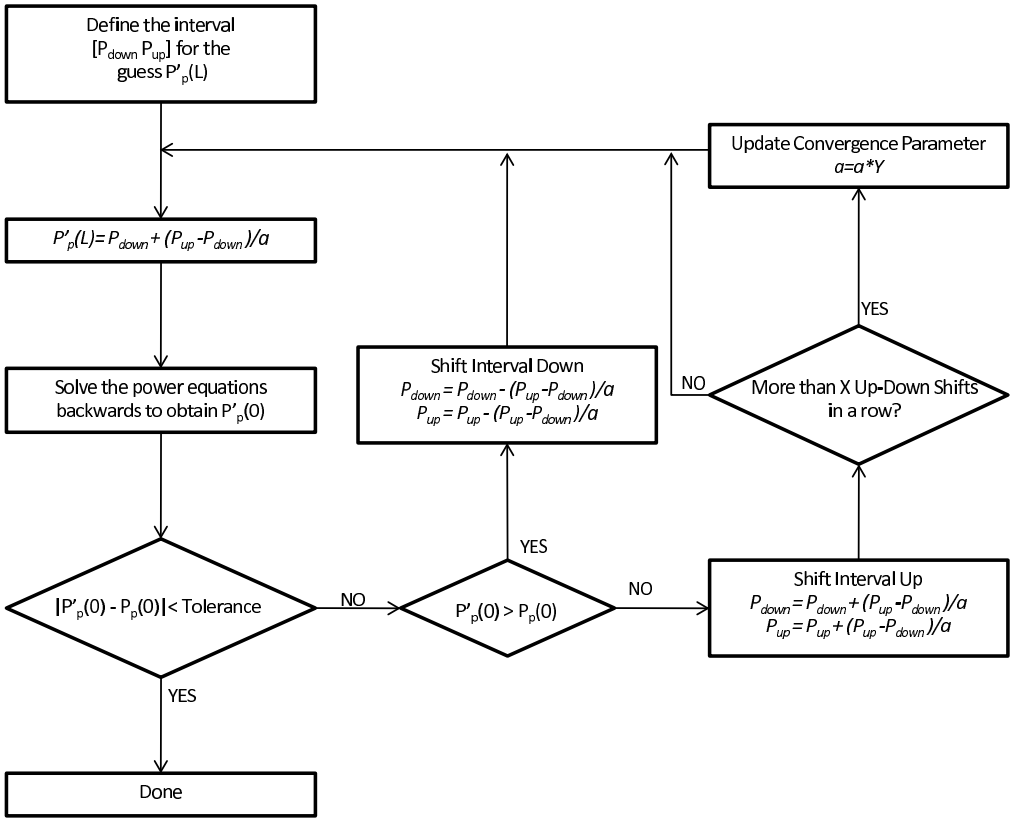

Figure 7.3: Shooting method flow chart inspired by [69].

Finally, the initial guess is set to half of the undepleted pump solution: $P_p(L) = 0.5 \cdot P_p(0)e^{-\alpha L}$. A more thorough optimization of the initial guess is expected to reduce the convergence time. Nevertheless with our choice the computational time was below 5 minutes on a standard personal computer.

Once the Stokes power is known, it is used inside $\hat{S}_p$ and the pump propagation (7.6a) is solved with the Split-step Fourier method.

7.3.2 Algorithm Validation

The algorithm implemented has been validated through comparison with the trends shown in [63] and [62]. Figure 7.4 show the first comparison.
The simulation have been carried on propagating a CW pump through a fiber defined by parameters reported in [63]. The Stokes field for $z = L$ has been set to $P_{BS}(L) = 10^{-9}$ W and $\beta_i' = 0$. Comparing the curves, good agreement is shown for the pump power. The

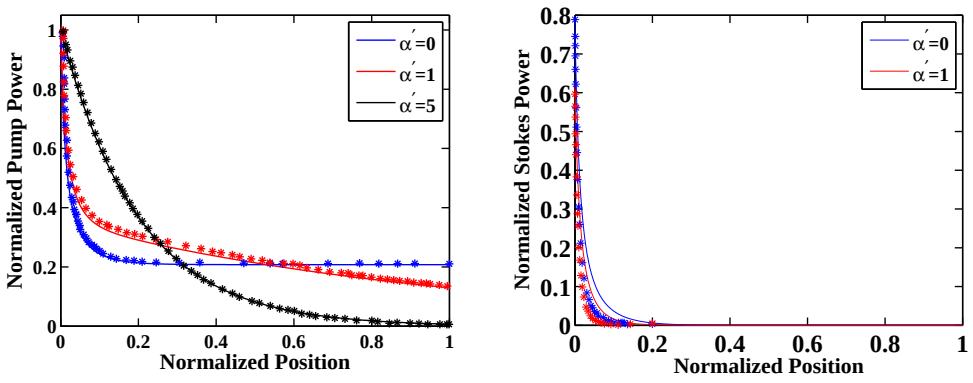

(a) (b)

Figure 7.4: Pump (a) and Stokes (b) wave power propagation inside an optical fiber: comparison between our simulations (continuous) and data (symbols) from [63].

Stokes field instead shows some discrepancies as in Figure 7.4(b).

Analyzing the case $\alpha' = 0$ (and $\beta_i' = 0$), we can see from (7.8) that the power difference $\bar{P}_p - \bar{P}_s$ should be a constant being the difference of the derivative equal to zero. Figure 7.5 shows that such power difference is indeed constant for our simulations while it has a exponential decay, as if $\alpha \neq 0$, for the data retrieved from [63]. This indicates a most probable typo in the article.

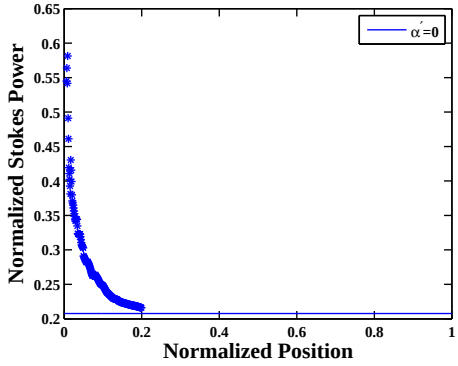

Figure 7.5: Power difference between pump and Stokes wave as function of the position inside the fiber: comparison between our simulations (continuous) and data (symbols) from [63].

A second validation has then been performed comparing the results of [62] with the curves calculated propagating a CW pump through the fiber characterized by the parameters reported in the article. The power propagation for Stokes and pump waves is shown in Figure 7.6.

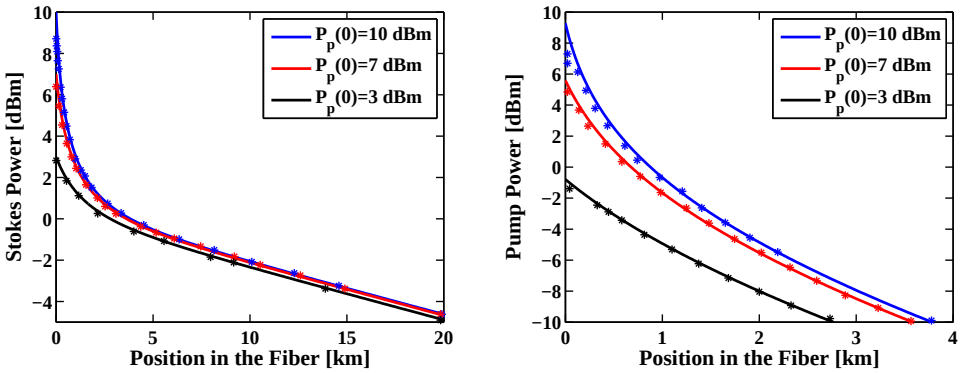

(a) (b)

Figure 7.6: Pump (a) and Stokes (b) wave power propagation inside an optical fiber: comparison between our simulations (continuous) and data (symbols) retrieved from [62].

A good agreement between our simulations and the results of [62] is shown for both pump and Stokes waves.

Finally one last verification has been performed. The consistency between the CW pump power obtained through the Split-step method P_{SSFM} and the solution of the shooting method P_{shooting} is examined. Figure 7.7(a) shows the comparison between the pump powers calculated with the two methods. A good agreement is shown, but the superposition between the two curves is strongly dependent on the step size Δz (Appendix B). Figure 7.7(b) shows the relative error between the power values calculated with the two methods for different step sizes. The relative error is defined as $|P_{\text{SSFM}} - P_{\text{shooting}}|/P_{\text{shooting}}$ where the shooting method is used as reference since it has been already validated. The fiber simulated is characterized by L = 300 m, α = 0.83 dB/km, γ = 11.6 $\text{W}^{-1}\cdot\text{km}^{-1}$, D = 0.22 ps/nm·km, S = 0.18 $\text{ps/nm}^2\cdot\text{km}$, λ_0 = 1549.3 nm, A_{eff} = 11.5 μm^2, β_i = $4.29 \cdot 10^{-8}$ m^{-1}, g_B = $5.67 \cdot 10^{-12}$ m/W as in [47]. The input pump power has been set to 20 dBm, ~ 2 dB above the fiber SBST.

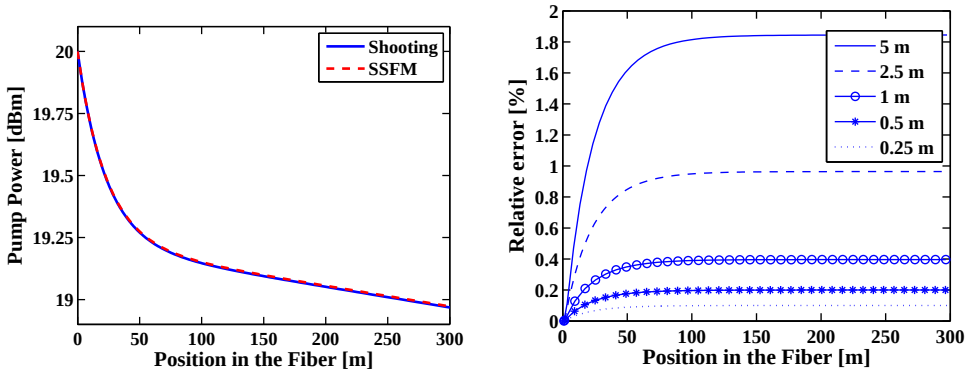

(a) Comparison (b) Relative Error

Figure 7.7: Pump power (a) as a function of the position in the fiber for the two methods with Δz =0.5. Relative error (b) between the power curves calculated with the two methods for various values of Δz.

The error of the Split-step solution is indeed reduced decreasing the step size. Furthermore the error originates at the input of the fiber, i.e. where the Stokes power is stronger, and asymptotically converges to a constant value when losses become dominant. Numerical errors made close to the fiber input propagate even when the effects of SBS become negligible resulting in a Split-step solution parallel to the Shooting curve but slightly higher. As the step size is reduced, the SBS effects are calculated with a higher precision and thus the relative error converges towards a smaller value.

7.3.3 Model Analysis

Standard optical fiber datasheets rarely report parameters relative to SBS. The solution dependence on two parameters particularly difficult to measure, β_i and $P_{BS}(L)$, is here investigated. Since a good agreement between shooting and Split-step algorithms has been demonstrated in the previous Subsection, only the power calculated through the shooting method is shown.

From the analysis of Section 7.2 we expect a low dependence of the solution on β_i. Figure 7.8 confirms such expectation. Both pump and Stokes power are shown as a function of the position inside the fiber for various values of β_i.

Concerning the boundary condition for the Stokes field, different approaches are sug-

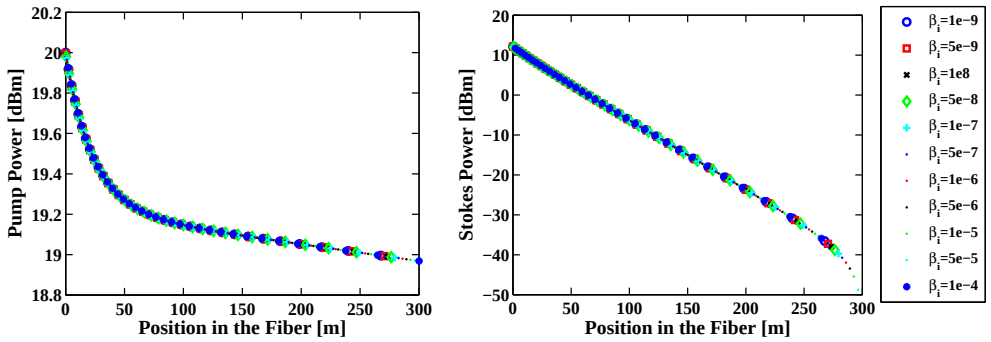

(a) (b)

Figure 7.8: Pump (a) and Stokes (b) power as a function of the position in the fiber for various values of β_i.

gested in literature [62, 63]. Figure 7.9 reports pump and Stokes power as function of the position for various values of $P_{BS}(L)$.

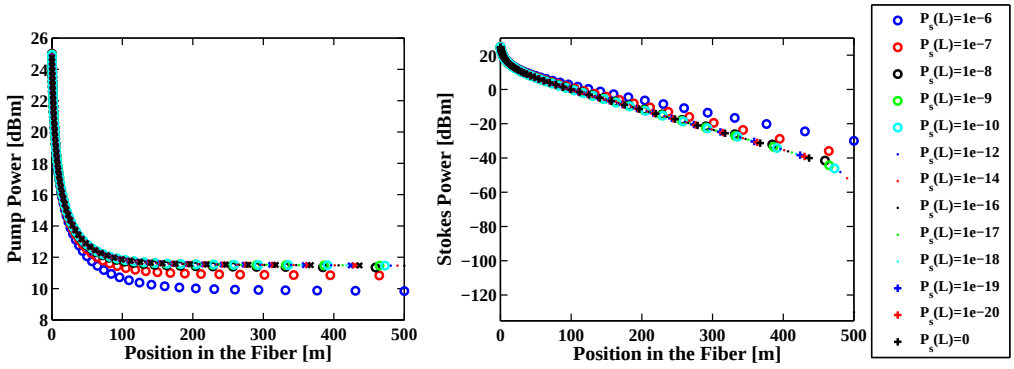

(a) (b)

Figure 7.9: Pump (a) and Stokes (b) power as a function of the position in the fiber for various values of $P_{BS}(L)$.

As for β_i we can see that no significant variations in the power curves can be noticed changing $P_{BS}(L)$, as long as it is kept around or below $P_{BS}(L) = 1$ nW, i.e. as in [63]. For boundary conditions higher that such value we can indeed see a deviation of the curves towards higher Stokes power and thus lower pump power. These high boundary values are however unrealistic. $P_{BS}(L)$ accounts for spontaneous emission noise which is inherently characterized by low power.

7.4 Analysis of Parametric Gain

The aim of this study on SBS is to analyze its effects on parametric processes. In this Section we investigate the maximization of the gain peak using a fiber link made of two spans, respectively the Ge and Al-doped HNLFs of [47]. The parameters of the two fibers are shown in Table 7.1. In our investigation we first highlight the impor-

	Ge-doped	Al-doped	Unit
L	298	179	m
α	0.83	15	dB/km
γ	11.6	7.4	$W^{-1}{\cdot}km^{-1}$
D	0.22	-0.12	ps/nm·km
S	0.18	0.011	$ps/nm^2{\cdot}km$
λ_0	1538	1562	nm
A_{eff}	11.5	13.5	μm^2
g_B	$5.67{\cdot}10^{-12}$	$1.67{\cdot}10^{-12}$	m/W
β_i	$4.296{\cdot}10^{-8}$	$4.296{\cdot}10^{-8}$	m^{-1}
P_{th}	18	28	dBm

Table 7.1: Fiber parameters from [47]

tance of SBS providing a comparison between parametric gain spectra with and without SBS. Then we show the power propagation through a two-fiber link varying the single fiber length to assess the influence of SBS on the pump power propagation. Finally we present a map showing the peak parametric gain as function of both the total length L_T of the fiber link and the ratio R_L between the length of the Al and the Ge doped HNLFs. In all analysis both the configurations with the Al-doped fiber first ("Al first") and with the Ge-doped fiber first ("Ge first") are analyzed.

7.4.1 Parametric Gain Spectra

In this Subsection we present the parametric gain spectra both with and without SBS effects. The parametric gain is calculated propagating through the fiber link a CW pump at 1560 nm together with a CW signal and sweeping the wavelength of the latter. The pump power is varied between 23 and 33 dBm with 1 dB-steps and the signal power is set to −50 dBm. A low signal power has been chosen both to avoid saturation and

neglect the Brillouin effects caused by the signal. The Stokes wave is thus calculated only on the pump power.

The results for the "Al first" configuration are shown in Figure 7.10.

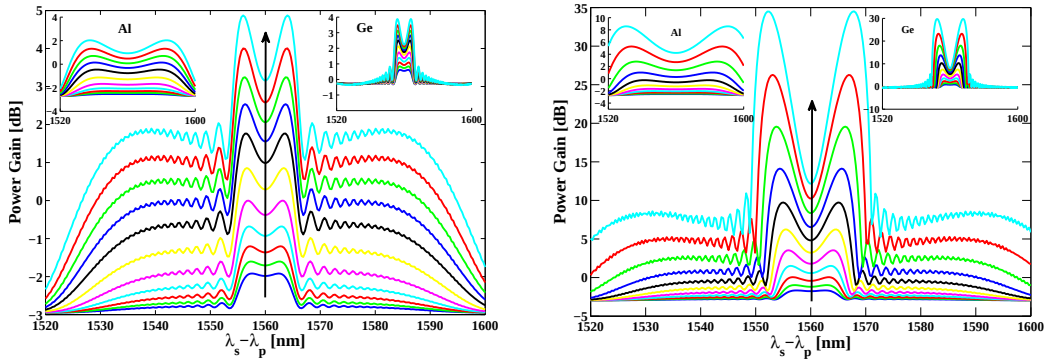

(a) With SBS

(b) Without SBS

Figure 7.10: **"Al first"** - Parametric gain spectra for pump power increasing in the direction indicated by the arrow: with (a) and without (b) SBS effects considered. The insets show the parametric gain in each fiber considered individually, Al-doped (left) and Ge-doped (right).

Comparing Figure 7.10(a) and 7.10(b), the main difference is the value of the peak gain. For a pump power of 33 dBm, neglecting the effects of SBS a gain as high as 35 dB can be achieved. When SBS is instead considered the gain is decreased of around 30 dB. For the same pump power, the gain bandwidth is then reduced from around 20 nm to less than 10 nm. The parametric gain bandwidth is indeed proportional to the pump power [15]. Since the pump is depleted by the power backscattered the gain spectrum becomes narrower. Both these effects, peak gain decrease and bandwidth shrinkage can be seen also in the gain spectra of the two fiber analyzed singularly[6] (insets).

Furthermore note that, regardless of Brillouin effects, the bandwidth of the Al-doped HNLF is larger than the Ge-doped and the peaks are not aligned. This is related to the different ZDW of the two fibers other than their dispersion slope. Aligning the peaks to the same wavelength however, would indeed increase the total gain.

[6]For the second stage the input power is set equal to the output power of the first stage and the gain is calculated with respect to that power level.

Finally both in Figure 7.10(a) and 7.10(b) we can notice that most of the amplification is provided by the Ge-doped fiber. This is consistent with its higher value for γ other than lower losses depleting the pump.

Analyzing now the "Ge first" configuration, the parametric gain spectra are shown in Figure 7.11.

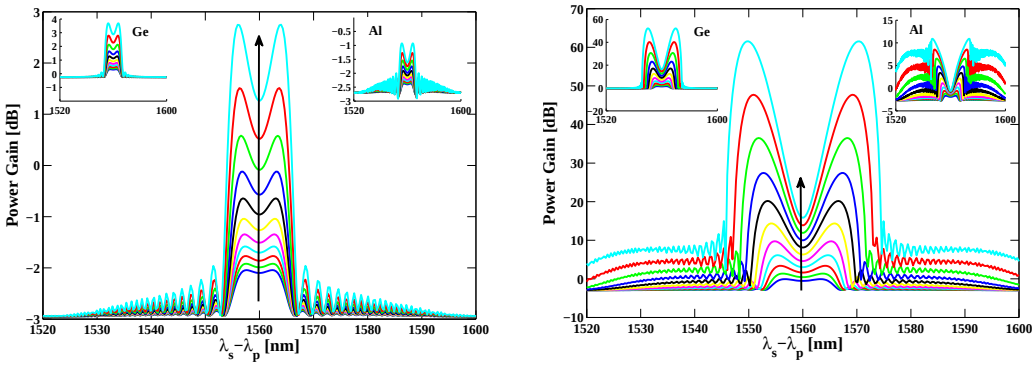

(a) With SBS

(b) Without SBS

Figure 7.11: **"Ge first"** - Parametric gain spectra for pump power increasing in the direction indicated by the arrow: with (a) and without (b) SBS effects considered. The insets show the parametric gain in each fiber considered individually, Ge-doped (left) and Al-doped (right).

The decrease of the parametric gain peak and the bandwidth shrinkage affects also this second configuration. Once again most of the gain is provided by the Ge-doped fiber but the influence of SBS is stronger than in the "Al first" case. In absence of SBS the dB of gain are almost doubled with respect to the previous configuration, indeed due to the higher power in input to the Ge-doped fiber. When instead SBS is depleting the pump the gain is slightly higher in the "Al first" scheme. In Figure 7.11(a) the gain provided by the Ge-doped HNLF is limited by pump depletion due to SBS.

To conclude, these simulations provide a good insight into the detrimental effects of SBS on parametric amplification. The Stokes wave "steals" power that could have otherwise been used to amplify the signal. In our simulations this results in a peak gain reduced to around 10% (in dB), and a bandwidth to less than half.

7.4.2 Fiber Length Variations in a Two-fiber Link

Figure 7.12 show the pump power propagation through the fiber link varying the length of the Al-doped fiber (Figure 7.12(a)) and of the Ge-doped (Figure 7.12(b)). The length has been varied from 90 to 110 % of the original length and the input power is $P_p(0)$ = 25 dBm so below threshold for the Al-doped HNLF but above for the Ge-doped. Note that such consideration stands only for small variations of the fiber length being the SBST dependent on L.

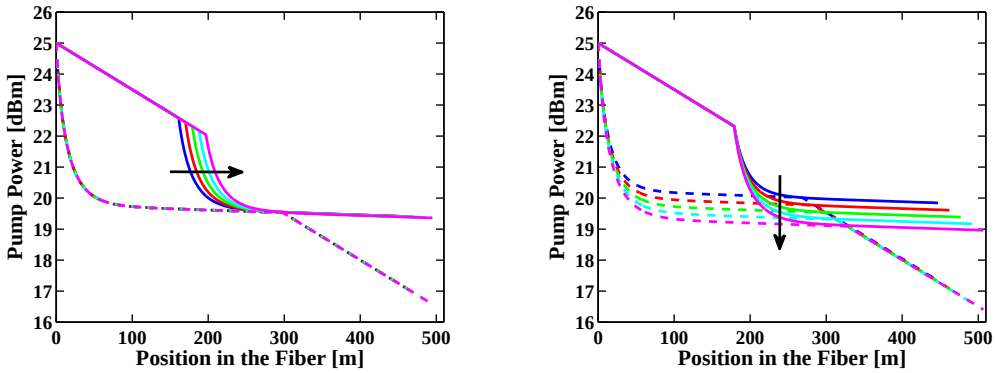

(a) Increasing L_1 (b) Increasing L_2

Figure 7.12: **$P_p(0)$ = 25 dB -** Pump power as function of the position in the fiber varying the length L_1 of the Al-doped HNLF (a) and L_2 of the Ge-doped HNLF (b) for "Al first" (continuous) and "Ge first" (dashed). The arrows point towards the direction of increase of the length.

As we can see in Figure 7.12(a), varying the length of the Al-doped fiber does not result in significant changes in the output power (Figure 7.12(a)). The difference between the curves (in both configurations) is due to the attenuation. The losses in the Al-doped HNLF are as high as 15 dB/km so increasing the length indeed changes the output power. Analyzing the two configurations separately we have that:

- When the pump is propagating first through the Al-doped fiber, a longer fiber causes higher losses and thus a lower power in input to the second fiber span. The lower power in turn results in lower effects of SBS in the Ge-doped fiber and thus the two phenomena compensate each other. This is to be expected however only when the output power is still above threshold for the Ge-doped HNLF (as in the case analyzed). The scenario with the output power below threshold for

the Ge-doped fiber is however of no interest for this analysis since no significant Brillouin effects would be shown.

- Concerning the configuration with the Ge-doped fiber first. Being the power at the output of the first fiber below threshold for the second one, the main effect shown is again attenuation.

When instead it is the Ge-doped fiber length that is varied (Figure 7.12(b)), the power is indeed reduced. In both configurations the increased amount of power lost is due to the higher effects of SBS in the Ge-doped HNLF. A longer fiber indeed results in an increase of the backscattered power.

When the power is increased beyond the SBST for the Al-doped HNLF, i.e. to 31 dBm, similar considerations can be made (Figure 7.13).

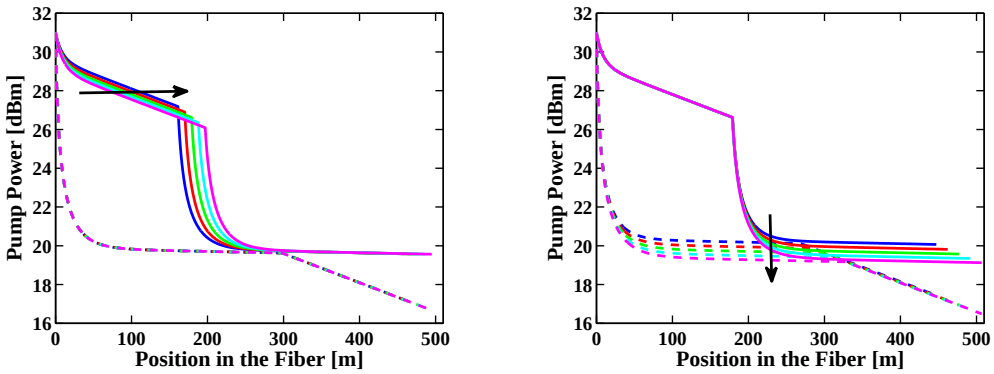

(a) Increasing L_1 (b) Increasing L_2

Figure 7.13: $\mathbf{P_p(0) = 31\ dB}$ **-** Pump power as function of the position in the fiber varying the length L_1 of the Al-doped HNLF (a) and L_2 of the Ge-doped HNLF (b) for "Al first" (continuous) and "Ge first" (dashed). The arrows point towards the direction of increase of the length.

When increasing the length of the Al-doped fiber (Figure 7.13(a)) the output power variations due to SBS are negligible. In this case however, for the "Al first" scheme, it is the higher power backscattered in the first fiber instead of the attenuation that is compensated in the second stage by the lower input power.
Furthermore, also variations in the length of the Ge-doped HNLF (Figure 7.13(b)) produce results similar to the Figure 7.12(b), so the same considerations apply.

Finally notice that we have always analyzed the "Ge first" configuration such that the input power for the Al-doped fiber is below SBST. A complete analysis would require to consider also the situation where it is above SBST. From our simulation however, this scenario was not achievable even injecting 40 dBm of power (unrealistic in an optical communication system) the output power was locked at ~20 dBm. This was expected since higher input power results in stronger Brillouin effects and so an almost unchanged output power.

7.4.3 Parametric Gain Peak Optimization

Finally the parametric gain peak is investigated as a function of both the total fiber length L_T and the ratio $R_L = L_1/L_2$, with L_i as in the previous Subsection. The two configurations are studied calculating the parametric gain for each set (L_T, R_L) with an input pump power of 30 dBm and a signal power of -50 dBm.

The results of our simulations are shown in Figure 7.14.

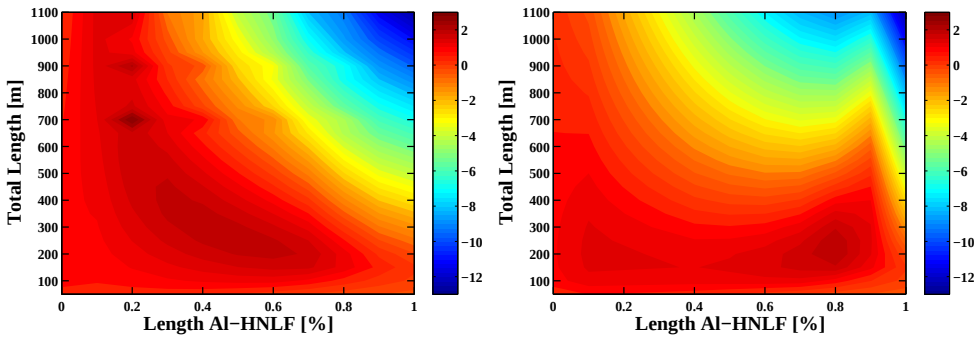

(a) "Al first" (b) "Ge first"

Figure 7.14: Peak parametric gain as a function of total length and ratio between the Al and Ge-doped length for the "Al first" (a) and "Ge first" (b) configurations. The input power is set to 30 dBm

Both the maps show the presence of maxima for specific values of L_T and R_L. To understand at least the general trend shown in the Figures we can compare with similar maps showing output pump power both at the first and the second stage, again for both configuration (Figure 7.15).

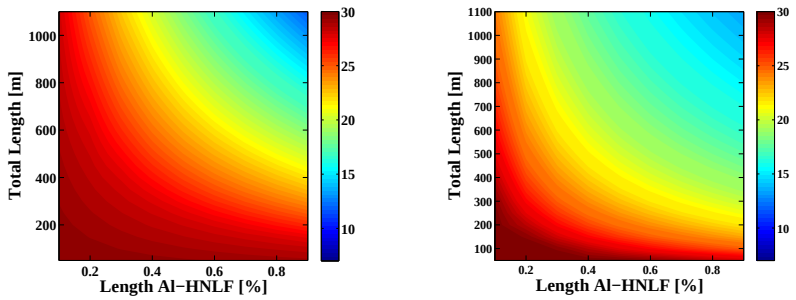

(a) "Al first" 1st stage

(b) "Ge first" 1st stage

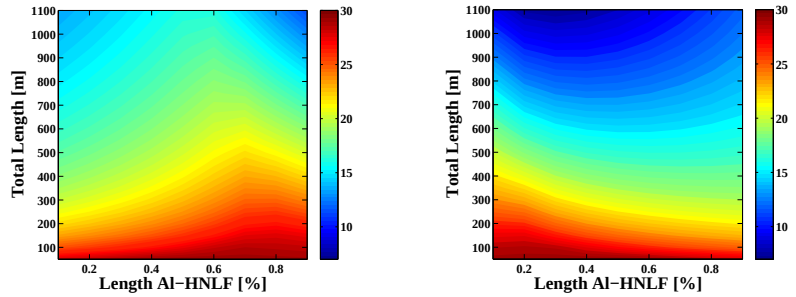

(c) "Al first" 2nd stage

(d) "Ge first" 2nd stage

Figure 7.15: Pump power at the output of the first (a)-(b) and second (c)-(d) fiber span as a function of L_T and R_L for the "Al first" (a)-(c) and "Ge first" (b)-(d) configurations. The input power is set to 30 dBm

Comparing Figure 7.14(a) with Figure 7.15(a) we can justify the decrease of parametric gain along the direction of increase of both L_T and R_T (diagonal of the Figure) with a decrease of the pump power. Concerning the second stage (Figure 7.15(c)) instead, a simple relation between the pump power and the parametric gain cannot be highlighted.

Similar comments can be made for the second configuration. Also in this case the first stage seems to have most of the influence on the general trend followed by the parametric gain peak. Nevertheless no straightforward relation can be defined overall.

Chapter 8

Conclusions and Future Work

The scope of this thesis was the analysis of all-optical signal regeneration for QPSK modulations through the use of PSA in FOPA.
In particular we have focused on two DP FOPA schemes in a respectively non-degenerate and degenerate configuration. The latter method has actually been proposed in this study and it has been developed starting from some conclusions drawn investigating the saturation regime of FOPAs. Both the regenerators have been discussed semi-analytically and optimized models have been implemented in MATLAB® in order to analyze their individual performances other than providing a comparison between the two.

The regenerators have been tested propagating NRZ, CSRZ and RZ 33% QPSK signals at 28 and 40 Gbaud and the reduction in the signal phase std and the improvement in the BER performances at the output have been investigated.

As illustrated in Chapter 6 the regeneration has been demonstrated by the significant increase in the performances. Phase stds improvements up to 80% and R-OSNR decreases up to 10 dB have been calculated for both the regeneration schemes. Furthermore error-free detection[1] has been shown for phase noise stds which would not have permitted it without regeneration.

The BER analysis has reported a good baudrate transparency for both the schemes. The baudrate dependence characterizing the output phase std when the non-degenerate

[1] "Error-free detection" needs to be read as discussed in Chapter 6.

scheme is used requires to investigate further the impact of phase squeezing and amplitude un-squeezing on the receiver.

Concerning the complexity of the schemes, the non-degenerate scheme requires two FOPA stages for the idler generation unlike the comb generator needed by degenerate case. The use of the idler-free configuration discussed in Section 4.4 has however the potential to ease the implementation.
The MZI of the proposed scheme, on the other hand, requires careful optimization and two identical HNLFs since the alignment of the responses in the two arms is critical. Nonetheless, mapping the MZI into a SI removes the need for two HNLFs and is thus expected to lower the tuning requirements.

Further studies are desirable to refine the results. First of all a reliable model for the phase noise generated through the propagation in optical fibers is required. As shown in [40] the measured performances are highly impacted by the chosen phase noise representation.

Furthermore, in this study we have analyzed regeneration performed at the receiver end. The regeneration performed within the optical link is indeed interesting for further research. The spacing of regenerators within an optical link needs to be evaluated according to the trade-off between minimizing their number and the abrupt increase in power penalty when the amount of phase noise in input to the regenerator reaches a certain threshold $\sigma_i \approx 12^\circ$ according to our results.

Finally, in the main part of our investigation SBS has been neglected in order to keep low the computational requirements. Nonetheless its detrimental effects have been discussed through a MATLAB® model simulating the dynamic behavior of SBS and a dual-fiber link made of an Al-doped and a Ge-doped HNLF has been optimized in length according to the maximum parametric gain. The consequent step would thus be the analysis of the regenerator schemes taking the Brillouin effects into account in order to reproduce more precisely the behavior of a practical scheme.

Appendix A

Optical Fibers

In this Appendix we briefly introduce and discuss the main parameters affecting the wave propagations through an optical fiber: losses, dispersion and nonlinearities. The equations describing the propagation are then analyzed in Appendix B.

A.1 Losses

An optical wave propagating through a fiber is attenuated by several physical effects [15]. The overall losses are usually defined by the attenuation constant α commonly expressed in dB/km and are related to the power $P(z)$ of a CW field through Beer's Law:

$$\frac{dP(z)}{dz} = -\alpha z\,. \tag{A.1}$$

In general, the attenuation (or "losses") is wavelength dependent as shown in Figure A.1 for a Corning LEAF©fiber.

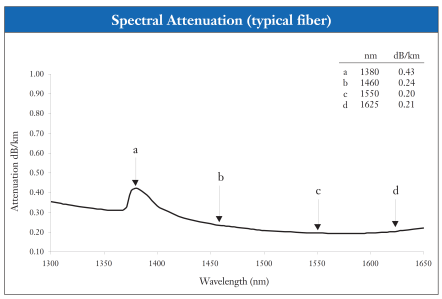

Figure A.1: Attenuation spectrum of a Corning LEAF©.

The attenuation spectrum however, shows a slow variation of α around 1550 nm, i.e. the wavelength window we use in our simulations. Throughout this thesis then, $\alpha(\lambda) = \alpha_0$.

Usual values of α for single mode fibers are on the order of $0.15 \div 0.2$ dB/km around λ =1550 nm. In this study however we deal mainly with HNLFs characterized by losses around $0.6 \div 1$ dB/km for common Ge-doped fibers. Then, due to the need to suppress SBS (Chapter 7), Al-doped fibers are also considered. The Al doping increase significantly the losses and values up to 15 dB/km are commonly reported [47, 64].

Finally losses determine the effective length of a fiber defined as:

$$L_{eff} = \frac{1 - e^{-\alpha L}}{\alpha}\,, \tag{A.2}$$

where L is the physical length of the fiber. The effective length plays an important role in determining properties like the SBST (7.4). When $\alpha L \gg 1$ it is common to approximate $L_{eff} \approx 1/\alpha$.

A.2 Dispersion

Under some approximation (Appendix B) the electrical field of an optical wave propagating through a fiber can be described as [15]:

$$E(z,t) = E(0,0)e^{i(\beta z - \omega t)}\,. \tag{A.3}$$

The propagation constant β is frequency dependent and can be Taylor expanded around the central frequency ω_0 used as reference frequency, yielding to:

$$\beta(\omega) \approx \beta_0 + \beta_1(\omega - \omega_0) + \frac{\beta_2}{2}(\omega - \omega_0)^2 + \frac{\beta_3}{6}(\omega - \omega_0)^3 + \frac{\beta_4}{24}(\omega - \omega_0)^4\,, \tag{A.4}$$

where $\beta_j = (d^j\beta/d\omega^j)_{\omega=\omega_0}$. Analyzing the different terms singularly we have:

- β_0 provides a constant phase term and so it is usually neglected;
- β_1 represents a constant delay in time. This is usually removed describing the wave through a reference frame moving with the pulse [54];
- β_2 is called GVD and defines the time delay $\Delta\tau$ accumulated by two co-propagating CW signals separated by a small frequency spacing $\Delta\omega$ [54]:

$$\Delta\tau = \frac{d\tau}{d\omega}\Delta\omega = \frac{d}{d\omega}\left(\frac{L}{v_g}\right)\Delta\omega \approx L\beta_2\Delta\omega\,,$$

where v_g is the group velocity defined as $v_g = d\omega/d\beta$. The GVD therefore represents the amount of broadening experienced by the optical pulse during the propagation;

- β_3 and β_4 are called respectively third and fourth-order dispersion parameter. These parameters are of particular importance when the system is tuned close to the zero-dispersion wavelength λ_0, i.e. the wavelength for which $\beta_2 = 0$.

In general for optical fibers it is customary to stop at the third order, β_4 is considered only for wavelengths close to λ_0.

An alternative wavelength representation equivalent to the frequency dependent β_j is also quite used. We define the dispersion parameter D and the dispersion slope S as:

$$D = -\frac{2\pi c}{\lambda^2}\beta_2\,, \tag{A.5a}$$

$$S = \left(\frac{2\pi c}{\lambda^2}\right)^2 \beta_3 + \frac{4\pi c}{\lambda^3}\beta_2\,. \tag{A.5b}$$

As for β_2 also D can be related to $\Delta\tau$ as $\Delta\tau \approx DL\Delta\lambda$.

Fiber manufacturers characterize optical fibers mainly through D and S. Typical values for HNLFs are of the order of $-3 \div 3$ ps/nm·km for D and $0.01 \div 0.03$ ps/nm^2·km for S [59, 70].

A.3 Nonlinearities

The nonlinearities affecting the waves propagation in optical fibers are mainly Kerr nonlinearities, stimulated Brillouin scattering (SBS) and Stimulated Raman Scattering. The first two are extensively discussed respectively in Chapter 2 and 7 while Raman scattering is usually negligible for our analysis [15].

Here then we limit ourselves to summarize the main parameters characterizing Kerr effects and SBS respectively:

- The nonlinear coefficient γ:

$$\gamma = \frac{2\pi n_2}{\lambda A_{eff}}\,, \tag{A.6}$$

with n_2 nonlinear refractive index and A_{eff} the effective area defined as [57],

$$A_{eff} = \frac{\left(\iint |F(x,y)|^2 dxdy.\right)^2}{\iint |F(x,y)|^4 dxdy.}. \tag{A.7}$$

Note that in (A.6) the nonlinear coefficient is frequency dependent. The variations are however not significant for the bandwidth of interest in our analysis so we assume γ constant [71]. For HNLFs the usual values of γ are of the order of $5 \div 20$ $\mathrm{W^{-1}{\cdot}km^{-1}}$ and A_{eff} around 10 $\mu\mathrm{m}^2$ [70, 71].

- The Brillouin gain g_B is strongly related to parameters of both the fiber and the propagating wave. For a complete formulation refer to [58]. The values of g_B are usually of the order of $10^{-12} \div 10^{-11}$ $\mathrm{m{\cdot}W^{-1}}$ [59].

Appendix B

Wave Propagation in a Single Mode Fiber

In this appendix we describe the model used to numerically calculate the wave propagation through an optical fiber. First of all we derive the NLSE theoretically and then we present the Split-step Fourier method to solve numerically the equation.

B.1 Nonlinear Schrödinger Equation

The propagation of optical signals through a single mode fiber is governed by Maxwell's equations leading to the wave equation [57]:

$$\nabla \times \nabla \times \mathbf{E} + \frac{1}{c^2}\frac{\partial^2 \mathbf{E}}{\partial t^2} = -\mu_0 \frac{\partial^2 \mathbf{P}}{\partial^2 t}\,, \tag{B.1}$$

where $\mathbf{E}$ and $\mathbf{P}$ are respectively electric field and induced electric polarization, μ_0 is the vacuum permeability and c the speed of light.

To solve further the equations simplifying assumptions are commonly made [54].

First of all we assume a small refractive index difference between core and cladding, *weakly guiding approximation*. In a single mode fiber this assumption allows to assume the electrical field linearly polarized. Furthermore, we assume the electric field separable into a transverse field distribution $F(x, y, \omega)$ (generally Gaussian) and a component along the direction of propagation $B(z, \omega)$. This latter is assumed harmonic in z due

to the cylindrical symmetry of the fiber. The electrical field can thus be expressed as:

$$\tilde{\mathbf{E}}(\mathbf{r},\omega) = \hat{\mathbf{x}}F(x,y,\omega)\tilde{B}(0,\omega)e^{i\beta z}\,, \tag{B.2}$$

with $\hat{\mathbf{x}}$ polarization unit vector, $\tilde{B}(0,\omega)$ initial amplitude and β propagation constant.

Then, the carrier frequency of the wave (ω_0) is assumed much greater than its spectral width ($\Delta\omega$), *slow varying envelope approximation*. This allows neglecting the frequency dependence of $F(x,y)$ and to write the optical field amplitude in the time domain as:

$$B(z,t) = \mathcal{F}^{-1}[\tilde{B}(z,\omega)] = A(z,t)e^{i(\beta_0 z-\omega_0 t)}\,, \tag{B.3}$$

where $\mathcal{F}^{-1}$ represents the inverse Fourier transformation [72, (1.6.2)] and β_0 is the first term of the Taylor expansion as in (A.4).
From the wave equation we can split the polarization into linear $\mathbf{P}_L$ and nonlinear $\mathbf{P}_{NL}$ components. The weakly guiding approximation allows considering the latter a small perturbation of the former. Combining (A.4) and (B.3) into (B.2) and inserting it into (B.1) after some math [57] yields to:

$$\frac{\partial A(z,t)}{\partial z} + \beta_1\frac{\partial A(z,t)}{\partial t} + \frac{i\beta_2}{2}\frac{\partial^2 A(z,t)}{\partial t^2} - \frac{\beta_3}{6}\frac{\partial^3 A(z,t)}{\partial t^3} = -\frac{\alpha}{2}A(z,t) + i\gamma|A(z,t)|^2A(z,t)\,, \tag{B.4}$$

Using the substitution $t' = t-\beta_1 z$, we can remove the term in β_1. The well-known NLSE can then be written as:

$$\begin{aligned}\frac{\partial}{\partial z}A(z,t) = &-\frac{\alpha}{2}A(z,t) && \text{(losses)}\\ &-i\frac{\beta_2}{2}\frac{\partial^2}{\partial t^2}A(z,t) && \text{(GVD)}\\ &+\frac{\beta_3}{6}\frac{\partial^3}{\partial t^3}A(z,t) && \text{(third order dispersion)}\\ &+i\gamma|A(z,t)|^2A(z,t) && \text{(Kerr nonlinearities)}\end{aligned} \tag{B.5}$$

First of all note that the frequency dependence for both losses and nonlinear coefficient has been dropped and they are assumed constant as discussed in Appendix A. Then, in the above expression for the NLSE, Raman and self-steepening effects are neglected. These effects are however negligible for pulses wider than 1 ps as the ones considered in this study [57].

Furthermore also Brillouin effects have been neglected in order to keep low the computational complexity of our simulations. Nonetheless SBS represents a strong impairment for parametric amplification depleting the pump and thus reducing the gain. A dynamic model for SBS which improves (B.5) is discussed in Chapter 7.
Finally also PMD is not considered by (B.5). Other than assuming the field linearly polarized we consider the polarization constant along the propagation.

B.2 Split-step Fourier Method

When both Kerr nonlinearities and GVD are present, the NLSE cannot be solved analytically other than in the special case of soliton propagation. Several numerical methods have therefore being proposed to provide a solution, one of the most used is known as *Split-step Fourier method*. This is the method we use to model the propagation through the fiber.

We start by rewriting (B.5) as:

$$\frac{\partial}{\partial z}A(z,t) = \left(\hat{D}(t) + \hat{N}(z,t)\right)A(z,t)\,, \tag{B.6}$$

where the linear $\hat{D}$ and nonlinear $\hat{N}$ operators are defined as:

$$\hat{D}(\omega) \;=\; -\frac{\alpha}{2} + i\left(\frac{\beta_2}{2}(\omega-\omega_0)^2 + \frac{\beta_3}{6}(\omega-\omega_0)^3\right), \tag{B.7}$$

$$\hat{N}(z,t) = -i\gamma|A(z,t)|^2\,, \tag{B.8}$$

if the fourth order dispersion is considered a term $i\beta_4(\omega-\omega_0)^4/24$ is added to (B.7). In general, unless stated otherwise, β_4 is assumed zero.

The Split-step Fourier method consists in applying the two operators separately: the linear part is solved in the frequency domain, the nonlinear part in the time domain. This is the reason why $\hat{D}$ is expressed as function of ω in (B.7).
Neglecting $\hat{N}$ yields to:

$$\frac{\partial}{\partial z}\tilde{A}(z,\omega) = \hat{D}(\omega)\tilde{A}(z,\omega) \quad\rightarrow\quad \tilde{A}(z+\Delta z,\omega) = \tilde{A}(z,\omega)e^{\hat{D}(\omega)\Delta z}\,, \tag{B.9}$$

where $\tilde{A}(z,\omega)$ is the Fourier transform of $A(z,t)$.

Concerning the nonlinear part instead, assuming Δz small enough we can approximate:

$$\int_z^{z+\Delta z} N(z)dz \approx N(z)\Delta z\,,$$

and thus write:

$$\frac{\partial}{\partial z}A(z,t) = \hat{N}(z,t)A(z,t) \quad \rightarrow \quad A(z+\Delta z,t) = A(z,t)e^{N(\hat{z},t)\Delta z}\,. \tag{B.10}$$

Combining the two steps yields to:

$$A(z+\Delta z,t) \approx \mathcal{F}^{-1}\left\{e^{\hat{D}(\omega)\Delta z}\mathcal{F}\left\{e^{\hat{N}(z,t)\Delta z}A(z,t)\right\}\right\}\,, \tag{B.11}$$

By applying (B.11), for a number of times equal to the fiber length divided by Δz the wave at the output of the fiber can be calculated with a precision increasing for decreasing step sizes.

This implementation is known as unsymmetrical Split-step. In this study, we have implemented a symmetrical version which is based on the use of a first half linear step of size $\Delta z/2$, a set of steps as in (B.11), and at the end again a half linear step.
The advantage of this symmetrical approach is that the error is reduced. The unsymmetrical approach is accurate to the second order in the step Δz, while the symmetrical method the error term is proportional to the third order in Δz [57]. The error rises when applying separately linear and nonlinear operators, i.e. assuming they commute. This is not the case for $\hat{D}$ and $\hat{N}$, so the error is proportional to the commutator which is different in the unsymmetrical and symmetrical scheme.

A graphical explanation of the symmetrical Split-step Fourier method is shown in Figure B.1

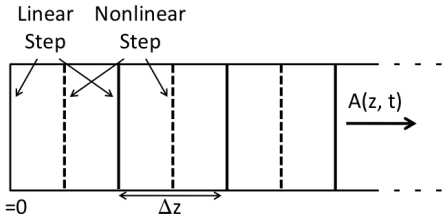

Figure B.1: Graphical explanation of the symmetrical Split-step Fourier method as in [57]. The nonlinear step is calculated between the dashed midplane lines.

Bibliography

[1] M. Seimetz, *High-Order Modulation for Optical Fiber Transmission (Springer Series in Optical Sciences)*. Springer, 1 ed., Jun. 2009.

[2] R. Griffin, R. Johnstone, R. Walker, J. Hall, S. Wadsworth, K. Berry, A. Carter, M. Wale, J. Hughes, P. Jerram, and N. Parsons, "10 gb/s optical differential quadrature phase shift key (dqpsk) transmission using gaas/algaas integration," in *Optical Fiber Communication Conference and Exhibit, 2002. OFC 2002*, pp. FD6 1–3, Mar. 2002.

[3] R. Griffin and A. Carter, "Optical differential quadrature phase-shift key (odqpsk) for high capacity optical transmission," in *Optical Fiber Communication Conference and Exhibit, 2002. OFC 2002*, pp. 367–368, Mar. 2002.

[4] R. Slavík, J. Kakande, F. Parmigiani, L. Grüner-Nielsen, D. Jakobsen, S. Herstrøm, P. Petropoulos, and D. Richardson, "All-optical phase-regenerative multicasting of 40 gbit/s dpsk signal in a degenerate phase sensitive amplifier," in *Optical Communication (ECOC), 2010 36th European Conference and Exhibition on*, pp. 1–3, Sept. 2010.

[5] Y. H. Wen, O. Kuzucu, T. Hou, M. Lipson, and A. L. Gaeta, "All-optical switching of a single resonance in silicon ring resonators," *Opt. Lett.*, vol. 36, pp. 1413–1415, Apr. 2011.

[6] I. Kang, C. Dorrer, L. Zhang, M. Rasras, L. Buhl, A. Bhardwaj, S. Cabot, M. Dinu, X. Liu, M. Cappuzzo, L. Gomez, A. Wong-Foy, Y. Chen, S. Patel, D. Neilson, J. Jacques, and C. Giles, "Regenerative all optical wavelength conversion of 40-gb/s dpsk signals using a semiconductor optical amplifier mach-zehnder interferometer," in *Optical Communication, 2005. ECOC 2005. 31st European Conference on*, vol. 6, pp. 29–30 vol.6, Sept. 2005.

[7] M. Matsumoto, "Regeneration of Phase Encoded Signals: Different Schemes and Future Issues," in *ECOC'10*, pp. 1–14, 2010.

[8] K. Croussore, C. Kim, and G. Li, "All-optical regeneration of differential phase-shift keying signals based on phase-sensitive amplification," *Opt. Lett.*, vol. 29, pp. 2357–2359, Oct. 2004.

[9] P. Andrekson, C. Lundström, and Z. Tong, "Phase-sensitive fiber-optic parametric amplifiers and their applications," in *Optical Communication (ECOC), 2010 36th European Conference and Exhibition on*, pp. 1–6, Sept. 2010.

[10] A. Bogris and D. Syvridis, "Rz-dpsk signal regeneration based on dual-pump phase-sensitive amplification in fibers," *Photonics Technology Letters, IEEE*, vol. 18, pp. 2144–2146, Oct. 2006.

[11] J. Kakande, A. Bogris, R. Slavík, F. Parmigiani, D. Syvridis, P. Petropoulos, and D. Richardson, "First demonstration of all-optical qpsk signal regeneration in a novel multi-format phase sensitive amplifier," in *Optical Communication (ECOC), 2010 36th European Conference and Exhibition on*, pp. 1–3, Sept. 2010.

[12] J. Kakande, F. Parmigiani, R. Slavík, L. Grüner-Nielsen, D. Jakobsen, S. Herstrøm and, P. Petropoulos, and D. Richardson, "Saturation effects in degenerate phase sensitive fiber optic parametric amplifiers," in *Optical Communication (ECOC), 2010 36th European Conference and Exhibition on*, pp. 1–3, Sept. 2010.

[13] J. Hansryd, P. A. Andrekson, M. Westlund, J. Li, and P. O. Hedekvist, "Fiber-based optical parametric amplifiers and their applications," *Selected Topics in Quantum Electronics, IEEE Journal of*, vol. 8, pp. 506–520, May 2002.

[14] N. Shibata, R. Braun, and R. Waarts, "Phase-mismatch dependence of efficiency of wave generation through four-wave mixing in a single-mode optical fiber," *Quantum Electronics, IEEE Journal of*, vol. 23, pp. 1205–1210, Jul. 1987.

[15] M. Marhic, *Fiber Optical Parametric Amplifiers, Oscillators and Related Devices*. Cambridge: Cambridge University Press, 2007.

[16] Y. Chen and A. W. Snyder, "Four-photon parametric mixing in optical fibers: effect of pump depletion," *Opt. Lett.*, vol. 14, pp. 87–89, Jan. 1989.

[17] C. Lundström, J. Kakande, P. Andrekson, Z. Tong, M. Karlsson, P. Petropoulos, F. Parmigiani, and D. Richardson, "Experimental comparison of gain and saturation characteristics of a parametric amplifier in phase-sensitive and phase-insensitive mode," in *Optical Communication, 2009. ECOC '09. 35th European Conference on*, pp. 1–2, Sept. 2009.

[18] Y. Yamamoto and T. Mukai, "Fundamentals of optical amplifiers," *Optical and Quantum Electronics*, vol. 21, pp. S1–S14, 1989. 10.1007/BF02117679.

[19] M. Matsumoto, "All-optical signal regeneration using fiber nonlinearity," in *2009 IEEE/LEOS Winter Topicals Meeting Series*, pp. 250–251, Ieee, Jan. 2009.

[20] A. Hirano, T. Kataoka, S. Kuwahara, M. Asobe, and Y. Yamabayashi, "All-optical limiter circuit based on four-wave mixing in optical fibres," *Electronics Letters*, vol. 34, pp. 1410–1411, Jul. 1998.

[21] E. Ciaramella and S. Trillo, "All-optical signal reshaping via four-wave mixing in optical fibers," *Photonics Technology Letters, IEEE*, vol. 12, pp. 849 –851, Jul. 2000.

[22] Y. Li, K. Croussore, C. Kim, and G. Li, "All-optical 2r regeneration using data-pumped fibre parametric amplification," *Electronics Letters*, vol. 39, pp. 1263–264, Aug. 2003.

[23] M. Matsumoto, "A fiber-based all-optical 3r regenerator for dpsk signals," *Photonics Technology Letters, IEEE*, vol. 19, pp. 273–275, Mar., 2007.

[24] M. Matsumoto and H. Sakaguchi, "DPSK signal regeneration using a fiber-based amplitude regenerator.," *Optics express*, vol. 16, pp. 11169–75, Jul. 2008.

[25] P. Vorreau, A. Marculescu, J. Wang, G. Bottger, B. Sartorius, C. Bornholdt, J. Slovak, M. Schlak, C. Schmidt, S. Tsadka, W. Freude, and J. Leuthold, "Cascadability and regenerative properties of soa all-optical dpsk wavelength converters," *Photonics Technology Letters, IEEE*, vol. 18, pp. 1970–1972, Sept. 2006.

[26] M. Shin, P. Devgan, V. Grigoryan, and P. Kumar, "Snr improvement of dpsk signals in a semiconductor optical regenerative amplifier," *Photonics Technology Letters, IEEE*, vol. 18, pp. 49–51, 1, 2006.

[27] R. Elschner, A. M. de Melo, C.-A. Bunge, and K. Petermann, "Noise suppression properties of an interferometer-based regenerator for differential phase-shift keying data," *Opt. Lett.*, vol. 32, pp. 112–114, Jan. 2007.

[28] M. Matsumoto and K. Sanuki, "Performance improvement of dpsk signal transmission by a phase-preserving amplitude limiter," *Opt. Express*, vol. 15, pp. 8094–8103, Jun. 2007.

[29] C. Peucheret, M. Lorenzen, J. Seoane, D. Noordegraaf, C. Nielsen, L. Gruner-Nielsen, and K. Rottwitt, "Amplitude regeneration of rz-dpsk signals in single-pump fiber-optic parametric amplifiers," *Photonics Technology Letters, IEEE*, vol. 21, pp. 872–874, Jul. 2009.

[30] M. Sköld, M. Karlsson, S. Oda, H. Sunnerud, and P. A. Andrekson, "Constellation diagram measurements of induced phase noise in a regenerating parametric amplifier," in *OFC/NFOEC 2008 - 2008 Conference on Optical Fiber Communication/National Fiber Optic Engineers Conference*, pp. 2–4, 2008.

[31] A. Striegler and B. Schmauss, "All-optical dpsk signal regeneration based on cross-phase modulation," *Photonics Technology Letters, IEEE*, vol. 16, pp. 1083–1085, Apr. 2004.

[32] A. Striegler, M. Meissner, K. Cvecek, K. Sponsel, G. Leuchs, and B. Schmauss, "Nolm-based rz-dpsk signal regeneration," *Photonics Technology Letters, IEEE*, vol. 17, pp. 639–641, Mar. 2005.

[33] C. Stephan, K. Sponsel, G. Onishchukov, B. Schmauss, and G. Leuchs, "Cascaded phase-preserving amplitude regeneration in a dpsk transmission system," in *Optical Communication, 2009. ECOC '09. 35th European Conference on*, pp. 1–2, Sept. 2009.

[34] Q. T. Le, A. O'Hare, L. Bramerie, M. Gay, H. trung Nguyen, J. louis Oudar, M. Joindot, and J. C. Simon, "All-optical phase-preserving amplitude regeneration of 28-gbaud rz-dqpsk signals with a microcavity saturable absorber in a recirculating loop experiment," in *Optical Fiber Communication Conference*, p. OMT5, Optical Society of America, 2011.

[35] R. Slavík, J. Kakande, F. Parmigiani, L. Grüner-Nielsen, R. Phelan, J. Vojtěch, P. Petropoulos, and D. Richardson, "Field-trial of an all-optical psk regenerator in a 40 gbit/s, 38 channel dwdm transmission experiment," in *National Fiber Optic Engineers Conference*, p. PDPA7, Optical Society of America, 2011.

[36] K. Croussore and G. Li, "Amplitude regeneration of rz-dpsk signals based on four-wave mixing in fibre," *Electronics Letters*, vol. 43, no. 3, pp. 177–178, 2007.

[37] C. Lundström, B. Puttnam, Z. Tong, M. Karlsson, and P. Andrekson, "Experimental characterization of the phase squeezing properties of a phase-sensitive parametric amplifier in non-degenerate idler configuration," in *Optical Communication (ECOC), 2010 36th European Conference and Exhibition on*, pp. 1–3, Sept. 2010.

[38] C. McKinstrie and S. Radic, "Phase-sensitive amplification in a fiber," *Opt. Express*, vol. 12, pp. 4973–4979, Oct 2004.

[39] C. Gerry and P. Knight, *Introductory quantum optics*. Cambridge University Press, 2005.

[40] P. Frascella, S. Sygletos, F. Gunning, R. Weerasuriya, L. Grüner-Nielsen, R. Phelan, J. O'Gorman, and A. Ellis, "Dpsk signal regeneration with a dual-pump nondegenerate phase-sensitive amplifier," *Photonics Technology Letters, IEEE*, vol. 23, pp. 516–518, Apr. 2011.

[41] X. Tang, L. Xi, and X. Zhang, "Phase regeneration of DPSK/DQPSK signals based on phase-sensitive amplification," in *Society of Photo-Optical Instrumentation Engineers (SPIE) Conference Series*, vol. 7136 of *Presented at the Society of Photo-Optical Instrumentation Engineers (SPIE) Conference*, Nov. 2008.

[42] K. Croussore, *All-optical regeneration for phase-shift keyed optical communication systems*. PhD thesis, University of Central Florida, 2007.

[43] J. Kakande, A. Bogris, R. Slavík, F. Parmigiani, D. Syvridis, P. Petropoulos, D. Richardson, M. Westlund, and M. Sköld, "Qpsk phase and amplitude regeneration at 56 gbaud in a novel idler-free non-degenerate phase sensitive amplifier," in *Optical Fiber Communication Conference*, p. OMT4, Optical Society of America, 2011.

[44] F. Mogensen, H. Olesen, and G. Jacobsen, "Locking conditions and stability properties for a semiconductor laser with external light injection," *IEEE Journal of Quantum Electronics*, vol. 21, pp. 784–793, Jul. 1985.

[45] P. Bhansali and J. S. Roychowdhury, "Gen-adler: the generalized adler's equation for injection locking analysis in oscillators," in *Asia and South Pacific Design Automation Conference*, pp. 522–527, 2009.

[46] G. Bosco, A. Carena, V. Curri, R. Gaudino, P. Poggiolini, and S. Benedetto, "Suppression of spurious tones induced by the split-step method in fiber systems simulation," *Photonics Technology Letters, IEEE*, vol. 12, pp. 489–491, May 2000.

[47] L. Grüner-Nielsen, S. Dasgupta, M. Mermelstein, D. Jakobsen, S. Herstrøm, M. Pedersen, E. Lim, S. Alam, F. Parmigiani, D. Richardson, and B. Pálsdóttir, "A silica based highly nonlinear fibre with improved threshold for stimulated brillouin scattering," in *Optical Communication (ECOC), 2010 36th European Conference and Exhibition on*, pp. 1–3, Sept. 2010.

[48] C. Peucheret, "Note on Optical DQPSK Modulation," 2003.

[49] F. MacWilliams and N. Sloane, "Pseudo-random sequences and arrays," *Proceedings of the IEEE*, vol. 64, pp. 1715–1729, Dec. 1976.

[50] P. Ramantanis, H. Badaoui, and Y. Frignac, "Quaternary sequences comparison for the modeling of optical dqpsk dispersion managed transmission systems," in *Optical Fiber Communication Conference*, p. OThC5, Optical Society of America, 2009.

[51] H. Badaoui, Y. Frignac, P. Ramantanis, B. E. Benkelfat, and M. Feham, "PRQS Sequences Characteristics Analysis by Auto-correlation Function and Statistical Properties," *Journal of Computer Science*, vol. 7, no. 4, pp. 39–44, 2010.

[52] Z. Zheng, L. An, Z. Li, X. Zhao, J. Yan, and X. Liu, "All-optical regeneration of dqpsk/qpsk signals based on phase-sensitive amplification," in *Optical Fiber communication/National Fiber Optic Engineers Conference, 2008. OFC/NFOEC 2008. Conference on*, pp. 1–3, Feb. 2008.

[53] M. Serbay, *Multilevel Modulation Formats for Optical Communication Systems Based on Direct Detection*. PhD thesis, Christian-Albrechts-Universität zu Kiel, 2007.

[54] G. Agrawal, *Fiber-optic communication systems*. No. v. 1 in Wiley series in microwave and optical engineering, Wiley-Interscience, 2002.

[55] M. Jeruchim, "Techniques for estimating the bit error rate in the simulation of digital communication systems," *Selected Areas in Communications, IEEE Journal on*, vol. 2, pp. 153–170, Jan. 1984.

[56] "G.975 'Forward error correction for submarine systems'."

[57] G. Agrawal, *Nonlinear fiber optics*. Optics and Photonics, Academic Press, 2007.

[58] A. Kobyakov, M. Sauer, and D. Chowdhury, "Stimulated brillouin scattering in optical fibers," *Adv. Opt. Photon.*, vol. 2, pp. 1–59, Mar. 2010.

[59] J. H. Lee, T. Tanemura, K. Kikuchi, T. Nagashima, T. Hasegawa, S. Ohara, and N. Sugimoto, "Experimental comparison of a kerr nonlinearity figure of merit including the stimulated brillouin scattering threshold for state-of-the-art nonlinear optical fibers," *Opt. Lett.*, vol. 30, pp. 1698–1700, Jul. 2005.

[60] L. A. Coldren and S. W. Corzine, *Diode Lasers and Photonic Integrated Circuits*. Wiley, 1995.

[61] F. G. Gebhardt and D. C. Smith, "Effects of diffraction of the self-induced thermal distortion of a laser beam in a crosswind," *Appl. Opt.*, vol. 11, pp. 244–248, Feb. 1972.

[62] A. Djupsjöbacka, G. Jacobsen, and B. Tromborg, "Dynamic stimulated brillouin scattering analysis," *J. Lightwave Technol.*, vol. 18, p. 416, Mar. 2000.

[63] P. Bayvel and P. Radmore, "Solutions of the sbs equations in single mode optical fibres and implications for fibre transmission systems," *Electronics Letters*, vol. 26, pp. 434–436, Mar. 1990.

[64] L. Grüner-Nielsen, S. Herstrøm, S. Dasgupta, D. Richardson, D. Jakobsen, P. Andrekson, M. Pedersen, and B. Pálsdóttir, "Silica-based highly nonlinear fibers with a high sbs threshold," in *Winter Topicals (WTM), 2011 IEEE*, pp. 171–172, Jan. 2011.

[65] C. Lundström, Z. Tong, and P. Andrekson, "Optical modulation signal enhancement using a phase sensitive amplifier," in *Optical Fiber Communication Conference*, p. OWL6, Optical Society of America, 2011.

[66] M.-J. Li, X. Chen, J. Wang, S. Gray, A. Liu, J. A. Demeritt, A. B. Ruffin, A. M. Crowley, D. T. Walton, and L. A. Zenteno, "Al/ge co-doped large mode area fiber with high sbs threshold," *Opt. Express*, vol. 15, pp. 8290–8299, Jun. 2007.

[67] A. Kobyakov, M. Sauer, and J. Hurley, "Sbs threshold of segmented fibers," in *Optical Fiber Communication Conference, 2005. Technical Digest. OFC/NFOEC*, vol. 1, p. 3 pp. Vol. 1, Mar. 2005.

[68] A. L. Campillo, F. Bucholtz, K. J. Williams, and P. F. Knapp, "Maximizing optical power throughput in long fiber optic links," tech. rep., Naval Research Laboratory, 2006.

[69] Z. Lali-Dastjerdi, M. Rahmani, and F. Kroushawi, "Modeling multi-pumped raman fiber amplifiers," in *PhotonicsGlobal@Singapore, 2008. IPGC 2008. IEEE*, pp. 1–3, Dec. 2008.

[70] T. Okuno, M. Hirano, T. Nakanishi, and M. Onishi, "Highly-nonlinear Optical Fibers and Their Applications," *Sei Technical Review*, vol. 62, pp. 34–40, 2006.

[71] K.-W. Chung and S. Yin, "A highly nonlinear dispersion-shifted fiber with 9.3 um2 effective area and low loss for all fiber wavelength converter," *Microwave and Optical Technology Letters*, vol. 40, no. 2, pp. 153–156, 2004.

[72] R. Boyd, *Nonlinear optics*. Academic Press, 2008.